universität wien

MASTERARBEIT / MASTER'S THESIS

Titel der Masterarbeit / Title of the Master's Thesis

„Computational Investigation of Förster Resonance Energy Transfer of a Chromophore/Photosensitizer Pair Embedded in a Lipid Bilayer“

verfasst von / submitted by

Richard Wilhelm Jacobi, B.Sc.

angestrebter akademischer Grad / in partial fulfilment of the requirements for the degree of

Master of Science (MSc)

Wien, 2021 / Vienna 2021

Studienkennzahl lt. Studienblatt / degree programme code as it appears on the student record sheet:	UA 066 862
Studienrichtung lt. Studienblatt / degree programme as it appears on the student record sheet:	Masterstudium Chemie
Betreut von / Supervisor:	Univ.-Prof. Dr. Dr. h.c. Leticia González Herrero

To my family,
for their endless support.

Abstract

In photosynthesis, highly optimized energy transfers are achieved by constraining the arrangement of chromophores in complex biological environments such as phospholipid membranes. Here, a bio-inspired light-harvesting system comprising a modified perylene diimide chromophore as energy donor and a derivative of the Ruthenium(II) tris-bipyridyl photosensitizer as energy acceptor embedded into opposite leaflets of a phospholipid bilayer is computationally investigated. Focus is the energy transfer rate within the realm of Förster Resonance Energy Transfer (FRET) theory, which is quantified based on a coherent theoretical approach. Photophysical properties such as absorption and emission spectra and transition electric dipole moments are computed for representative conformational ensembles by means of density functional theory. Distance and arrangement of the chromophores are monitored in time through classical molecular dynamics simulations. The FRET rate for the system, which is quantified based on these results, highlights advantages of the membrane confinement, such as the spatial proximity of the chromophores, as well as drawbacks, namely the unfavorable relative arrangements, and provides valuable insights into optimization strategies.

Zusammenfassung

In der Photosythese werden hochoptimierte Energietransfers ermöglicht, indem die Ausrichtung der Farbstoffe in komplexen biologischen Umgebungen, wie zum Beispiel Phospholipidmembranen, eingeschränkt wird. Hier wird ein die Natur nachahmendes System untersucht, das aus einem modifizieren Perylendiimid als Energiedonor und einem vom Ruthenium(II)tris-bipyridin Photosensibilisator abgeleitetem Akzeptor besteht, die beide in gegenüberliegenden Seiten einer Lipiddoppelschicht eingebettet sind. Schwerpunkt liegt dabei auf dem Bestimmen der Rate des Energietransfers im Rahmen der Methodik des Förster-Resonanzenergietransfers (FRET) mit computerbasierten Methoden. Die photophysikalischen Eigenschaften wie etwa Absorptions- und Emissionsspektren sowie Übergangsdipolmomente werden für charakteristische Konformationsensembles mit der Dichtefunktionaltheorie berechnet. Die zeitabhängigen Abstände und Ausrichtungen der Farbstoffe werden in klassischen Molekulardynamiksimulationen verfolgt. Die auf den Ergebnissen basierende FRET-Rate für das System zeigt Vorteile der Immobilisierung in der Membran, wie etwa die räumliche Nähe der Moleküle zueinander, sowie Nachteile wie ungünstige Ausrichtungen auf.

Acknowledgements

First of all, I would like to express my thanks to Prof. Leticia González for giving me the opportunity to work within her group, for her aid, guidance, advise, and indulgence.

I would like to thank Monika Schett and Sophie Gröber for handling administrative complexities, Dr. Markus Oppel and Denis Hoxha for providing technical support, Dr. Sebastian Mai for extensive scientific discussions, and Ass.-Prof. Pedro Sánchez Murcia and Dr. Davide Avagliano for helping me MD — some day I'll figure it out. I thank everybody in the group for making me feel welcome and creating an environment it is a pleasure to work in, but which also helps me forget work when need be. I am really grateful to each and everyone of you for both your scientific and non-scientific inputs.

My special thanks go to David Hernández-Castillo, for putting up with me during these months, for your patience and constant availability, for your foresight and care, and for all the hours you sacrificed to help me assemble this work.

I am grateful to my family, to my parents, to my grandparents, and to my siblings, for always being there for me, for constant support, and for enabling me to complete this degree with no worries.

List of acronyms

CREST	Conformer-rotamer ensemble sampling tool
DFT	Density functional theory
DOPG	dioleoylphosphatidylglycerol
DPPC	dipalmitoylphosphatidylcholin
FCHT	Franck-Condon and Herzberg Teller approach
FRET	Förster resonance energy transfer
FWHM	Full width at half maximum
GAFF	Generalized Amber force field
GGA	Generalized gradient approximation
HOMO	Highest occupied molecular orbital
LDA	Local density approximation
LUMO	Lowest unoccupied molecular orbital
LSDA	Local spin density approximation
MD	Molecular dynamics
MM	Molecular mechanics
MO	Molecular orbital
QM	Quantum mechanics
PCA	Principal component analysis
PDI	Perylene diimide
PSI	Photosystem I
RESP	Retrained electrostatic potential
$Ru(bpy)_3$	Ruthenium (II) tris-bipyridyl
TD-DFT	Time-dependent density functional theory
TDM	Transition electric dipole moment

List of symbols

0 (subscript)	Ground state
$\Delta A(\omega)$	Absorption spectrum
A (subscript)	FRET energy acceptor
a_i	Empirical angle parameter
b_i	Empirical bond parameter
c	Speed of light
$\vec{c}$	Linear combination of atomic coordinates
D (subscript)	FRET energy donor
E	energy
E_{elec}	Electronic energy
E_{XC}	Exchange-correlation energy
$\mathcal{F}$	Force
$F[\rho]$	Energy density functional
$F(\omega)$	Fluorescence emission spectrum
$f_{Hxc}(\omega)$	exchange-correlation kernel
$\hat{H}$	Hamiltonian operator
$\hat{H}_{elec}$	Electronic Hamiltonian
$h^{\hat{K}S}$	Kohn-Sham operator
$\hbar$	reduced Planck constant
i	Imaginary constant
J	Coloumb energy
k_{FRET}	FRET rate constant
l_i	bond length
M	Number of nuclei
m_i	Mass of particle i
N	Number of electrons
n	Multiplicity of torsional potentials
$P[\rho]$	Action principle
Q	Set of normal modes
q_i	Charge of particle i
r_{AD}	donor-acceptor distance
$\vec{r}_{AD}$	donor-acceptor distance vector
$\vec{r}_i$	set of spatial coordinates
$\vec{r}_{jk}$	distance between electron j and k
$\vec{r}_{jA}$	distance between electron j and nucleus A
S_0	Singlet ground state
S_I	Ith singlet excited state
S (subscript)	Non-interacting Kohn-Sham reference system
$\hat{T}$	Kinetic energy
t	time
t_i	Empirical torsion parameter
V	Potential
V_{Ne}	nuclei-electron attraction potential
V_{ee}	electron-electron repulsion potential
V_{ext}	external potential
V_{XC}	Exchange-correlation potential
v_S	effective one-electron potential

w_{Nn}	Weight of atom Nn to $\vec{c}$
$\vec{x}_i$	set of spatial and spin coordinates
x_i	x-coordinate of particle i
x, y, z	Cartesian coordinates
Z_A	nuclear charge of atom A

α, β, γ	Empirical parameters in hybrid functionals
ϵ_0	vacuum permittivity
ϵ_j	eigenvalue of Kohn-Sham orbital φ_j
ε_{ij}	Lennard-Jones potential well depth
η	refractive index
Θ	Slater determinant
θ_i	Bond angle
θ_A	Angle between $\vec{\mu}_A$ and $\vec{r}_{AD}$
θ_D	Angle between $\vec{\mu}_D$ and $\vec{r}_{AD}$
θ_{AD}	Angle between $\vec{\mu}_D$ and $\vec{\mu}_A$
κ^2	FRET orientation factor
λ	Normal mode
$\hat{\mu}$	Electric dipole moment operator
$\hat{\mu}_e$	Electronic dipole moment operator
$\vec{\mu}_{ij}$	TDM (general representation)
$\vec{\mu}_A$	FRET acceptor TDM vector
$\vec{\mu}_D$	FRET donor TDM vector
ρ	probability density (electron density)
σ_i	spin coordinate
ς_{ij}	Lennard-Jones potential collision diameter
Φ	Torsional angle
φ_j	Kohn-Sham one-electron spin orbital
$\chi[\rho_0]$	Point-wise susceptibility
Ψ_0	Ground-state wave function
Ψ_I	State I wave function
Ψ_{elec}	Electronic wave function
Ω_I	True excitation energy of state I
ω	frequency

Contents

1 Introduction

Oxygen-producing photosynthesis is a crucial process in converting solar radiation into chemical energy[1]. Among the key principles of this fundamental transformation are the absorption of photons as well as a spatial separation of charges[2]. These light harvesting processes are achieved by employing multi-subunit protein complexes, which are embedded into flexible, fluid two-dimensional lipid bilayers, the thylakoid membranes of chloroplasts[2, 3]. These membranes enable compartmentalization, creating the prerequisite for charge separation and the generation of independent reaction environments within the different compartments, such as distinct pH values[1]. Additionally, the membrane accounts for the arrangement of inserted complexes, facilitating light-collecting antenna complexes to transfer absorbed radiation onto photochemical reaction centers[2, 4]. These transfers are highly complex, with photosystem I (PSI) alone containing 127 co-factors[1], and can be manipulated by controlling the orientation of the embedded light-harvesting chromophores[5]. There is reason to believe that the arrangement of the chromophores within this excitation-transfer networks has been optimized with respect to the transfer efficiency, with PSI exhibiting a quantum yield close to unity[1, 4].

Mimicking this membrane compartmentalization has already been successfully implemented in artificial photosynthesis. The designs under investigation include water oxidation, hydrogen production and CO_2 reduction catalysts[6–9]. The use of these lipid bilayers ensures spatial proximity of the compounds as well as the possibility of generating different environments as a result of the separation through the membrane. Additionally, it was observed that the insertion into phospholipid membranes not only allowes the introduction of water-insoluble compounds and with this exposing them to an aqueous environment, but also enhanced the stability of the catalyst units and increased the efficiency at low concentrations without reducing the reaction rates at elevated concentrations. These findings make vesicles interesting for potential application, and research currently focuses on increasing efficiencies and tackling problems such as oxidative quenching caused by the environment[6, 9].

The energy transfers occuring between the chromophores in tylakoid membranes as well as between antenna molecules and photosensitizers in artificial systems can be qualitatively and quantitatively described by Förster Resonance Energy Transfer (FRET) theory[3]. Here, energy is transferred from an electronically excited-state donor to an acceptor chromophore in the electronic ground state, thus producing a ground-state donor and an excited-state acceptor (see figure 1). This transfer occurs as a result of radiationless resonance between the transition electric dipole moments of the respective states in donor and acceptor. As a consequence, FRET theory holds between donor and acceptor molecules sufficiently separated such that the electronic wave functions do not overlap, but at interchromophoric distances smaller than the excitation wavelength, such that emission and reabsorption do not occur[10].

Within the FRET formalism, the energy transfer rate depends on the chromophore-chromophore distance and their relative arrangement, as well as the spectral overlap of the emission and absorption spectra[10]. Especially the high sensitivity to distance renders FRET a powerful tool when used to assess the spatial separation of chromophores, *i.e.*, as a molecular ruler[11]. However, when the distance is calculated from the FRET efficiency, the orientation dependency is often neglected. This is a reasonable approximation in isotropic media, where the orientation factor κ^2 can be averaged over the ensemble[12]. However, this conjecture falls as soon as the arrangements are constraint, which is especially the case in biological samples, where chromophores are embedded into macro- and supramolecular structures such as protein complexes, thus

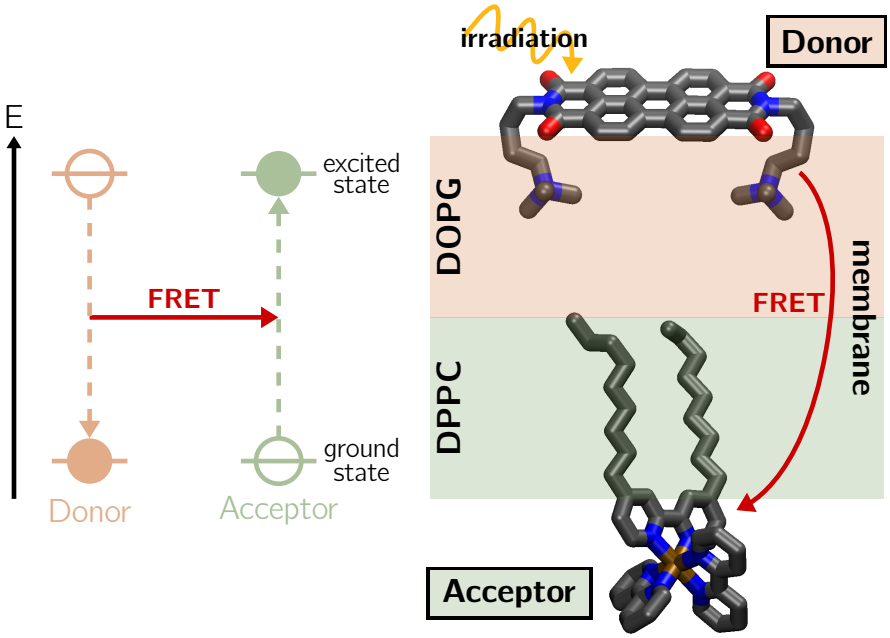

Figure 1: Left: Energetic diagram of the Förster Resonance Energy Transfer. Right: Scheme of the artificial light-harvesting system. The PDI derivative and modified $Ru(bpy)_3$ complex are embedded in the membrane leaflets comprising DOPG and DPPC lipids, respectively. After irradiation, the energy is transfered from the donor to the acceptor according to the Förster Resonance Energy Transfer (FRET) framework. Atoms and bonds are colored by element: grey for carbon, blue for nitrogen, red for oxygen, and ochre for ruthenium.

inhibiting the movement and rotation of the co-factors[11]. This can induce uncertainties to the calculated distances of well over 10 Å when arrangements are neglected[12, 13].

This view of κ^2 as a factor of uncertainty, however, does not account for the advantages and possibilities in investigating the orientation between the chromophores, as it opens a route for the optimization of the energy transfer by analyzing and subsequently adjusting the chomophore arrangements in possible applications. In general, the assessment of how the orientation affects the transfer efficiency can be made through experiments, but require significant alterations. For instance, DNA has been used to control the orientation of chromophores attached to opposite ends of a strand, as the double-helical structure of DNA enables to manipulate the angle between the chromophores as a function of strand length[11, 12].

Computational methods allow to investigate the orientation effects more closely in the respective environment without the need of such scaffold structures. Therefore, FRET efficiency evaluation in constrained media often require both experimental and computational approaches. The orientation factor has been computed employing molecular dynamics (MD) simulations, which include coarse-grained[14], all-atom force-field[10, 15, 16] and ab-initio approaches[17], while it is still common to average over ensembles, in turn introducing dubiety. Additionally, within the calculations, the spectral overlap is either neglected or included as a constant measured experimentally. This leaves much to be desired regarding a concise computational approach, in which all factors affecting the FRET rate and efficiency are directly accessible using theoretical methods, thus minimizing the need for external data.

In this work, the **object of investigation** is an artificial light-harvesting system

consisting of a perylene diimide (PDI) derivative as energy donor and a modified ruthenium(II) tris-bipyridyl ($Ru(bpy)_3$) complex as acceptor inserted into opposite leaflets of a phospholipid bilayer. This system is studied in collaboration with A. Pannwitz and coworkers[18] in the framework of the transregional research project TRR 234 "Catalight".

The donor-acceptor distance and the relative arrangements as well as the photophysical properties of the chromophores will be evaluated using computational tools based on the **hypothesis** that all properties affecting the FRET rate can be assessed employing distinct theoretical methods in a bottom-up approach. The **main objective** is to evaluate the FRET rate for the modified PDI / $Ru(bpy)_3$ chromophore pair within the lipid bilayer membrane. To this end, the following **individual goals** are targeted:

1. To compute the photophysical properties, which include emission and absorption spectra as well as the transition electric dipole moments (TDMs), using density functional theory (DFT). Here, the overlap is calculated and decomposed into contributions of all relevant electronic transitions. Additionally, the theoretical spectra will be compared to experimental spectra to ensure the applicability of the selected method.

2. To evaluate the influence of the aliphatic chains used to improve the interaction of the chromophore with the phospholipid membrane by performing the DFT calculations on the full molecules as well as model systems, where the aliphatic tails are substituted for methyl groups. Additionally, the computation of photophysical properties is performed on a conformational ensemble of the structures to account for various geometries, as single local minima are insufficient to correctly describe the molecule's properties in a thermodynamic ensemble[19].

3. To monitor the arrangement and orientation as well as the distance between the chromophores in time by means of classical force-field based MD simulations. Therefore, the directionality of the TDMs is referenced from the quantum mechanical (QM) calculations to the molecular geometry.

4. To propose rate optimization strategies based on the results of this multiscale approach, which are are combined to quantify the FRET rate.

The remainder of this thesis is organized as follows: The theoretical background concerning the methodologies employed is introduced in section 2, alongside the computational details in section 3. The results are analyzed in section 4, from the QM calculations in section 4.1 to the MD simulations in section 4.2. Finally, the FRET rate is evaluated in section 4.3. The most important results are again underlined in section 5, which concludes this work.

2 Theoretical background

The evaluation of the energy transfer efficiency in this work is based on FRET. The FRET formalism as well as the parameters influencing the FRET rate are presented in section 2.1. To compute these parameters, the photophysical properties of the chromophores will be computed using DFT and time-dependent DFT (TD-DFT), which is introduced in section 2.2. Since PDI exhibits a distinct vibrational fine structure in the optical spectra, vibrationally-resolved spectra are computed following a TD-DFT-based formalism presented in section 2.3. While the photophysical properties can be computed with DFT, this method is too computationally demanding to simulate the arrangements of the structures within the membrane. In this work, MD simulations for the monitoring of position and arrangement of the chromophores in the lipid bilayer are performed by force-field based methods as outlined in section 2.4.

2.1 Förster Resonance Energy Transfer

Theodor Förster investigated solutions which he irradiated with a polarized light source. He realized that highly viscous solutions subsequently emit radiation that is polarized in the same way as the incident rays[20]. Only molecules, whose transition moments coincide within the polarization plane, can absorb radiation, and hence only these will emit radiation. Molecules of other orientations will not be excited in the first place. In viscous media, the Brownian molecular motion is limited. As a result, there is little reorientation of the excited chromophores prior to fluorescence, and the emitted radiation is polarized, as well. However, the fluorescence signal is depolarized at elevated chromophore concentrations[20].

J. Perrin[21, 22] and his son F. Perrin[23] attributed this depolarization to a resonant transfer of excitation energy between neighboring molecules of different orientations, such that the emitter does not have to be aligned with the irradiating polarization plane. However, F. Perrin's quantum mechanical theory failed to predict key values such as the mean interchromophoric distance quantitatively. Förster expanded on their theory and included well-described effects such as Dirac's formula for the evaluation of transition probabilities and Einstein's theories on spontaneous emission to link his findings to the fluorescence and absorption spectra of the chromophores[24]. A key simplification was to approximate the influence of the fluctuating electronic charges of both chromophores as described by J. Perrin with the Coulomb interactions between two dipoles[24]. This approximation holds true for large molecular distances with respect to the size of the molecules. With this, Förster was able to define a quantitative description of the energy transfer rate. Within this FRET formalism, the rate constant k_{FRET} can be expressed as[11]

$$k_{FRET} = \frac{1}{\hbar^2 c \eta^4 (4\pi\epsilon_0)^2} * \frac{\kappa^2 \left|\vec{\mu}_D\right|^2 \left|\vec{\mu}_A\right|^2}{r_{AD}^6} \int_0^\infty F_D(\omega) A_A(\omega) d\omega, \tag{1}$$

where $\hbar$ is the Planck constant divided by 2π, c is the speed of light, η is the medium refractive index and ϵ_0 is the vacuum permittivity. The spectral overlap $\int_0^\infty F_D(\omega) A_A(\omega) d\omega$ is defined as the overlap of the fluorescence spectrum of the donor $F_D(\omega)$ and the absorption spectrum of the acceptor $A_A(\omega)$ integrated over the entire frequency definition range. The FRET rate diminishes with the chromophore distance r^6[10]. The squared moduli $|\vec{\mu}_D|^2$ and $|\vec{\mu}_A|^2$ represent the magnitude of the transition electric dipole moments (TDMs) of donor and acceptor, respectively, while their orientation effects are included in the factor κ^2, which is given as[11]

$$\kappa^2 = \frac{(\vec{\mu}_D \cdot \vec{\mu}_A) - \frac{3}{r_{AD}^2}(\vec{\mu}_D \cdot \vec{r}_{AD})(\vec{\mu}_A \cdot \vec{r}_{AD})}{|\vec{\mu}_D|^2 \, |\vec{\mu}_A|^2} \tag{2}$$

Solving the dot products between the TDMs and the distance vector allows to represent κ^2 in a simplified form as

$$\kappa^2 = [\cos(\theta_{AD}) - 3\cos(\theta_D)\cos(\theta_A)]^2 \tag{3}$$

where θ_{AD} represents the angle between the donor and acceptor TDMs, while θ_D and θ_A are the angles between the respective TDM and the distance vector $\vec{r}_{AD}$ (see figure 2)[11].

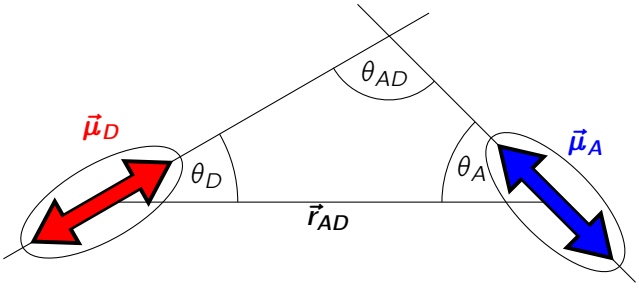

Figure 2: Scheme of the angles enclosed by the transition dipole moments of donor and acceptor, $\vec{\mu}_D$ and $\vec{\mu}_A$, respectively, and the distance vector $\vec{r}_{AD}$ as used in equation 3.

In this way, κ^2 varies between 0 for perpendicular TDMs (with one of the TDM perpendicular to the distance vector $\vec{r}_{AD}$), 1 for parallel TDMs (with again one of the TDM perpendicular to the distance vector $\vec{r}_{AD}$) and the maximum value of 4 for TDMs both aligned with the distance vector $\vec{r}_{AD}$ and, as a result, along each other (see figure 3). In isotropic media, where there is no preferred alignment, the orientation factor can be averaged over the ensemble. In these cases, κ^2 is generally simplified to $\kappa^2 = 2/3$[25].

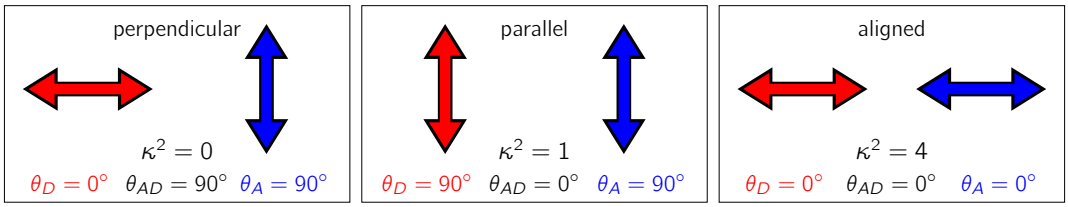

Figure 3: κ^2 values for distinct transition dipole moment alignments.

2.2 Density Functional Theory and its time-dependent version

All properties of a system in its electronic ground state can be determined through the wave function $\Psi_0 = \Psi_0(\vec{x}_1, \vec{x}_2, \ldots, \vec{x}_N)$, where $\vec{x}_i$ designates a set of spatial coordinates $\vec{r}_i$ and spin coordinates σ_i. Ψ_0 is subject to the non-relativistic, time-independent Schrödinger equation,

$$\hat{H}\Psi_0 = E_0\Psi_0 \tag{4}$$

where $\hat{H}$ is the Hamiltonian operator and E_0 is the ground-state energy[26]. Within the Born-Oppenheimer approximation[27], which neglects the kinetic energy of the

nuclei and allows to isolate the electronic ground-state wave function Ψ_{elec} from Ψ_0, equation 4 gets reduced to

$$\hat{H}_{\text{elec}}\Psi_{\text{elec}} = E_{\text{elec}}\Psi_{\text{elec}}. \tag{5}$$

The electronic energy E_{elec} now differs from the total energy only by the nuclear repulsion energy. The electronic Hamiltonian $\hat{H}_{\text{elec}}$ contains terms representing the kinetic energy ($\hat{T}$), nuclei-electron attraction ($\hat{V}_{Ne}$) and electron-electron repulsion ($\hat{V}_{ee}$):

$$\hat{H}_{\text{elec}} = \hat{T} + \hat{V}_{Ne} + \hat{V}_{ee} = -\frac{1}{2}\sum_{j=1}^{N}\nabla_j^2 - \sum_{j=1}^{N}\sum_{A=1}^{M}\frac{Z_A}{r_{jA}} + \sum_{j=1}^{N}\sum_{k>j}^{N}\frac{1}{r_{jk}}. \tag{6}$$

where N and M are the number of electrons and nuclei, respectively. Further, Z_A is the nuclear charge of atom A, while r_{jk} and r_{jA} denote electron-electron and electron-nuclei distances, respectively. All equations are given in atomic units. From here on, if nothing else is noted, Ψ indicates the electronic wave function.

The wave function is not an observable but is closely connected to the probability density $\rho(\vec{r})$, more commonly simply referred to as the electron density, which can be obtained by integrating the squared modulus over all electronic spins and all but one spartial coordinate:

$$\rho(\vec{r}_1) = N\int\cdots\int|\Psi(\vec{x}_1,\vec{x}_2,\ldots,\vec{x}_N)|^2\,\mathrm{d}\sigma_1\mathrm{d}\vec{x}_2\ldots\mathrm{d}\vec{x}_N. \tag{7}$$

Employing the electron density as the central quantity forms the basis of DFT. This approach is justified by two theorems published by Hohenberg and Kohn in 1964[28]. The first states that an external potential, such as the nuclear potential of a molecule, can be unambigously determined from the electron density. Since the electronic Hamiltonian directly depends on the external potential according to equation 6, and the ground-state wave function can be evaluated with the Hamiltonian, there is a functional dependency between the ground-state electron density, the ground-state wave function, and, in turn, the ground-state energy and all other properties of the system. Therefore, this is called DFT. Hohenberg and Kohn defined a functional $F[\rho]$, that formally represents the kinetic and electron-electron interaction energy terms for a given electron density. This energy differs from the system's total energy only by the potential energy of the electrons within the external potential and the nuclear repulsion energy term.

The second theorem is the formulation of the variational principle for DFT. It states that the true $F[\rho]$ will return the minimum energy if and only if the electron density is exactly that of the true ground-state density, *i.e.*, that of the true ground-state wave function. For any other density, the energy evaluated using $F[\rho]$ will be larger, or, in other words, less negative[28]. This means that there is not only a functional dependency between the ground-state density and the ground-state wave function, but the variational principle also allows a general assessment of the quality of any given electron density with respect to the true ground-state density.

The two Hohenberg-Kohn theorems represent the physical justification for any method that attempts to assess the properties of a system *via* its electron density, such as DFT. However, it lacks any practical description of how to compute the functional $F[\rho]$. This changed in 1965, when Kohn and Sham published an, in principle, exact approach to the computation of the energy as a functional of the electron density[29].

Analogously to the Roothaan equations[30], a molecular orbital representation of the Hartree-Fock approach[31, 32], within the realm of wave function-based methods,

Kohn and Sham proposed a non-interacting reference system comprising Kohn-Sham orbitals $\varphi_j(\vec{r},\sigma)$, which are one-electron spin orbitals. These spin orbitals combined have to equal the true ground-state density $\rho_0(\vec{r})$:

$$\rho_s(\vec{r}) = \sum_j^N \sum_\sigma \left|\varphi_j(\vec{x})\right|^2 = \rho_0(\vec{r}). \tag{8}$$

The Kohn-Sham orbitals are associated with eigenvalues ϵ_j, which are approximations to optical excitation energies of zeroth-order[33], *via* the Kohn-Sham operator $\hat{h}^{KS}$:

$$\hat{h}^{KS}\varphi_j = \epsilon_j\varphi_j \tag{9}$$

with

$$\hat{h}^{KS} = -\frac{1}{2}\nabla_j^2 + v_S(\vec{r}_j). \tag{10}$$

Here, $v_S(\vec{r}_j)$ is the effective potential acting on the individual electron within the non-interacting reference system. The anti-symmetric ground-state wave function is represented as a Slater determinant Θ of the spin orbitals:

$$\Theta = \frac{1}{\sqrt{N!}}\begin{vmatrix} \varphi_1(\vec{x}_1) & \varphi_2(\vec{x}_1) & \cdots & \varphi_N(\vec{x}_1) \\ \varphi_1(\vec{x}_2) & \varphi_2(\vec{x}_2) & \cdots & \varphi_N(\vec{x}_2) \\ \vdots & \vdots & \ddots & \vdots \\ \varphi_1(\vec{x}_N) & \varphi_2(\vec{x}_N) & \cdots & \varphi_N(\vec{x}_N) \end{vmatrix}. \tag{11}$$

The Hamiltonian of the non-interacting system can then be represented as

$$\hat{H}_S = -\frac{1}{2}\sum_j^N \nabla_j^2 + \sum_j^N v_S(\vec{r}_j). \tag{12}$$

The challenge tackled by Kohn and Sham at this point was to represent the energy functional $F[\rho]$ proposed by Hohenberg and Kohn as accurately as possible. This was achieved by splitting all terms that can be evaluated exactly, namely the kinetic energy of the non-interacting system $T_S[\rho]$ and the classical Coloumb terms $J[\rho]$, and collecting all other terms jointly in the newly-defined exchange-correlation energy functional $E_{XC}[\rho]$:

$$F[\rho(\vec{r})] = T_S[\rho(\vec{r})] + J[\rho(\vec{r})] + E_{XC}[\rho(\vec{r})]. \tag{13}$$

The exchange-correlation functional thus is defined as

$$E_{XC}[\rho(\vec{r})] = (T[\rho(\vec{r})] - T_S[\rho(\vec{r})]) + (E_{ee}[\rho(\vec{r})] - J[\rho(\vec{r})]) \tag{14}$$

i.e., by all kinetic energy contributions not covered by the kinetic energy of the non-interacting system, as well as all electrostatic electron-electron terms not covered by the Coloumb static interaction term. To this day, $E_{XC}[\rho]$ cannot be solved exactly. However, there are various approximations of this functional. The majority of these are based on the so-called local density approximation (LDA) and local spin density approximation (LSDA)[34]. This then got expanded using the generalized gradient approximation (GGA)[34], which was implemented for instance in the BP86 functional[35, 36]. Some of the most popular functionals nowadays, such as B3LYP[37, 38], which is also used in this work, are called hybrid functionals. In the hybrid functionals, exact exchange contributions are linearly combined with LDA- and GGA-based functionals

using semiempirical linear coefficients to obtain functionals that perform well when benchmarked against reference data bases containing experimentally well-determined energies[26]. For B3LYP, which is based on the B88 functional by Becke[35] and the LYP functional by Lee, Yang and Parr[37, 39], the formulation is as follows[34]:

$$E_{XC}^{\mathrm{B3LYP}} = (1-\alpha)E_x^{\mathrm{LSDA}} + \alpha E_x^{\mathrm{exact}} + \beta\Delta E_x^{\mathrm{B88}} + (1-\gamma)E_c^{\mathrm{LSDA}} + \gamma E_c^{\mathrm{LYP}} \tag{15}$$

The contribution of the individual exchange (x) and correlation (c) terms is goverened by the empirical parameters, which are usually set to $\alpha \sim 0.2$, $\beta \sim 0.7$, and $\gamma \sim 0.8$.[34]

To make the realm of excited states accessible to DFT, time-dependent density functional theory (TD-DFT) was introduced[33]. TD-DFT is based on ground-state DFT and applies its principles to time-dependent systems. As a result, even though both contain vastly different physics, huge parts of the formalism in TD-DFT are defined in the spirit of ground-state DFT and therefore follow similar statements[33]. Analogously to ground-state DFT, which is committed to solving the time-independent Schrödinger equation (equation 4), TD-DFT is based on the time-dependent Schrödinger equation:

$$i\frac{\partial}{\partial t}\Psi(t) = \hat{H}(t)\Psi(t). \tag{16}$$

where i is the imaginary constant. We define $\Psi(t)$ such that the wave function at time zero equals the true ground-state wave function of the unperturbed system:

$$\Psi(t_0) = \Psi_0. \tag{17}$$

The time-dependent Hamiltonian consists out of two parts, the system's Hamiltonian $\hat{H}_0(t)$, which contains the kinetic energy of the electrons and all particle-particle interactions within the realm of the Born-Oppenheimer approximation (see equation 6), and an external, time-dependent potential:

$$\hat{H}(t) = \hat{H}_0(t) + \hat{V}_{ext}(t). \tag{18}$$

Note that since $\hat{H}_0(t)$ is a functional of the ground state density, which will change according to the external, time dependent potential, $\hat{H}_0(t)$ is time-dependent, as well.

Similarly to how ground-state DFT is based on the Hohenberg-Kohn theorems, modern TD-DFT was conceived by Runge and Gross[33, 40] in their 1984 paper fittingly titled "Density Functional Theory for Time-Dependent Systems"[41]. As Runge and Gross proved, any time-dependent operator, and in turn the time-dependent wave function, is a unique functional of the time-dependent density as well as the true (initial) ground state density (up to a time-dependent phase factor).

Again, the wave function is constructed using a non-interacting system based on Kohn-Sham orbitals, which have to satisfy the time-dependent Kohn-Sham equation

$$i\frac{\partial}{\partial t}\varphi_j(\vec{r},t) = \hat{h}_{KS}[\rho(\vec{r},t)]\varphi_j(\vec{r},t). \tag{19}$$

The Hamiltonian for this non-interacting, time-dependent reference system is of the form

$$\hat{H}_S[\rho(\vec{r},t)] = \hat{T}_S[\rho(\vec{r},t)] + \hat{V}_{ext}[\rho(\vec{r},t)] + \hat{V}_S[\rho(\vec{r},t)] + \hat{V}_{xc}[\rho(\vec{r},t)]. \tag{20}$$

Here, $\hat{T}_S[\rho(\vec{r},t)]$ accounts for the kinetic energy of the non-interacting system, $\hat{V}_{ext}[\rho(\vec{r},t)]$ is the time-dependent, external potential, $\hat{V}_S[\rho(\vec{r},t)]$ includes the effective potential within the non-interacting system, with the exchange-correlation potential

$\hat{V}_{xc}[\rho(\vec{r},t)]$ covering all additional effects of the interacting system not accounted for by the non-interacting approximation.

The Runge and Gross formalism allows, in principle, to compute a wave function based on the time-dependent density. Nevertheless, the computation of the time-dependent density is less straight-forward and was under debate for quite some time[40]. It was aimed to manifest a time-dependent density functional, for which the potential was a functional derivative[33]. Already in their 1984 paper, Runge and Gross proposed such an action principle of the form

$$P[\rho] = \int_{t_0}^{t_1} \langle \Psi[\rho](t) | i\frac{\partial}{\partial t} - \hat{H} | \Psi[\rho](t) \rangle dt, \tag{21}$$

claiming that this functional exhibits a stationary point at the true density and can therefore be computed using the derivative of $P[\rho]$ with respect to the density. This action can be directly derived from the time-dependent Schrödinger equation (equation 16). However, this representation includes some formal issues such as the so-called causality paradox[42]. This paradox stems from the construction of the potential as a functional derivative of this action:

$$v[\rho(\vec{r},t)] \equiv \frac{\delta P[\rho]}{\delta \rho(\vec{r}',t')}. \tag{22}$$

If this equation, however, holds, then one can also write the derivative of the potential with respect to the density as a second derivative of the action:

$$\frac{\delta v[\rho(\vec{r},t)]}{\delta \rho(\vec{r}',t')} = \frac{\delta^2 P[\rho]}{\delta \rho(\vec{r},t)\delta \rho(\vec{r}',t')}. \tag{23}$$

As a second derivative, the right hand side of this equation has to be symmetric under interchange of t and t'. Contrary, the left side can only be non-zero at times $t > t'$. This can be explained quite easily: While, naturally, changes in the density at times t' can and will affect the potential only at times t, which occur after the changes in density, *i.e.*, $t' < t$, any changes in density happening at a later point can not influence the potential at earlier times, signifying that $\frac{\delta v[\rho(\vec{r},t)]}{\delta \rho(\vec{r}',t')} = 0$ for $t' > t$. As a result, equation 23 can not hold for the formulation of the action principle given by Runge and Gross (equation 21).

It was only in 2008 that Vignale presented a solution to this causality paradox in real time[43]. Based on his work, the action principle through which the true electron density (in the limit of the exact exchange-correlation functional) can be obtained, can be written as[40]

$$P[\rho] = \int_{t_0}^{t_1} \langle \Psi[\rho](t) | i\frac{\partial}{\partial t} - \hat{H} | \Psi[\rho](t) \rangle dt - i\langle \Psi[\rho](t_1) | \delta\Psi[\rho](t_1) \rangle, \tag{24}$$

where the action proposed by Runge and Gross is expanded by an additional "boundary term"[43]. This can be regarded as the TD-DFT analogue to the variational principle of ground-state DFT.

With this rigorous formal description of the time-dependent density, the next step is to propagate the density and with this extract information such as photophysical properties of a system. Aside from real-time TD-DFT[44, 45], this is most commonly done using first-order response theory. This approach is especially useful in situations where the perturbation, *i.e.*, the external field, is weak[40]. The first-order response of the density can be given in terms of the point-wise susceptibility $\chi[\rho_0]$:

$$\delta\rho(\vec{r},t) = \int_{-\infty}^{t} \int \chi[\rho_0](\vec{r},\vec{r}',t,t')\delta v(\vec{r}',t')d\vec{r}dt'. \tag{25}$$

For the non-interacting Kohn-Sham system, this representation takes the form

$$\delta\rho(\vec{r},t) = \int_{-\infty}^{t} \int \chi_S[\rho_0](\vec{r},\vec{r}',t,t')\Big[\delta v_{ext}(\vec{r}',t')+\delta v_H(\vec{r}',t')+\delta v_{xc}(\vec{r}',t')\Big]d\vec{r}dt'. \tag{26}$$

Fourier-transforming these two equation yields the susceptibility response function in frequency-space:

$$\hat{\chi}(\omega) = \lim_{\eta\to 0^+}\sum_I \frac{\langle\Psi_0|\hat{\rho}|\Psi_I\rangle\langle\Psi_I|\hat{\rho}|\Psi_0\rangle}{\omega-\Omega_I+i\eta} - \frac{\langle\Psi_0|\hat{\rho}|\Psi_I\rangle\langle\Psi_I|\hat{\rho}|\Psi_0\rangle}{\omega+\Omega_I-i\eta}. \tag{27}$$

This equation contains the density expectation values for the ground-state and excited-state wave functions, Ψ_0 and Ψ_I, respectively. This function has poles, *i.e.* the it blows up, at $\omega = \Omega_I$, which is the true excitation energy. The response function for the non-interacting Kohn-Sham system takes up a similar form:

$$\hat{\chi}_S(\omega) = \lim_{\eta\to 0^+}\sum_{ja}(f_a - f_j)\frac{\hat{\varphi}_j\hat{\varphi}_j^*\hat{\varphi}_a\hat{\varphi}_a^*}{\omega-(\epsilon_a-\epsilon_j)+i\eta}, \tag{28}$$

with now the excitation energy being represented by the difference in Kohn-Sham eigenvalues $\epsilon_a - \epsilon_j$, corresponding to exciting one electron from the occupied orbital j to the previously unoccupied orbital a. Furthermore, the occupation numbers f_a and f_j are introduced. To use these Kohn-Sham excitations to compute the true excitation energies, one has to introduce the exchange-correlation kernel $f_{Hxc}(\omega) = \frac{\delta v_H(\omega)}{\delta\rho(\omega)} + \frac{\delta v_{xc}(\omega)}{\delta\rho(\omega)}$. With it, equations 27 and 28 can be combined to yield:

$$(\hat{1} - \hat{\chi}_S(\omega)f_{Hxc}(\omega))\hat{\chi}(\omega) = \hat{\chi}_S(\omega). \tag{29}$$

As long as $\epsilon_q - \epsilon_p$ is different from Ω_I, as it generally is, the left hand side tends to infinity at $\omega = \Omega_I$, while the right hand side adopts a finite value, breaking the equality. This issue can be resolved by identifying the eigenvalues of the equation

$$(\hat{1} - \hat{\chi}_S(\omega)f_{Hxc}(\omega))X(\omega) = \omega X(\omega). \tag{30}$$

Expanding this eigenfunciton in the Kohn-Sham spin orbital basis yields

$$\begin{bmatrix} \mathbf{\Lambda}(\omega) & \mathbf{\Pi}(\omega) \\ -\mathbf{\Pi}^*(\omega) & -\mathbf{\Lambda}^*(\omega) \end{bmatrix}\begin{bmatrix}\mathbf{X}(\omega)\\ \mathbf{Y}(\omega)\end{bmatrix} = \omega\begin{bmatrix}\mathbf{X}(\omega)\\ \mathbf{Y}(\omega)\end{bmatrix} \tag{31}$$

with

$$\Lambda_{ja,kb}(\omega) = \delta_{jk}\delta_{ab}(\epsilon_a-\epsilon_j) + \int\int \varphi_j^*(\vec{r})\varphi_a(\vec{r})\left[f_{Hxc}(\omega)\right]\varphi_b^*(\vec{r})\varphi_k(\vec{r})d\vec{r}d\vec{r}' \tag{32}$$

and

$$\Pi_{ja,kb}(\omega) = \int\int \varphi_j^*(\vec{r})\varphi_a(\vec{r})\left[f_{Hxc}(\omega)\right]\varphi_k^*(\vec{r})\varphi_b(\vec{r})d\vec{r}d\vec{r}'. \tag{33}$$

As a result, the change in time-dependent density can be represented as

$$\delta\rho(\vec{r},t) = \sum_{ja} \left(X_{ja}(\Omega_I)\varphi_a^*(\vec{r})\varphi_j(\vec{r}) + Y_{ja}(\Omega_I)\varphi_a(\vec{r})\varphi_j^*(\vec{r}) \right), \tag{34}$$

such that X_{ja} and Y_{ja} describe the weighting of the transition between orbitals $\varphi_a(\vec{r})$ and $\varphi_j(\vec{r})$ at an specific excitation frequency Ω_I. The latter can be extracted by analyzing the poles in equation 27. Similarly to the concepts of ground-state DFT, this representation is formally exact (within the realm of linear response), while the implementation in reality needs to approximate the exchange-correlation potential $v_{xc}(\vec{r},t)$.

2.3 Computation of vibrationally-resolved spectra

The absorption spectrum of a system is given by

$$\Delta A(\omega) = \frac{4\pi^2\omega}{3} \sum_f |\langle\Psi_i|\hat{\mu}|\Psi_f\rangle|^2 \delta(E_f - E_i - \hbar\omega), \tag{35}$$

where ω is the frequency, Ψ_i and Ψ_f denote the initial and final states corresponding to the energies E_i and E_f, respectively, and $\hat{\mu}$ is the electric dipole moment operator[46]. A key quantity in this formulation is the TDM integral $\langle\Psi_i|\hat{\mu}|\Psi_f\rangle$.

One of the most straight-forward ways for the computation of electronic spectra is to employ the vertical excitation approximation, *i.e.*, to compute the excitation energies and intensities at a given geometry and convolute these transitions using Lorentzian or Gaussian functions for homogeneous or inhomogeneous broadening, respectively[46, 47]. This approach performs quite reasonably in some cases, however, it neglects the complexity of the transition dipole moment integral, which, again within the Born-Oppenheimer approximation, can be represented as

$$\langle\Psi_i|\hat{\mu}|\Psi_f\rangle = \langle\nu_i|\vec{\mu}_{if}|\nu_f\rangle, \tag{36}$$

with ν_i and ν_f denoting the corresponding nuclear (vibronic) wave functions, and $\vec{\mu}_{if}$ being the transition electric dipole moment between the electronic wave functions ψ_i and ψ_f:

$$\mu_{if} = \langle\psi_i|\hat{\mu}_e|\psi_f\rangle. \tag{37}$$

$\hat{\mu}_e$ is the electronic dipole moment operator. $\vec{\mu}_{if}$ and its dependency on changes in molecular geometry are not known exactly, but have to be approximated. Therefore, it can be represented as a Taylor expansion of the form:

$$\vec{\mu}_{if}(Q) = \vec{\mu}_{if}(Q_0) + \sum_{k=1}^{\lambda} \frac{\partial\vec{\mu}_{if}}{\partial Q_k} Q_k + \frac{1}{2}\sum_{k=1}^{\lambda}\sum_{l=1}^{\lambda} \left(\frac{\partial^2\vec{\mu}_{if}}{\partial Q_k \partial Q_l} \right)_0 Q_k Q_l + \ldots \tag{38}$$

Q denotes a set of λ normal modes, which can be either the initial or the final state, though routinely the final state is chosen for computational reasons. The normal modes at equilibrium geometry are denoted as Q_0. These sets of normal modes have to be common between the final and initial state. The projection of the basis vectors of the normal modes can be done by means of a Duschinsky transformation.

The simplest approximation in this Taylor series is of zeroth order. Here, all changes in the transition dipole moment with respect to the molecular geometry are neglected. It is assumed that the geometry does not change during excitation whatsoever. This corresponds to the Franck-Condon principle. Considering the first-order term of equation 38 is the so-called Herzberg-Teller approximation, which particularly accounts for

dipole-forbidden or weakly allowed transitions. The combination of both is thus known as the Frack-Condon and Herzberg-Teller (FCHT) approach[46].

The implementation of the FCHT approach in the program Gaussian 16[48] requires three steps. First, the electronic ground and excited states are computed, for instance using TD-DFT. Subsequently, the normal modes are computed for each of the states of interest to construct each of the potential energy surfaces. Finally, both steps are combined and the wave-function overlap of all relevant nuclear wave functions are computed for two selected electronic states to obtain vibrationally resolved spectra fit to be convoluted to obtain the final vibrationally-resolved spectrum.

2.4 Molecular Dynamics simulations

The description of large systems using quantum mechanical methods such as DFT is not feasible due to the computational cost of electron-based methods. Molecular mechanics (MM) therefore approximates the system's total energy as a function of only the nuclear coordinates by using empirically potentials functions to describe the interaction between the atoms[49]. This comes at the cost of diminished accuracy as well as the incapability of describing electronic effects, such as bond cleavage and formation or photophysical properties, but allows the description of huge systems at a fraction of the cost of quantum chemical methods. A powerful tool within the realm of MM are empirical force field models. Here, the interaction potential between two nuclei is estimated using simple functions.

These functions can usually be divided into terms accounting for bonded, and others for non-bonded interactions. Bonds are most simply described by three energy terms, representing bond length and bond angle, while the third, torsional term accounts for bond rotations:

$$V_{bonded}(\vec{r}^M) = \sum_{bonds} \frac{b_i}{2}(l_i - l_{i,0})^2 + \sum_{angles} \frac{a_i}{2}(\theta_i - \theta_{i,0})^2 + \sum_{torsions} \frac{t_i}{2}(1 - cos(n\Phi - \xi)). \tag{39}$$

Here, bond lengths l_i and angles θ_i are represented as quadratic energy terms around the equilibrium value $l_{i,0}$ and $\theta_{i,0}$, respectively. To account for the periodical nature of bond rotations, the torsion term is included as a cosine function around the angle Φ. Furthermore, n is the multiplicity, which defines the number of minima along one bond rotation, and ξ is a phase factor, which determines the position of the minima. The steepness of each of the three terms is defined by the constants b_i, a_i and t_i, respectively. More sophisticated force fields expand the representation in equation 39 by additional terms, such as improper torsions, which help to describe geometric alterations that for instance effects like aromaticity cause.

The energetic effect of non-bonded interactions is composed of van der Waals terms and electrostatic contributions according to Coulomb's law with respect to the distance of the two particles r_{ij}:

$$V_{non-bonded}(\vec{r}^M) = \sum_{i=1}^{M}\sum_{j>i}^{M}\left(4\varepsilon_{ij}\left[\left(\frac{\varsigma_{ij}}{r_{ij}}\right)^{12} - \left(\frac{\varsigma_{ij}}{r_{ij}}\right)^{6}\right]\right) + \sum_{i=1}^{M}\sum_{j>i}^{M}\frac{q_i q_j}{4\pi\epsilon_0 r_{ij}}, \tag{40}$$

where the double sums are constructed such that double counting of one interaction is prohibited. The first term is the so-called Lennard-Jones 12-6 function, which can be tuned *via* the collision diameter ς_{ij}, which corresponds to the distance at which the energy is zero, and the well depth ε_{ij}, *i.e.*, the most negative value the function can

adopt. The second term is a standard Coulomb potential between two charges q_i and q_j, such that the potential becomes repulsive for equal-signed charges and attractive for opposite charges.

The terms presented here used to model both bonded as well as non-bonded interactions include various parameters, which have to be determined empirically. This parametrization can be a lenghtly and tedious task, as in principle every atom of every molecule has to be evaluated individually. In practice, however, it is common to group atoms of the same element into several categories based on for instance hybridization or special chemical nature such as radicals or charged species. Subsequently, parameters are fitted to match either experimental data or quantum chemical calculations performed on small model systems.

Once a potential energy hypersurface is constructed from equations 39 and 40, the system can be propagated in time. This is accomplished by solving Newton's law of motion

$$\frac{d^2x_i}{dt^2} = \frac{\mathcal{F}_{x_i}}{m_i}, \tag{41}$$

where the acceleration of a particle is computed from the force $\mathcal{F}_{x_i}$, which can be derived from the potential, and the mass of the particle m_i[49].

3 Computational details

Employing the methodologies presented in the previous section, the FRET rate and the properties influencing it are assessed. Here, the computational details of these calculations are presented. In section 3.1, the QM setup used to compute the photophysical properties of the chromophores is outlined. Special attention is given to the generation of conformers representative of thermally accessible ensembles. The computation of the position and arrangements of the chromophores within the lipid bilayer using MD simulations is detailed in section 3.2.

3.1 Quantum mechanical calculations

3.1.1 Computation of photophysical properties

All excited state calculations were computed on the restricted (closed shell) B3LYP[37, 38]/def2-SVP[50, 51] level of theory using the quantum chemistry program Gaussian 16, revision C.01[48]. Solvent effects for acetonitrile were included implicitly were noted using the polarizable conductor-like calculation model[52, 53] by placing the solute in a cavity within the solvent reaction field. Within the framework of the vertical approximation, properties related to absorption of radiation, such as absorption spectra and the corresponding TDMs, were computed on the optimized electronic ground state structure, while emissive properties were computed on the optimized first excited state geometry, assuming that each higher excited state relaxed into the S_1 state prior emission. These geometry optimizations were performed using B3LYP/def2-SVP, as well. Dispersive effects were corrected empirically using Grimme's D3 model with Becke-Johnson damping[54, 55]. All geometry optimizations were performed with tighter cutoffs on forces and step size (`tight` keyword in Gaussian 16). The convergence of the geometry optimizations was confirmed by the absence of imaginary frequencies. Electronic excited states were computed using TD-DFT. For each structure, 30 singlet excited states were calculated.

Wave function analysis was performed with Multiwfn[56] using the results of the Gaussian 16 calculations to compute the TDMs and to convolute the electronic transitions into absorption and emission spectra. Here, the convolution was achieved using Gaussian functions with a full width at half maximum (FWHM) of the default value in Multiwfn of precisely 0.66667 eV.

Vibrationally-resolved spectra were computed where noted using the FCHT method developed by Barone and coworkers as implemented in Gaussian 16[46, 57]. Therefore, normal modes were computed both on the ground state and the first excited state structures. The resulting spectra were convoluted with Gaussian functions at a FWHM of 0.08 eV.

3.1.2 Generation of representative conformers

Long aliphatic chains can adopt numerous different conformations, rendering it insufficient to merely compute the properties of one conformer[49, 58, 59]. Therefore, structures representative of the thermally-accessible conformational ensemble were generated for C4-PDI-C4 and Ru(bpy)$_2$bpyC9 using the conformer-rotamer ensemble sampling tool (CREST)[19, 60]. In CREST, the generated structures are optimized using the geometry, frequency, non-covalent extended tight binding model of version 2 (GFN2-xTB)[61]. To reasonably utilize computational resources, the structure crossing step within the standard CREST workflow, which generates new conformers as difference structures between two already existing conformers[62], was omitted for the

$Ru(bpy)_2bpyC9$ calculation. Solvent effects were included implicitly using the analytical linearized Poisson-Boltzmann model[19, 60] where noted.

Usually, it would be sufficient to consider all conformers within an energy range of 3 kcal/mol with respect to the global minimum, as, according to the Boltzmann distribution for an idealized, non-degenerate two level system, the population of a conformer that is 3 kcal/mol less stable compared to the lowest energy conformer, would be well below 1%. However, to compensate for inaccuracies in the semiempirical tight-binding GFN2-xTB method on which the conformers are optimized and energies are computed within the CREST workflow, all conformers within an energy window of 7 kcal/mol were included in the initial steps of the ensemble generation.

To reduce the vast ensembles generated with CREST (>38,000 conformers for $Ru(bpy)_2bpyC9$, >2,000 structures for C4-PDI-C4) without losing significant structures, the principal component analysis (PCA) and k-means clustering algorithm[63] included in the CREST program package was employed, where the ensemble is grouped based on the geometry of the molecules. By then only preserving one representative structure per cluster, the conformer number within the ensemble was decreased to 1000. Single point energies on these 1000 structures were computed on the BP86[35, 36]/def2-SVP level of theory using the quantum chemistry program ORCA (version 4.2.1)[64]. Solvent effects were included implicitly using the polarizable conductor-like calculation model. The resolution of identity approximation was utilized, employing the auxiliary basis set def2/J. Based on the BP86/def2-SVP energies, the number of representative structures was reduced to a final 100 and 92 for C4-PDI-C4 and $Ru(bpy)_2bpyC9$, respectively. To assess the performance of the BP86 functional, single point calculations on the B3LYP/def2-SVP level of theory were performed for these final structures in ORCA. Here, the RIJCOSX approximation for B3LYP was employed. Prior to computing the excited states for these representative structures, the geometries were optimized utilizing Gaussian 16 as described in section 3.1.1.

Optical spectra representative of the conformational ensemble were computed by linear combination of each individual spectrum weighted according to the Boltzmann distribution calculated with CREST based on the B3LYP/def2-SVP geometry optimized ground state energies.

3.2 Molecular dynamics simulations

MD simulations were performed using the program packages Amber20 and AmberTools21[65].

Starting structures were selected for the chromophores (C4-PDI-C4 and $Ru(bpy)_2bpyC9$) from the ensemble optimized on the B3LYP/def2-SVP level of theory. Point charges were computed using the restrained electrostatic potential atomic partial charges (RESP) scheme in Gaussian 16[48]. All point charges where computed on the optimized ground state geometries, such that, especially for the energy donor, any structural relaxations are neglected. The chromophores were described using the Generalized Amber Force Field (GAFF) included in AmberTools21, with additional parameters for the ruthenium complex taken from Brandt and coworkers[66]. During this parametrization of the ruthenium complex, all nitrogen-ruthenium-nitrogen angles were erroneous parametrized as cis angles (91.1°) in this work, instead of correctly labelling opposing nitrogen atoms as trans (180.0°) as described in the original publication[66]. However, since this affects three out of 15 angles, it is assumed that this only marginally distorts the complex scaffold, while not affecting the insertion mode into the membrane, both with respect to the distance to the center of the membrane as well as the orientation arrangement. This hypothesis is supported by one reference trajectory

with the correctly parametrized force field is presented in appendix A. There are no significant changes in chromophore insertion into the membrane and orientation with respect to the surface of the membrane between the correctly and falsely parametrized force fields. Therefore, it was decided not to redo all the simulations except for the presented reference trajectory, as the repeating would have required significant additional computational resources.

The lipid bilayer was assembled using the membrane builder of the web-based input generator CHARMM-GUI[67]. Therefore, chromophores were placed individually into a rectangular box each with an initial guess for the dimensions in x- and y-directions of 80 Å. The membrane comprised dipalmitoylphosphatidylcholine (DPPC) lipids in the upper, dioleoylphosphatidylglycerol (DOPG) lipids in the lower leaflet and was assembled in the xy-plane. The number of lipids was chosen automatically according to the box dimensions. The resulting numbers vary depending on the chromophore and the insertion mode from 99 to 102 for DPPC and from 93 to 95 for DOPG.

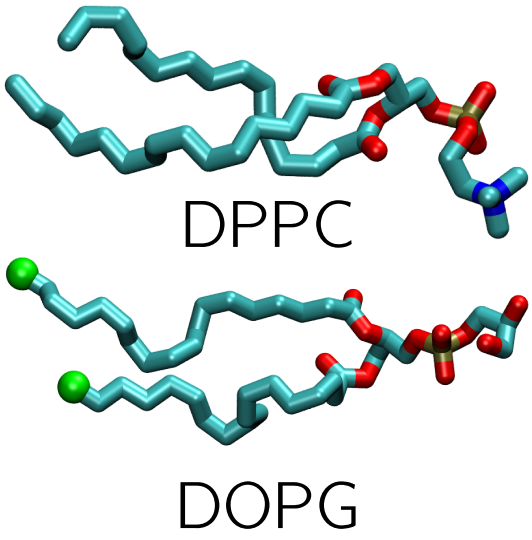

Figure 4: Molecular structures of DPPC (top) and DOPG (bottom). Atoms and bonds are colored by element: cyan for carbon, blue for nitrogen, red for oxygen and tan for phosphorus. The C_{18} atoms, which are used to define the center of the membrane, are highlighted in green.

To define the box dimension in z-direction, the hydration number of each lipid was set to 50, which is well in excess of experimental hydration numbers for similar lipids of 32.8[68]. The negative charge of the lipid head groups was neutralized by placing potassium ions into the solvated area of the box using the Monte-Carlo placing method, and subsequently the number of potassium and chlorine ions was increased to yield a salt concentration of 0.15 mol/L. The lipids were described using the Lipid17 force field, while water and the atomic ions were described using the "optimal" point charge model[69] implemented in AmberTools21.

Each system obtained from CHARMM-GUI was minimized using the Amber module pmemd in 5,000 minimization cycles employing a steepest descent algorithm, and another 5,000 additional steps using a conjugate gradient algorithm. The minimization was performed at constant pressure using anisotropic pressure scaling.

For all the MD simulations, a time step of 2 fs was used. To achieve this large time step, the SHAKE algorithm was turned on to freeze hydrogen bond lengths at a relative geometrical tolerance of 1e-7. Constant pressure periodic boundary conditions were superimposed with anisotropic pressure scaling. The cutoff for non-bonded interaction

terms was set to 10 Å. The simulation was performed using the GPU (CUDA) version of pmemd[70–72].

The minimized system was subsequently heated using the Langevin thermostat at a collision frequency of 1.0 ps^{-1} to 100 K in 2,500 time steps (5 ps), followed by a heating to 300 K in 50,000 steps (100 ps). The first heating was performed at a pressure relaxation time of 1 ps, which was increased to 2 ps for the second heating phase only.

Prior to production, the system was equilibrated by running 10 ps of simulation time (5,000,000 time steps).

The analysis of the simulation trajectories was performed using the program CPPTRAJ[73]. Visualization was done using the molecular viewer VMD[74]. The distance to the center of the membrane was computed as the center-of-mass distance between the core atoms of the chromophores, *i.e.*, all non-hydrogen atoms excluding the aliphatic tails, and the C_{18} atoms of the DOPG lipids. To ensure that this corresponds to the minimum distance between the chromophore and the membrane center and not some artificially elongated distance misrepresented by lateral movement of the ligand within the membrane, the chromophore was imaged into the center of the periodic box for each frame during the analysis. To monitor the orientations of the TDMs during the MD simulations, the TDM vectors are referenced onto linear combinations of nuclear coordinates based on the QM calculations. Assuming the membrane as fully aligned with the xy-plane, the angle of the transition dipole moment vectors to the membrane surface can be approximated using the positions of these reference atoms in each individual chromophore using simple trigonometry (see figure 5). This scheme also holds for more complex linear combinations of atomic positions.

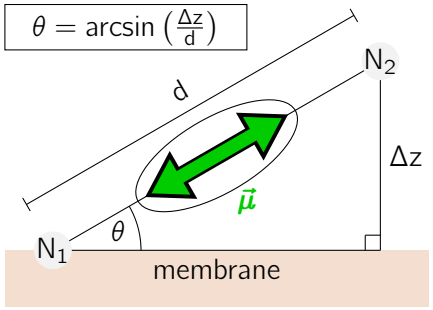

Figure 5: Scheme for the computation of the angle of the TDM with respect to the membrane surface in the xy-plane. The TDM is referenced onto a linear combination of nuclear coordinates, in this example $\vec{\mu} = r(N_1) - r(N_2)$.

3.3 Reference data

In this work, computed one-photon spectra are being compared to experimentally measured UV-vis absorption and fluorescence spectra recorded by A. Pannwitz and coworkers[18], collaborators within the transregional research project TRR 234 "Catalight".

In their experiments, the absorption and emission spectra of [C4-PDI-C4$(PF_6)_2$] were recorded in acetonitrile. For the latter, an excitation wavelength of 520 nm was used. The absorption spectra of [Ru$(bpy)_2$bpyC9$(PF_6)_2$] was recorded in water and in presence of DPPC at a 10:1 (lipid:chromophore) ratio, such that the lipid concentration was below 5 mM.

4 Results and discussion

To evaluate the rate constant, and thus the efficiency of the FRET, three key parameters have to be taken into consideration: the distance between the chromophores, the magnitude and the relative orientation of the TDMs, and the spectral overlap between the fluorescence spectrum of the donor and the absorption spectrum of the acceptor molecule (see equation 1).

In section 4.1, QM calculations on the excited state chromophores are performed using TD-DFT to compute the TDMs as well as one-photon spectra. The latter will be compared to experimental measurements to validate the theoretical setup. The TDMs will be quantified with respect to the nuclear coordinates.

In section 4.2, classical MD simulations are run for the chromophores embedded into the membrane. Different starting positions and orientations of the chromophores within the membrane will provide insights into the insertion modes into the membrane, as well as their evolution in time. Combined with the information on the TDM orientation within the molecule as established in section 4.1, this enables to evaluate the rate constant of the FRET.

4.1 Quantum mechanical calculations

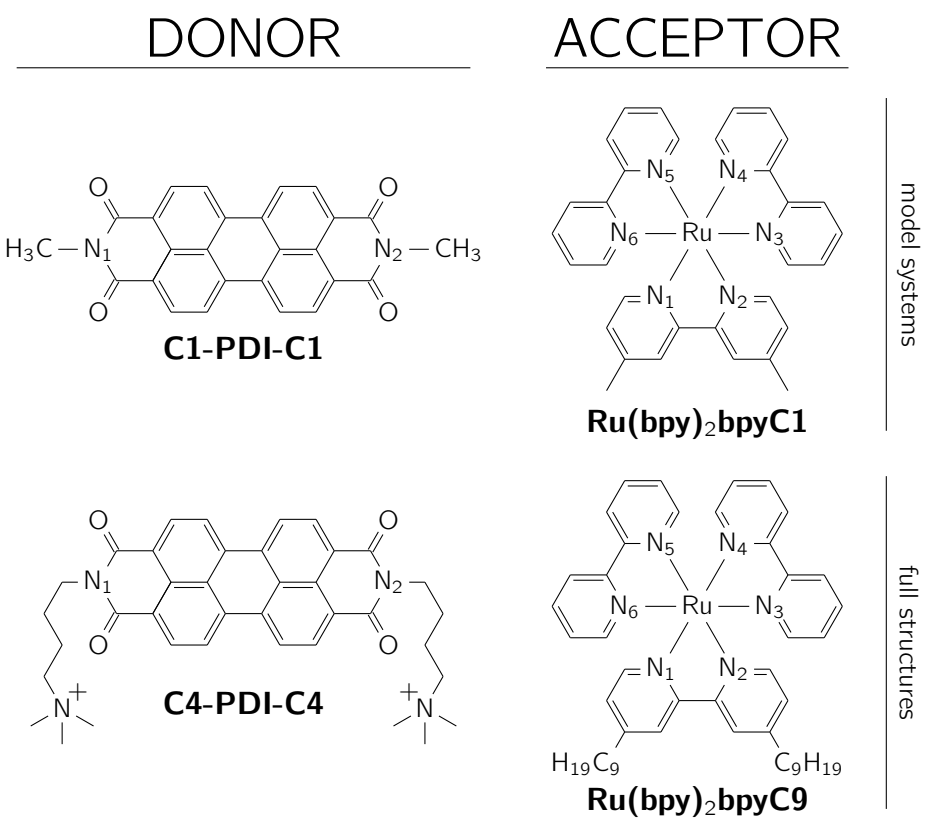

Figure 6: Different structures under investigation for the perylene diimide (left) and ruthenium(II) tris-bipyridyl derivatives (right). The nomenclature used in this work is given for the respective molecules, as well as the numbering for the nitrogen atoms.

In this section, the optical spectra as well as the TDMs will be computed using TD-DFT for the N-substituted PDI energy donor (section 4.1.1) and the modified $Ru(bpy)_3$ acceptor (section 4.1.2). To evaluate the influence of the aliphatic substituents present in both molecules, the calculation of the photophysical properties will

first be performed on model systems, which are in the following referred to as C1-PDI-C1 and Ru(bpy)$_2$bpyC1 (see figure 6). These are obtained from the full molecules by truncating the substituents to methyl groups. After that, the spectra and TDMs are calculated for the full molecules, namely C4-PDI-C4 and Ru(bpy)$_2$bpyC9. Here, special attention is given to the generation of a representative ensemble of conformers, and how distinct conformations affect the properties.

A third PDI derivative was initially considered, where the methyl groups in C4-PDI-C4 were substituted for hydrogen atoms. However, this molecule was disregarded due to a high similarity to C4-PDI-C4. The calculations that had already been performed are presented in appendix C.

4.1.1 PDI

The perylene diimide derivative is the energy donor. Therefore, emission spectra and the corresponding TDMs are computed and will be presented in the following section. Since the underlying photophysical process leading to emission here is the fluorescence, all transitions occur between the S_1 and the S_0. Within the vertical approximation, both these electronic states have to be investigated on the first excited state optimized structure. As a reference, the absorption spectra will be shown as well. For this, all properties are computed on the optimized ground state structure. In the following, these results will be shown for the truncated C1-PDI-C1 in gas phase and in acetonitrile, as well as for a conformational ensemble of the full C4-PDI-C4 in acetonitrile only.

C1-PDI-C1 For C1-PDI-C1, the geometries corresponding to the S_0 and S_1 electronic configurations were optimized in DFT / TD-DFT calculations in gas phase and acetonitrile to compute absorption and emission spectra. The result of these calculations are presented in figure 7.

Especially in the case of the absorption spectrum, there is a good agreement between theory and experiment. The low-enery range is dominated by absorptive bands in the region around 2.5 eV, while the region between 3 and 4.5 eV is optically mostly transparent in all cases. Even though the high-energy range is badly represented in the computations due to a limitation to 30 excited states, the experimental rise in intensity at energies larger than 4.5 eV is well visible in the computed spectrum for C1-PDI-C1 in acetonitrile, with a lower intensity signal for the calculations in gas phase. However, the experimental spectrum is clearly more detailed in the lower energy region compared to the TD-DFT spectra. This gets especially obvious in the emission spectra, as the $S_0 \rightarrow S_1$ transition is the only one that contributed towards fluorescence. Therefore, only one transition each is reported for the computed spectra, while in the experiment at least three distinct maxima can be observed, indicating the influence of vibrational effects.

In order to get a more realistic picture of the optical spectra, vibrationally-resolved spectra were computed by approximating the change in TDMs with respect to the nuclear coordinates by employing the FCHT approach (see section 2.3). The way that vibrationally-resolved spectra are computed within the FCHT approximation is to compute the nuclear vibrations of two distinct electronic configurations, in this case S_0 and S_1, and evaluate the wave function overlap with respect to the electric dipole moment (see section 2.3). Therefore, the spectra shown in figure 8 are limited to the $S_0 \rightarrow S_1$ transition (or the $S_1 \rightarrow S_0$ transition for the emission spectrum). This, however, is no limitation regarding the computed emission spectra, as the process of fluorescence in general occurs mostly only from the S_1 to the S_0 in the experiments, as well. Since the PDI derivative is the energy donor, the photophysical properties of

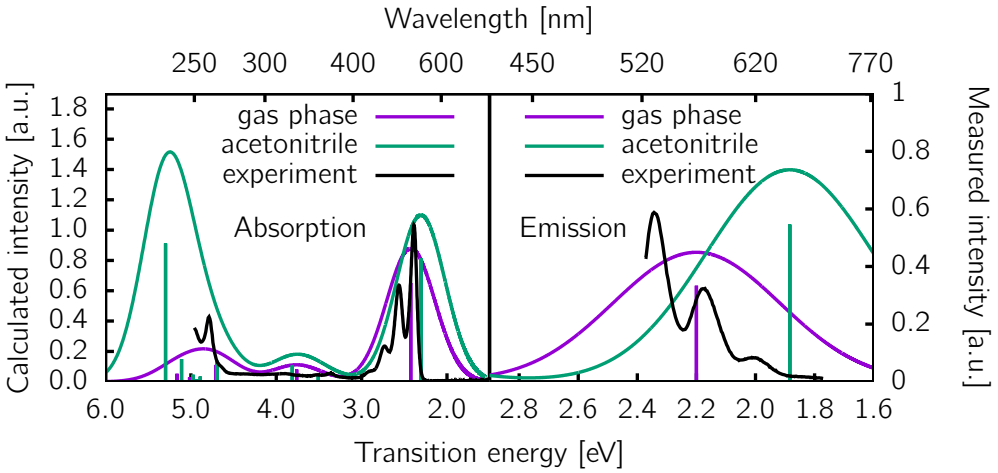

Environment	Excitation	Energy	Dipole Strength	Orbitals (contribution)[a]
gas phase	$S_0 \rightarrow S_1$	2.42 eV	11.0 a.u.	HOMO → LUMO (50%)
acetonitrile	$S_0 \rightarrow S_1$	2.31 eV	14.4 a.u.	HOMO → LUMO (50%)
gas phase	$S_1 \rightarrow S_0$	2.20 eV	11.7 a.u.	HOMO → LUMO (51%) HOMO ← LUMO (1.4%)
acetonitrile	$S_1 \rightarrow S_0$	1.88 eV	22.5 a.u.	HOMO → LUMO (50%)

[a] Only orbital contributions >1%.

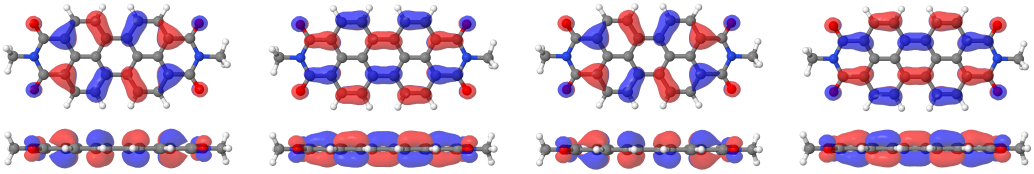

HOMO ground state geometry | **LUMO** ground state geometry | **HOMO** excited state geometry | **LUMO** excited state geometry

Figure 7: Computed TD-DFT absorption (top left) and emission (top right) spectra of C1-PDI-C1 in gas phase (purple line) and acetonitrile (green line). Oscillator strengths are drawn as vertical lines. For comparison, the corresponding experimental spectra of C4-PDI-C4 are shown in black. Details on selected excitations of C1-PDI-C1 are given below the spectra. The corresponding computed HOMO and LUMO of C1-PDI-C1 in acetonitrile are visualized at the bottom. MOs are shown at an isosurface cutoff of 0.03 a.u. The orbitals calculated in gas phase are included in appendix B.

C1-PDI-C1 are represented sufficiently by investigating S_0 and S_1. For the absorption spectrum, which serves as a reference, this restriction to the $S_0 \rightarrow S_1$ transition limits the analysis to the lower energy range (up to ca. 3 eV), while the higher energy transitions are being neglected.

Upon inclusion of nuclear vibrations into the computation of optical spectra, the theoretical results match the experiment fairly accurately (see figure 8), even though the calculations were performed on C1-PDI-C1, while the experimental spectra were recorded from C4-PDI-C4. This is a first indicator towards a small influence of the heteroaliphatic substituents on the photophysical properties. Yet, to achieve a good match between experiment and theory, the computed spectra have to be shifted towards higher transition energies by around 0.14 and 0.42 eV for gas phase and acetonitrile absorption, respectively, with the emission spectra having around 0.02 to 0.03 eV smaller shifts. Still, it is common for TD-DFT calculations to be offset from experimental results in absolute values well around ±0.5 eV[40, 75, 76]. Nevertheless, the relative agreement between theory and experiment is very good. The calculations correctly predict three distinct maxima, whose relative intensity differ only slightly from the experiment. With this, the combination of TD-DFT and FCHT calculations verifies that the three distinct peaks in the experimental emission spectrum arise from the same $S_1 \rightarrow S_0$ electronic transition, but the associated nuclear transitions are different for the individual maxima. The most intense transition is associated with the 0-0 transition, *i.e.,* from the vibrational ground state in S_1 to the vibrational ground state in S_0. The second most intense peak is associated with a transition from the vibrational ground state to the 14th vibrational level, the third most intense transition with an excitation to the 96th vibrational level in S_0 both in the gas phase and in acetonitrile. The overall intensity of the computed absorption in acetonitrile surpasses that of the gas phase calculation, while the intensities for the emission spectra are about similar. This stands in contrast to the standard TD-DFT calculations, where the oscillator strength of C1-PDI-C1 emission in acetonitrile is significantly larger than that in the gas phase. Additional FCHT calculations with different functionals are shown in appendix C.

As previously outlined, the calculation of the vibrationally-resolved spectra consists of the electronic part, as computed with the TD-DFT method, augmented with

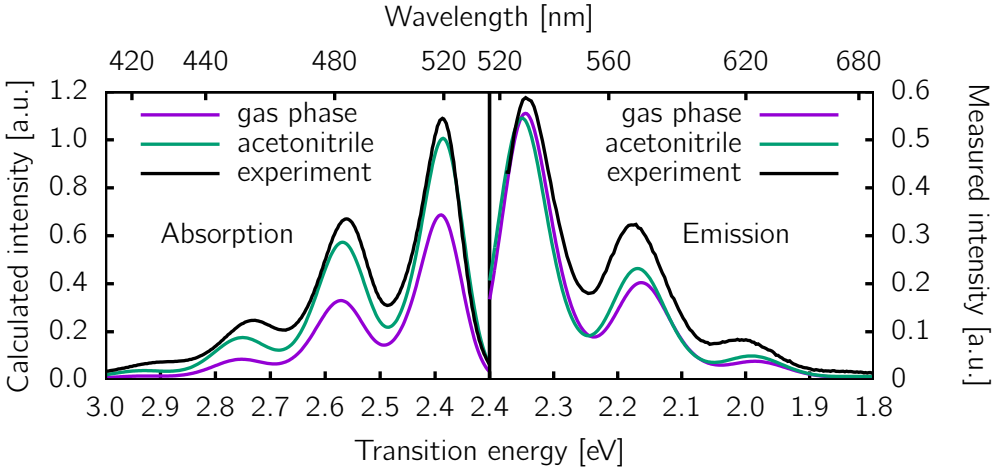

Figure 8: Computed TD-DFT/FCHT absorption (left) and emission (right) spectra of C1-PDI-C1 in gas phase (purple line) and acetonitrile (green line). For comparison, the corresponding experimental spectra of C4-PDI-C4 are shown in black. To better agree with the experimental findings, computed spectra were shifted by +0.14 eV (gas phase, absorption), +0.42 eV (acetonitrile, absorption), +0.11 eV (gas phase, emission) and +0.40 eV (acetonitrile, emission).

the nuclear contributions and their influence on the electric dipole moment within the Franck-Condon and Herzberg-Teller approximation (see section 2.3 and 3.1). The accuracy of the computed vibrationally-resolved spectra with respect to the experiment therefore validates the individual contributions, especially the electronic contributions and the applicability of TD-DFT to this problem. Even though the standard TD-DFT calculations fail to accurately predict the spectra when not augmented with nuclear contributions, the TDM calculation can be performed directly from the wave functions obtained from these, since TDMs are computed directly from the electronic wave function (see section 2.3). As a consequence, the vibrationally-resolved spectra presented in figure 8 serve as a validation of the level of theory, but they are not needed for the analysis of the TDMs, which are based on the electronic wave functions calculated with TD-DFT.

The first excited state is dominated by the single excitation wave function corresponding to transferring one electron from the highest occupied molecular orbital (HOMO) to the lowest unoccupied MO (LUMO) (see figure 7). Even though this transition merely contributes around 50% to the excited state wave function, the remaining 50% are comprised of single excitation wave functions with less than 1% total contribution each. Alone for the S_1 of the first excited state geometry of C1-PDI-C1 in the gas phase, the contribution of the de-excitation from the LUMO to the HOMO is somewhat more prominent at 1.4%. Both HOMO and LUMO consist of π-orbitals delocalized over nearly the entire planar chromophore main body, with the LUMO having one additional nodal plane compared to the HOMO. Virtually no electron density for those MOs is localized on the methyl substituents. As a result, the transition from S_0 to S_1 can be regarded as a $\pi\pi^*$-transition. Additionally, there are no considerable differences between the HOMOs or LUMOs when comparing ground state or first excited state structures.

The corresponding $S_0 \leftrightarrow S_1$ transition electric dipole moments (see figure 9) lie within the molecular plane along one of the molecules' symmetry axes. They differ between the various states and environments only in magnitude (see dipole strength in figure 7). The TDM is virtually perfectly aligned with the vector connecting the two nitrogen atoms. The quality of this alignment can be assessed by calculating the dot product of vector which connects both nitrogen atoms and the TDMs, such that 1 indicates parallelity, and 0 perpendicular vectors. On both ground and excited state geometries, no matter the environment, the dot product is between 0.9999999 and 1.0, which means that the vectors are indeed parallel.

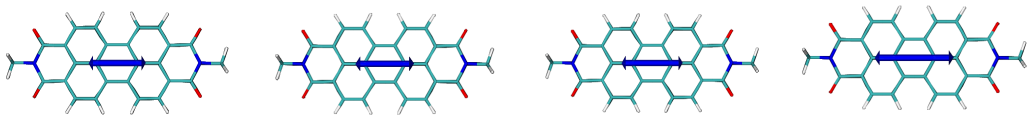

gas phase ground state geometry | **gas phase** excited state geometry | **acetonitrile** ground state geometry | **acetonitrile** excited state geometry

Figure 9: $S_0 \leftrightarrow S_1$ transition electric dipole moments of C1-PDI-C1. The dipole strength is represented in the magnitude of the vectors.

C4-PDI-C4 The inclusion of heteroaliphatic substituents from C1-PDI-C1 to C4-PDI-C4 open up a sizeable conformer space for the latter. As a result, to assemble a complete picture of the photophysical properties of C4-PDI-C4, one single minimum structure is not sufficient, but multiple local minimum structures representative of the

entire conformational space have to be computationally generated and evaluated. For the computational details of the ensemble generation see section 3.1.

The total number of C4-PDI-C4 conformers within an energy window of 7 kcal/mol with respect to the structure of lowest energy generated with CREST (2273 conformers), was reduced to 1000 using the PCA and k-means clustering algorithm within the CREST program package. It was assured that this reduced ensemble covered the entire 7 kcal/mol energy range, with the 1000th structure being exactly 7.0 kcal/mol higher in energy compared to the global minimum.

Single point energy calculations with the BP86 functional were performed on these 1000 representative conformers. The correlation between relative BP86 and GFN2-xTB energies is shown in figure 10. In general, the majority of conformers yield higher relative BP86 energies compared to the GFN2-xTB energies, such that only 561 conformers remain within the energy window of 7 kcal/mol with respect to the most stable structure in BP86 energies. These 561 conformers were Boltzmann-weighted using CREST. According to this, the lowest 100 conformers make up for over 99.4% of this population, with the 100th conformer being 4.2 kcal/mol higher in energy compared to the most stable conformer. Therefore, only these 100 representative structures were elected for further analysis.

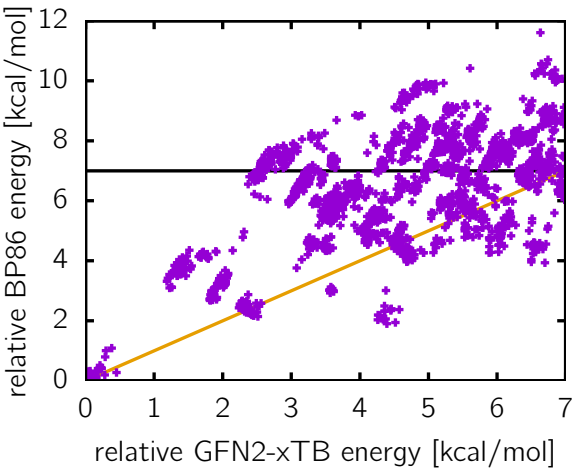

Figure 10: GFN2-xTB vs. BP86 energies on the GFN2-xTB geometries of C4-PDI-C4. The black line denotes 7 kcal/mol in relative BP86 energies, the yellow line identical GFN2-xTB and BP86 energies.

To evaluate the accuracy of the BP86 single point calculations that were the basis for the selection of the remaining 100 conformers, single point calculations as well as geometry optimizations were performed for these 100 structures on the B3LYP/def2-SVP level of theory, *i.e.*, the same setup as used for the computation of the photophysical properties. As can be seen in figure 11, there is a strong correlation between the BP86 and B3LYP single point energies, with the B3LYP functional generating slightly higher relative energies. Considering the B3LYP geometry optimizations, the overall energy trend is still quite close to the single point calculations, with some quite notable exceptions, where for instance conformers with a relative BP86 energy of over 3.5 kcal/mol yield relative energies of nearly 0 kcal/mol after optimization with B3LYP. These very close energies indicate a convergence of these conformers to the global minimum within the here explored ensemble. Some conformers yield higher relative B3LYP energies after optimization compared to the B3LYP single point energies. This somewhat unintuitive occurence of energies "rising" upon geometry optimization can be attributed

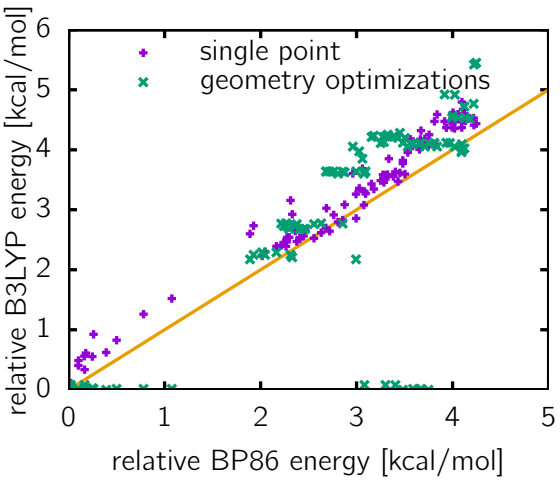

Figure 11: BP86 vs. B3LYP energies on the 100 final conformers of C4-PDI-C4. BP86 and B3LYP single points were computed on the GFN2-xTB geometries, while for B3LYP additional geometry optimizations were conducted. The yellow line denotes identical BP86 and B3LYP energies.

to the fact that energies are given relative to the most stable conformer, so that some conformers were stabilized to a less extend by the geometry optimization than the reference structure, resulting in higher relative energies. Since the cost-effective BP86 functional, however, yields qualitative very comparable results with respect to the B3LYP calculations, this justifies the usage of BP86 for reducing the ensemble from 1000 to 100 representative conformers based on energetic criteria. While identifying the ideal setup for the generation of a representative ensemble, additional calculations were performed. These are shown in appendix C.

The structures of the 100 final molecules of C4-PDI-C4 are displayed in figure 12 overlaid. Apparently, the inclusion of the heteroaliphatic substituents barely influences the geometry of the aromatic plane of PDI. However, the substituents themselves take on many different conformations. The computed TD-DFT absorption and emission spectra of these 100 representative C4-PDI-C4 conformers are shown in figure 13.

The spectra of these conformers are very similar to one another and also qualitatively alike to the C1-PDI-C1 TD-DFT spectra (compare figure 7), already indicating very minor influence of the addition as well as the arrangement of the heteroaliphatic substituents. Especially the $S_0 \rightarrow S_1$ and $S_1 \rightarrow S_0$ transitions are very comparable

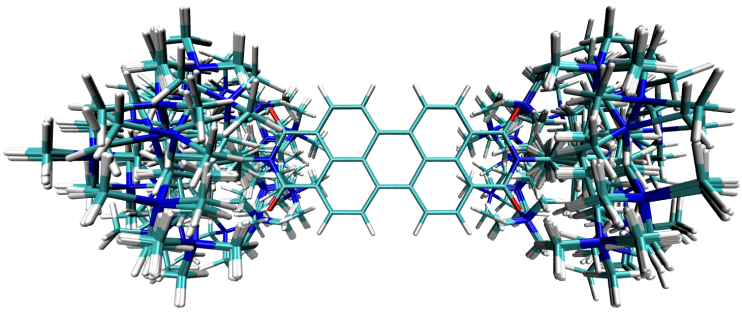

Figure 12: Overlaid structures of the 100 representative C4-PDI-C4 conformers. The atoms of the conformers' molecular plane were aligned for this representation.

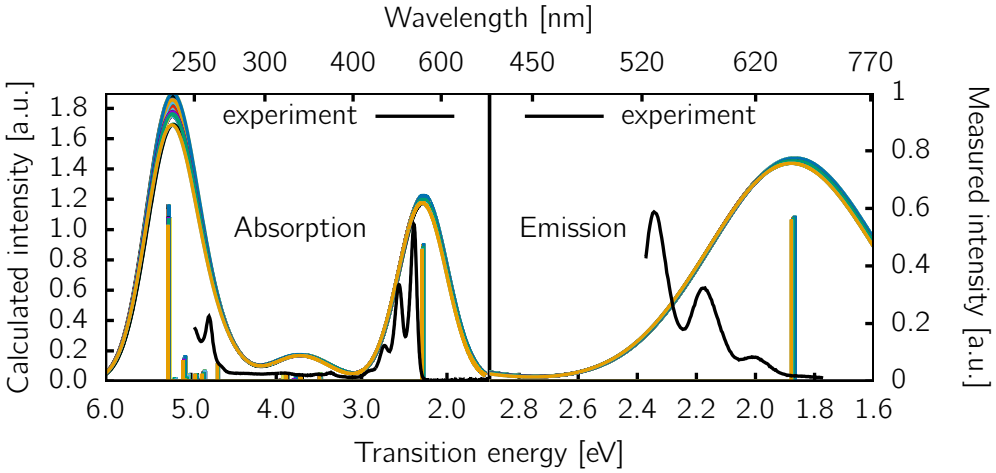

Type	Energy	Dipole Strength	Orbitals (contribution)[a]
absorption	2.27 to 2.29 eV	15.6 to 16.3	HOMO → LUMO (50%)
emission	1.87 to 1.88 eV	23.2 to 23.9	HOMO → LUMO (50%)

[a] Only orbital contributions >1%.

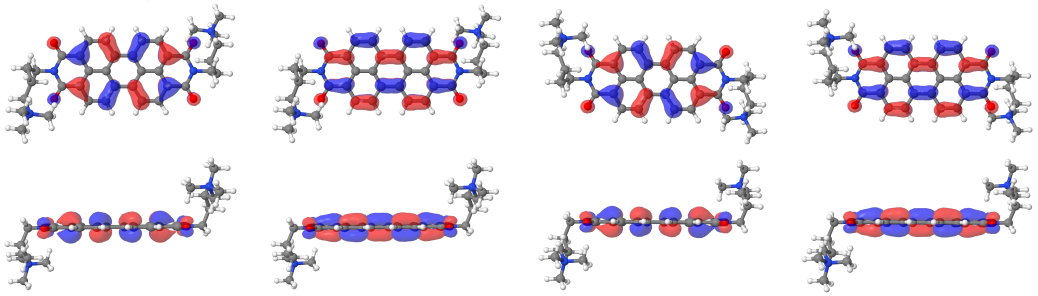

HOMO ground state geometry | **LUMO** ground state geometry | **HOMO** excited state geometry | **LUMO** excited state geometry

Figure 13: Computed TD-DFT absorption (top left) and emission (top right) spectra of 100 C4-PDI-C4 conformers in acetonitrile (multiple colored lines). Oscillator strengths are drawn as vertical lines. For comparison, the corresponding experimental spectra are shown in black. Details on the $S_0 \rightarrow S_1$ and $S_1 \rightarrow S_0$ excitations are given below the spectra. The corresponding computed HOMO and LUMO of of the most stable C4-PDI-C4 conformer in acetonitrile are visualized at the bottom. MOs are shown at an isosurface cutoff of 0.03 a.u.

in energy and intensity between all conformers (see figure 13). However, the standard TD-DFT spectra again lack resolution compared to the experiment. Therefore, vibrationally-resolved spectra were computed employing the FCHT approximations analogously to the computations done for C1-PDI-C1. The vibrationally-resolved spectra for the 100 representative C4-PDI-C4 conformers are shown in figure 14.

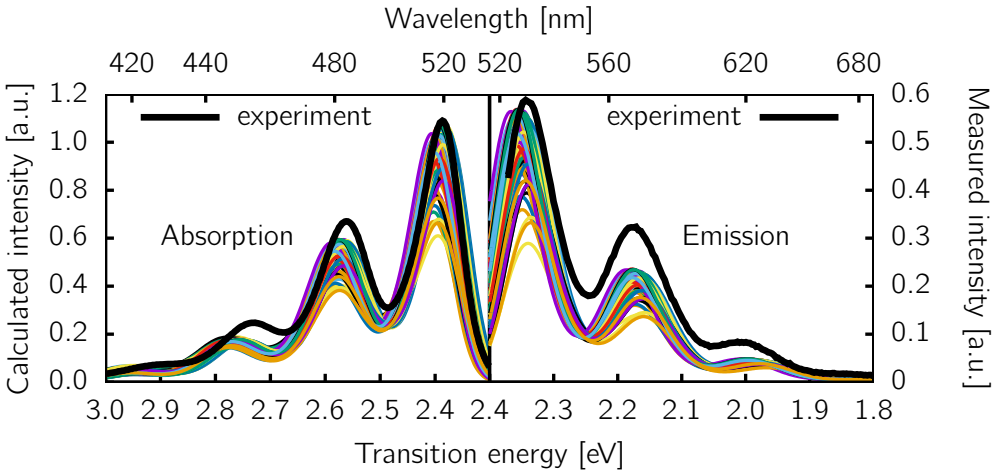

Figure 14: Computed TD-DFT/FCHT absorption (left) and emission (right) spectra of 100 C4-PDI-C4 conformers in acetonitrile (multiple colored lines). For comparison, the corresponding experimental spectra are shown in black. To better agree with the experimental findings, computed spectra were shifted by +0.44 eV (absorption) and +0.42 eV (emission).

The vibrationally-resolved spectra of the 100 C4-PDI-C4 conformers are very similar to one another and alike to these of C1-PDI-C1 (see figure 8). While varying in intensity, the peak positions spread only very little between the conformers, with a total range from 2.345 to 2.376 eV (values after the shifting) of the 0-0 transition in the case of emission. The relative intensities of the peaks appear to be overall mostly constant, such that, apart from smaller deviations, the conformers with the greatest intensity for the 0-0 transition exhibit the most intense peaks relative to the other conformers for the remaining transitions, as well, and *vice versa*. Additionally, conformers with a high absorption intensity also display elevated emission spectra. Overall, all calculated spectra are in good agreement with the experimentally recorded spectra. To obtain a definite, representative spectrum for the ensemble, all 100 conformers were Boltzmann-weighted according to the B3LYP ground state energy of the optimized structure using the sorting algorithm implemented in CREST. The computed spectra displayed in figure 15 were generated by linear combination of the single spectra, with the Boltzmann-weights being the linear coefficients. These weighted absorption and emission spectra coincide very well with the experimental spectra, validating the accuracy of the computations.

Again, for the analysis of the electronic properties, only the TD-DFT calculations will be investigated, while the vibrationally resolved spectra serve as validation of the level of theory.

The S_1 wave function of C4-PDI-C4 is generated from the ground state by transferring an electron from the HOMO to the LUMO with a weight of 50% for all 100 conformers with next to no variation between the structures (see figure 13), with all other single-electron wave function contributions being well below 1%. This holds true for both the optimized ground state and first excited state structures. The HOMOs and LUMOs of C4-PDI-C4 are qualitatively identical to those of C1-PDI-C1 (compare figures 7 and 13), with virtually no electron density located on the heteroaliphatic sub-

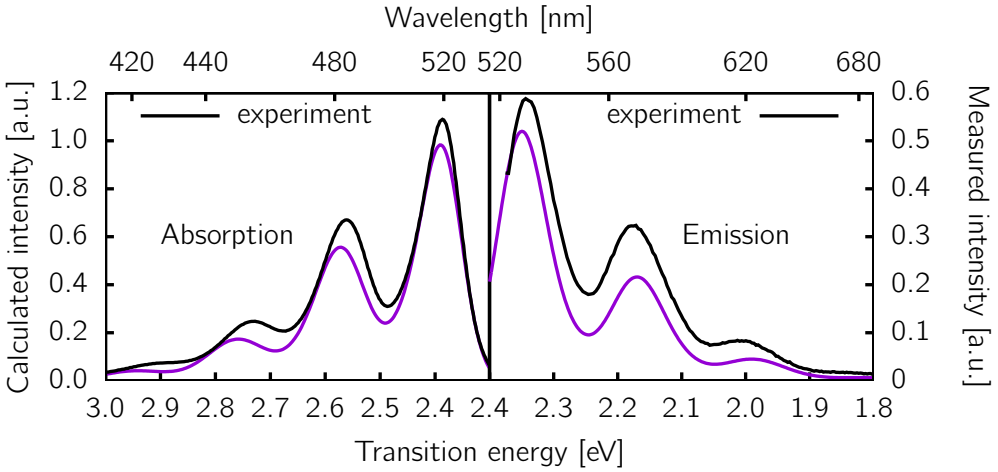

Figure 15: Boltzmann-weighted average of the computed TD-DFT/FCHT absorption (left) and emission (right) spectra of 100 C4-PDI-C4 conformers in acetonitrile (purple line). For comparison, the corresponding experimental spectra are shown in black. To better agree with the experimental findings, computed spectra were shifted by +0.44 eV (absorption) and +0.42 eV (emission).

stituents, explaining the minuscule influence of the conformation on the photophysical properties of C4-PDI-C4.

The influence of the conformation on the $S_1 \rightarrow S_0$ TDMs is vanishingly low. The dot product of the vector connecting the two nitrogen atoms within the molecular plane (N_1 and N_2 in figure 6) and the TDM is almost 1 for all conformers. This means that both vectors are effectively parallel. In the most extreme case, the scalar deviates from 1 by 0.03%, which is little over 1° deflection. Also the deviation in magnitude is limited (see figure 13). Computing the Boltzmann-weighted TDM yields 23.6 (atomic units) for the conformational ensemble.

4.1.2 Ruthenium complex

The modified $Ru(bpy)_3$ chromophores serve as energy acceptors. Therefore, contrary to the PDI derivatives, the absorption properties are of major interest. Thus, the absorption spectra and corresponding TDMs for $Ru(bpy)_2$bpyC1 and the conformational ensemble of $Ru(bpy)_2$bpyC9 presented in the this section, are computed on the optimized ground state structures.

$Ru(bpy)_2$bpyC1 Excited states of $Ru(bpy)_2$bpyC1 were computed on the optimized ground state structure in gas phase and acetonitrile. The TD-DFT absorption spectra are shown in figure 16.

The overall agreement between theory and experiment is quite good, as both describe a local absorption maximum in the low energy range between 2.5 and 3 eV, and a substantial rise in absorption above 3.5 eV. The theory fails to correctly predict the high-energy range above 4 eV, which can be attributed to a restriction to 30 excited states, with the excited state highest in energy appearing at 4.21 or 4.26 eV in gas phase or acetonitrile, respectively. This is not an issue, however, as the emission of PDI levels off above around 2.5 eV (see figure 15). The spectral overlap will be investigated in more detail in section 4.1.3. As a result, only the spectral window below 3 eV in the absorption spectrum of $Ru(bpy)_2$bpyC1 needs to be considered, and therefore the TD-DFT calculations describe the absorptive effects of $Ru(bpy)_2$bpyC1 accurately enough for the purposes of this work.

The spectral window below 3 eV in the absorption spectrum of $Ru(bpy)_2$bpyC1 (see figure 16) is dominated by four distinct transitions both in gas phase and in acetonitrile. These include the transitions from the S_0 to S_5, S_6, S_7, and S_8. All absorptions are red-shifted in acetonitrile compared to the gas phase calculations, and simultaneously more intense. Only the $S_0 \rightarrow S_6$ transition is barely affected by the environmental change. The relative contributions of the one-electron wave functions to the excited states are identical between the environments, while they slightly differ in absolute weights.

All significant one-electron wave functions, *i.e.*, those contributing no less than 1% to the four selected excited states, are comprised of transferring an electron from either the second or third highest occupied MO to on of the three lowest unoccupied MOs. These orbitals are displayed in figure 17. The HOMO itself, which exhibits a distinct metal-centered d_{z^2} character, does not significantly contribute to either of the S_5, S_6, S_7, or S_8. In general, all the three highest occupied MOs comprise mostly metal-centered orbitals, while the three lowest-lying unoccupied molecular orbitals mostly display π-character delocalized over the ligands. The electron density of the LUMO and LUMO+1 is mostly delocalized over the unmodified bipyridine ligands, while LUMO+2 is delocalized over the sp^2 framework of the methylated ligand, thus rendering all the transitions from S_0 to S_5 through S_8 metal-ligand charge transfers. Furthermore considering that the LUMO and LUMO+1 are mostly localized on the unsubstituted bipyridine ligands, while LUMO+2 mostly comprises of π-orbitals on the modified bipyridine, this implies that excitation to the S_5 transfers electron density onto the unmodified ligands when compared to the ground state electron density. This is also mostly true for the S_6 and S_8 transitions, even though these excitations already exhibit non-negligible LUMO+2 character. The S_7 excited state wavefunctions exhibits the largest LUMO+2 character of all excited state wavefunctions investigated here. As a result, compared to the ground state electron density, excitation to S_7 increases the electron density on the modified ligand.

The TDMs of $Ru(bpy)_2$bpyC1 corresponding to the four transitions of interest (see figure 16) cluster into two groups — those parallel to the principal C_2 symmetry axis,

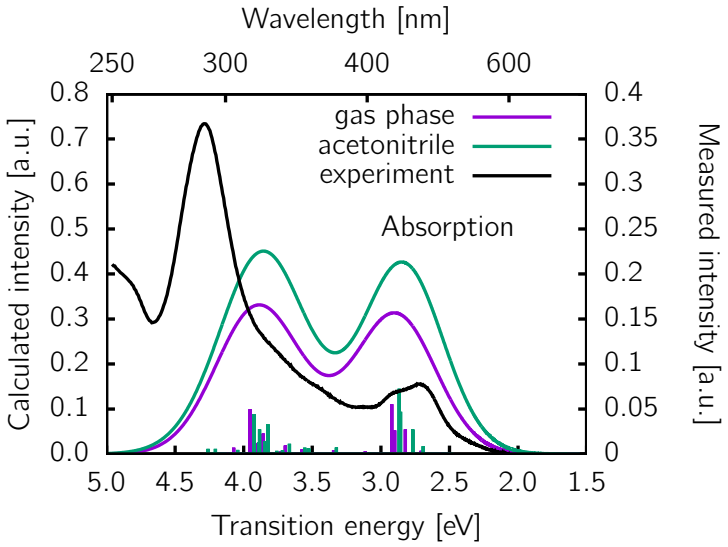

Environment	Excitation	Energy	Dipole Strength	Orbitals (contribution)[a]
gas phase	$S_0 \rightarrow S_5$	2.71	0.109	HOMO-1 → LUMO (43%) HOMO-2 → LUMO+1 (5%)
gas phase	$S_0 \rightarrow S_6$	2.82	0.794	HOMO-2 → LUMO (33%) HOMO-2 → LUMO+2 (10%) HOMO-1 → LUMO+1 (7%)
gas phase	$S_0 \rightarrow S_7$	2.90	0.741	HOMO-2 → LUMO+2 (36%) HOMO-1 → LUMO+1 (9%) HOMO-2 → LUMO (4%)
gas phase	$S_0 \rightarrow S_8$	2.92	1.55	HOMO-2 → LUMO+1 (25%) HOMO-1 → LUMO+2 (18%) HOMO-1 → LUMO (6%)
acetonitrile	$S_0 \rightarrow S_5$	2.69	0.267	HOMO-1 → LUMO (44%) HOMO-2 → LUMO+1 (4%) HOMO-1 → LUMO+2 (1%)
acetonitrile	$S_0 \rightarrow S_6$	2.77	0.807	HOMO-2 → LUMO (33%) HOMO-2 → LUMO+2 (12%) HOMO-1 → LUMO+1 (5%)
acetonitrile	$S_0 \rightarrow S_7$	2.86	1.35	HOMO-2 → LUMO+2 (32%) HOMO-1 → LUMO+1 (13%) HOMO-2 → LUMO (4%)
acetonitrile	$S_0 \rightarrow S_8$	2.87	2.07	HOMO-2 → LUMO+1 (24%) HOMO-1 → LUMO+2 (20%) HOMO-1 → LUMO (5%)

[a] Only orbital contributions >1%.

Figure 16: Computed TD-DFT absorption spectra of $Ru(bpy)_2bpyC1$ in gas phase (purple line) and acetonitrile (green line). Oscillator strengths are drawn as vertical lines. For comparison, the corresponding experimental spectrum of $Ru(bpy)_2bpyC9$ is shown in black. Details on selected excitations are presented underneath. The corresponding orbitals are visualized in figure 17.

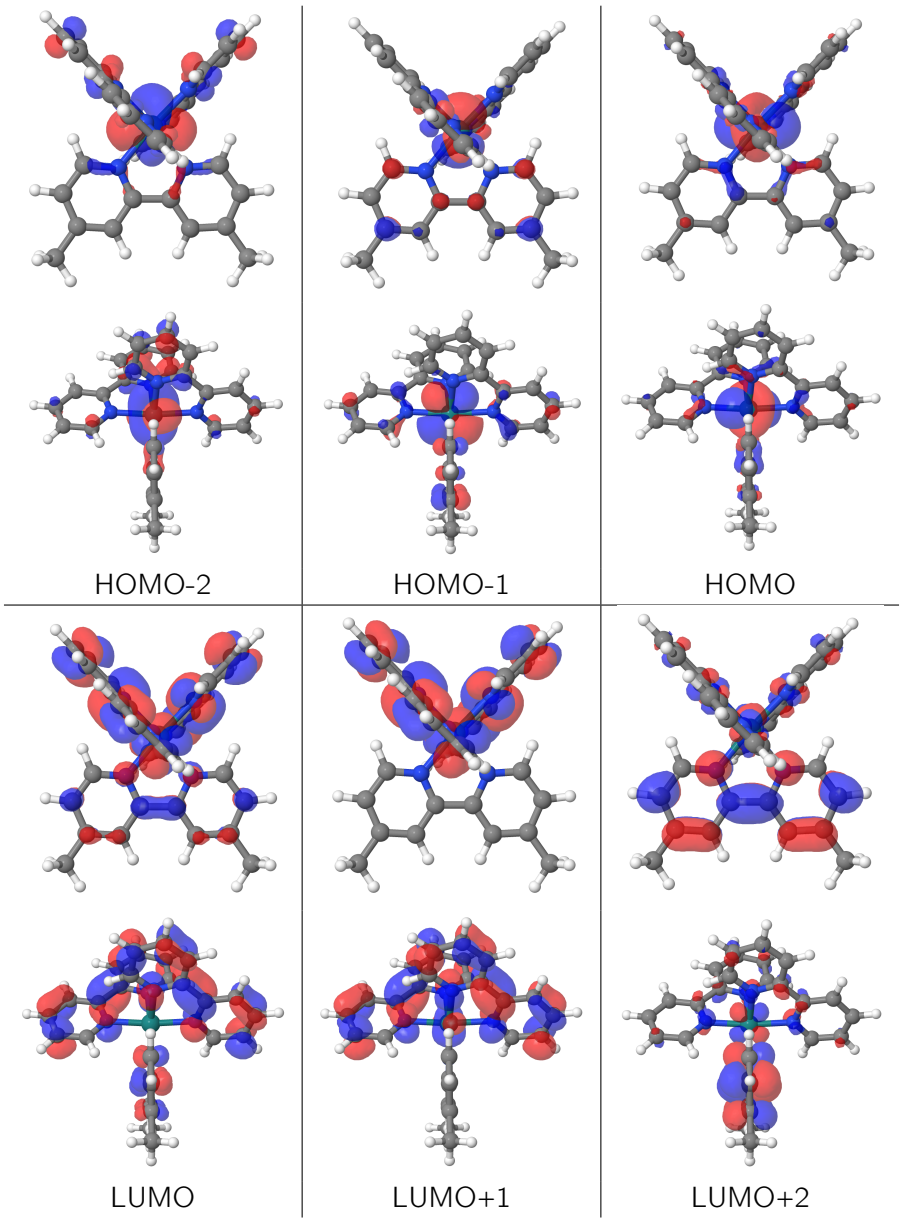

Figure 17: Computed orbitals of $Ru(bpy)_2bpyC1$ in acetonitrile from HOMO-2 to LUMO+2. Molecular orbitals are shown at an isosurface cutoff of 0.03 a.u. The orbitals of the gas phase calculations are included in appendix B.

and those perpendicular (see figure 18). The transitions from S_0 to S_5 and S_8 belong to the first, those to S_6 and S_7 to the second group. Aside from the magnitude of the vectors, which is governed by the dipole strength (see figure 16), there is virtually no difference between the TDMs in the gas phase and acetonitrile.

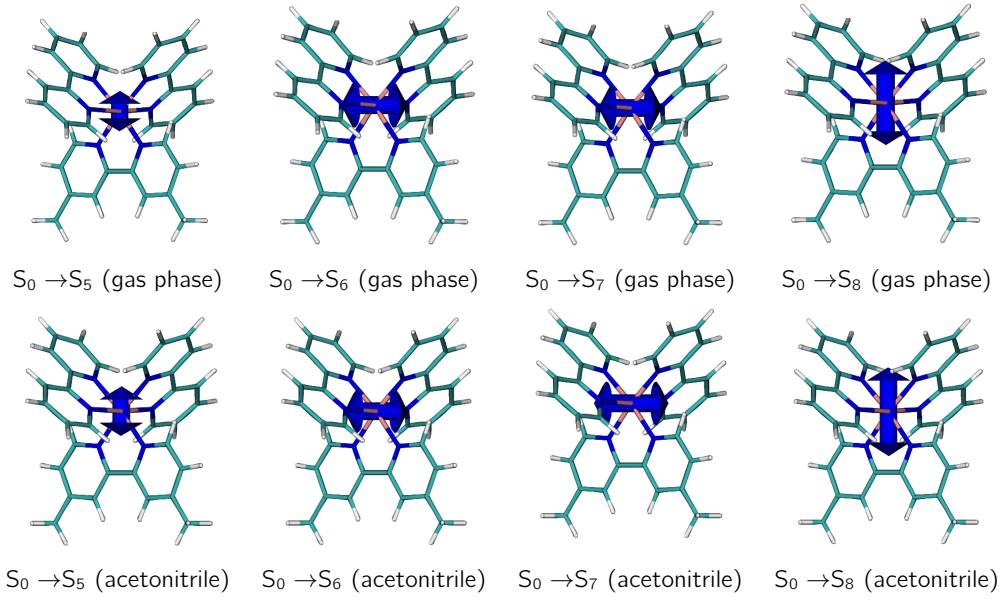

Figure 18: Transition electric dipole moments of $Ru(bpy)_2bpyC1$.

Since the TDMs in $Ru(bpy)_2bpyC1$ do not align with a distance vector between two atomic coordinates, they have to be described as linear combinations of nitrogen atom coordinates as

$$\vec{c} = \begin{pmatrix} c_x \\ c_y \\ c_z \end{pmatrix} = \sum_{n=1}^{6} w_{Nn} \begin{pmatrix} Nn_x \\ Nn_y \\ Nn_z \end{pmatrix} \tag{42}$$

where w_{Nn} is the contribution of the nitrogen atom n, and Nn_x, Nn_y, and Nn_z are the respective coordinates of the nitrogen atom n. The numbering of the nitrogen atoms is given in figure 6. This way, two different linear combinations for the each of the TDM orientations were constructed. The mode describes hereby, whether the vector is parallel or perpendicular to the principal symmetry axis. The weights for the four excitations of interest are given in table 1.

Excitation	w_{N1}	w_{N2}	w_{N3}	w_{N4}	w_{N5}	w_{N6}	mode
$S_0 \rightarrow S_5$	1	1	0	-1	-1	0	parallel
$S_0 \rightarrow S_6$	1	-1	-2	-1	1	2	perpendicular
$S_0 \rightarrow S_6$	1	-1	-2	-1	1	2	perpendicular
$S_0 \rightarrow S_8$	1	1	0	-1	-1	0	parallel

Table 1: Weights for the definition of transition electric dipole moments in terms of nitrogen nuclear coordinates in $Ru(bpy)_2bpyC1$. The numbering scheme for the Nitrogens is shown in figure 6.

The quality of this parametrization was assessed by calculating the dot product of the nuclear coordinate's linear combination vector and the TDM vector. These linear combinations describe the directionality of the TDMs fairly accurately, will all eight combinations (excitations to S_5 through S_8 for gas phase and acetonitrile) yielding

dot products between the linear combination and TDM of better than 99.99%, which corresponds to a deviation of less than 1°.

Ru(bpy)$_2$bpyC9 Analogously to C4-PDI-C4 (see section 4.1.1), the inclusion of aliphatic substituents to Ru(bpy)$_2$bpyC1 to obtain Ru(bpy)$_2$bpyC9 results in the potentiality of a manifold of conformers. Since the substituents in Ru(bpy)$_2$bpyC9 are longer than those in C4-PDI-C4, the conformational space increases accordingly. To save computational resources, the number of calculated conformers was limited by excluding the structure-crossing step from the CREST calculation generating the conformational ensemble. Nevertheless, the Ru(bpy)$_2$bpyC9 ensemble comprised 38399 conformers within the energy window of 7 kcal/mol starting from the most stable structure. This number of conformers was reduced to 1000 by PCA and k-means clustering. Again, it was ensured that these 1000 conformers spanned the entire energy range of the initial ensemble, with the 1000th conformer being 6.72 kcal/mol higher in GFN2-xTB energy than the global minimum structure. For these 1000 conformers, BP86 single point calculations were performed (see figure 19).

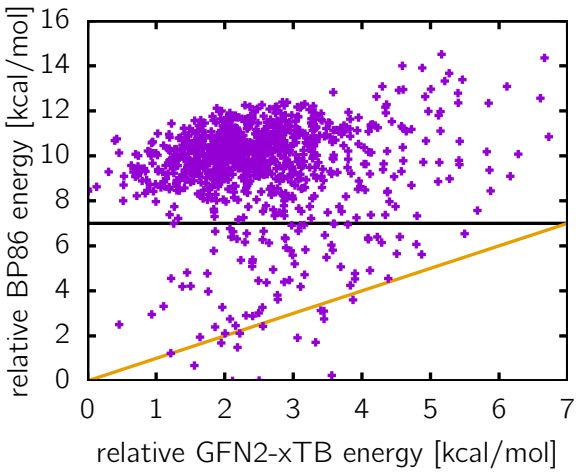

Figure 19: GFN2-xTB vs. BP86 energies on the GFN2-xTB geometries of Ru(bpy)$_2$bpyC9. The black line denotes 7 kcal/mol in relative BP86 energies, the yellow line identical GFN2-xTB and BP86 energies.

It is apparent that GFN2-xTB overestimates the stability of a lot of the conformers. From those 1000 conformers, merely 92 yielded BP86 single point energies within the energy range of 7 kcal/mol with respect to the most stable conformer. Within these 92 conformers, in turn, there is some weak correlation between GFN2-xTB and BP86 energies, but the values still spread a wide range. These 92 conformers were selected as final structures representative of the entire conformational space and were optimized on the B3LYP/def2-SVP level of theory. The B3LYP energies on the structures optimized with B3LYP as well as using GFN2-xTB are shown in figure 20. Similarly to the results presented for C4-PDI-C4 in section 4.1.1, there is a high correlation between BP86 and B3LYP single point energies, justifying the use of the cheaper BP86 functional for an ensemble reduction based on energetic parameters. However, most of the 92 conformers yield significantly higher relative energies after geometry optimization. This causes the five most stable conformers to already account for over 99% of the ensemble when Boltzmann-weighted. Nevertheless, to evaluate the aliphatic substituents' effect on the photophysical properties of Ru(bpy)$_2$bpyC9, excited state calculations were performed on all 92 conformers. These conformers are collectively shown in figure 21.

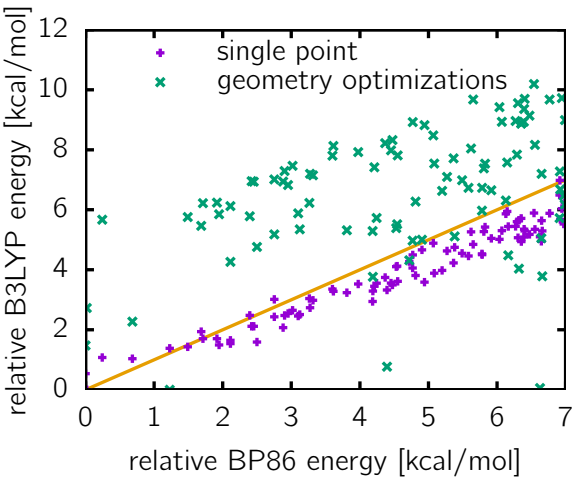

Figure 20: BP86 vs. B3LYP energies on the 92 final conformers of Ru(bpy)2bpyC9. BP86 and B3LYP single points were computed on the GFN2-xTB geometries, while for B3LYP additional geometry optimizations were conducted. The yellow line denotes identical BP86 and B3LYP energies.

Contrary to what has been observed for C4-PDI-C4, the conformation of the aliphatic substituents does influence the geometry of the three bipyridine frameworks, leading to some distortion of the aromatic planes. The substituents' conformations range from almost linear to completely bend around the core of the complex.

The TD-DFT absorption spectra for the 92 representative conformers of $Ru(bpy)_2bpyC9$ are shown in figure 22. The orbitals are shown in appendix B. Qualitatively, the spectra are very comparable in overall intensity between all conformers. However, in the range of interest between 2.5 and 3 eV, the conformers cause the transition energies to vary, such that no distinct transitions can be attributed to any region. This becomes especially apparent in figure 23, where the individual excitations are color coded based on the energetic ordering within each conformer. The transitions displayed include S_4, S_5, S_6, S_7, and S_8, omitting S9, as these transitions only occur

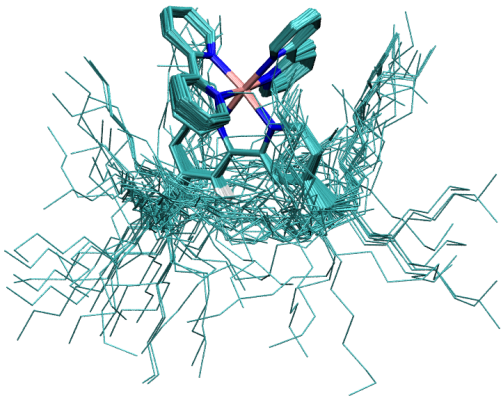

Figure 21: Overlaid structures of the 92 representative $Ru(bpy)_2bpyC9$ conformers. The atoms of the central three bipyridine framework, including the metal center, were aligned for this presentation, and this moiety is represented with larger bond radii compared to the aliphatic substituents. Hydrogen atoms are not drawn for clarity reasons.

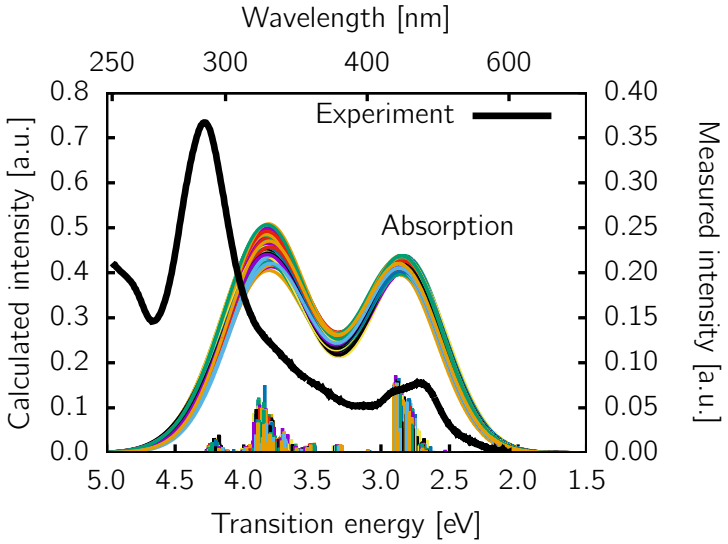

Figure 22: Computed TD-DFT absorption spectra of 92 Ru(bpy)$_2$bpyC9 conformers in acetonitrile (multiple colored lines). Oscillator strengths are drawn as vertical lines. For comparison, the corresponding experimental spectrum is shown in black.

at transition energies of over 3.05 eV. Furthermore, all $S_0 \rightarrow$S9 oscillator strengths are below 0.007. The transitions from S_0 to S_4, S_5 and S_6 mix very little, with especially the transitions to S_6 being well-seperated from the other transitions in their combination of transition energies and oscillator strengths. The energetic regions of S_4 and S_5 heavily overlap, but the S_5-transitions are distinctively intense enough compared to S_4 to assume that the energetic ordering of those two excited state wavefunctions does not change in most of the conformers.

The picture is different for the excitations to S_7 and S_8, which are similar in intensity and overlap significantly in transition energy, providing reason to assume that conformational changes stabilize and destabilize the S_7 and S_8 excited state wavefunctions in such a way that they exchange their rank when ordered by energy. In other words, the excited state wave function of one character, which is seventh in excitation energy for one conformer, might be eighth in energetic ordering for another conformer and *vice versa*.

This finding is further supported by an orientation analysis of the TDMs μ_A. The

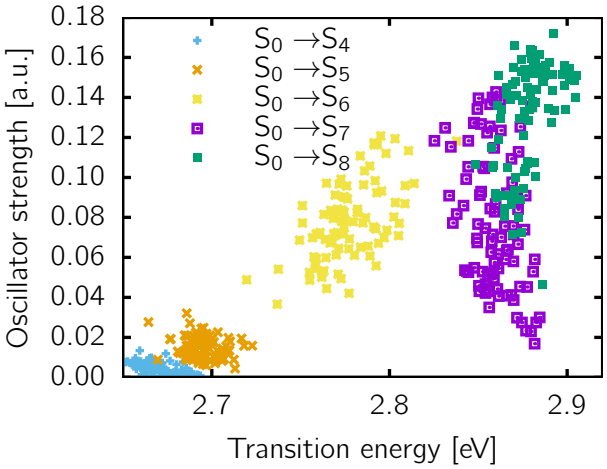

Figure 23: Oscillator strength and transition energies of the excitations to S_4 through S_8 of the 92 Ru(bpy)$_2$bpyC9 conformers.

squared dot product between these and the vectors generated as linear combinations of nitrogen atoms' nuclear coordinates were computed for both the parallel and the perpendicular mode ν_i as defined for Ru(bpy)$_2$bpyC1 (see table 1). Therefore, the closer the squared dot product is to 1, the more aligned this TDM is with the respective axis. The squared dot products for the TDMs corresponding to the transition to S_5, S_6, S_7, and S_8 of the 92 representative conformers are displayed in figure 24.

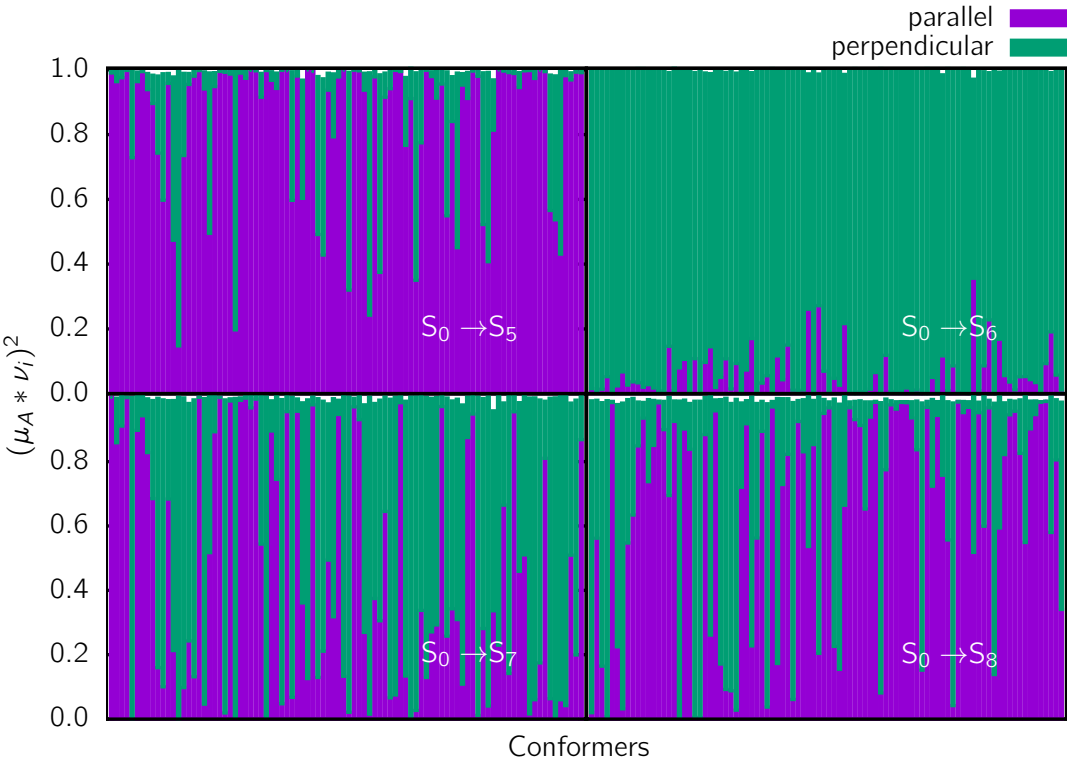

Figure 24: Squared dot product of the transition electric dipole moment vectors for the excitations to S_5 through S_8 and the linear combinations of nitrogen coordinates defined in table 1 for the 92 Ru(bpy)$_2$bpyC9 conformers.

Aside from minor fluctuations and a few major exceptions, the TDM of $S_0 \rightarrow S_5$ is aligned to the parallel mode, while the one of $S_0 \rightarrow S_6$ clearly exhibits perpendicular character for almost all conformers. This is in line with the observations that these two transitions mix negligible with other transitions. However, the fact that no unambiguous alignment can be assigned to for transitions, supports the statement that the S_7 and S_8 wave functions switch energetic rank between different conformers. Still, there appears to be a complementing characteristic to the alignment of the TDMs for $S_0 \rightarrow S_7$ and $S_0 \rightarrow S_8$. In cases, where a perpendicular character can be assigned to one of the excited states, the other one most often displays a parallel character and *vice versa*. This further supports the theory that not one wave function character can be assigned to S_7 or S_8, but that in fact both comprise two distinct wave functions which switch in energetic ordering as the molecule adopts a different conformation.

Nevertheless, even after complementing the S_7 and S_8 characters into a concise picture, the TDMs align poorly with either the parallel or the perpendicular modes. While there are cases in which a specific TDM is aligned almost perfectly with one of the modes, other TDMs exhibit dot products which are almost identical for both modes. This is true through all investigated excited states, even though the alignment is

especially bad for the TDMs corresponding to $S_0 \rightarrow S_7$ and $S_0 \rightarrow S_8$. Overall, however, it can be concluded that for each conformer, between the excitations to S_7 and S_8, one TDM aligns with either the parallel or the perpendicular mode, while the second one aligns with the respective other mode.

The Boltzmann-weighted spectrum of all 92 representative conformers of $Ru(bpy)_2bpyC9$ (see figure 25) represents the individual conformer spectra in that it describes the experiment reasonably well in the energy range below 3 eV, but it fails to predict the absorption properties correctly in the higher energy range, again due to the limitation on 30 excited states in the TD-DFT calculations. The Boltzmann-weighted TDM strengths (in atomic units) are 0.224 for the $S_0 \rightarrow S_5$ transition and 0.968 for $S_0 \rightarrow S_6$, while the $S_0 \rightarrow S_7$ and $S_0 \rightarrow S_8$ TDMs averaged together amount to 1.62 each. In this, the transitions are in general an order of magnitude less intense compared to those in C4-PDI-C4.

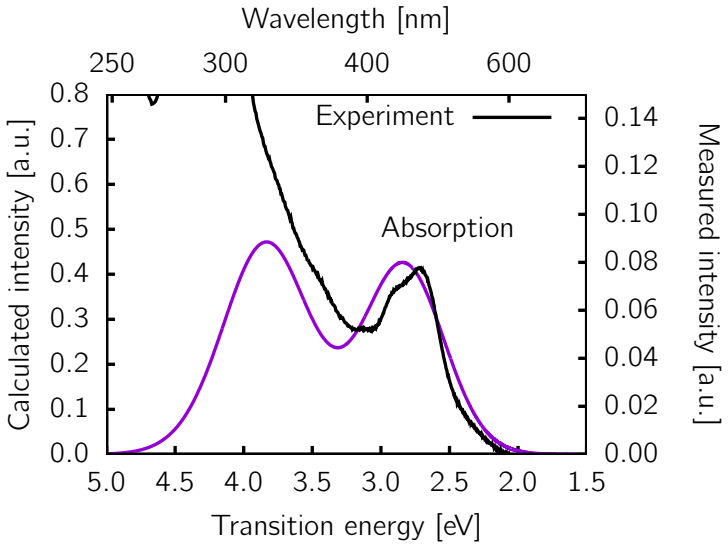

Figure 25: Boltzmann-weighted average of the computed TD-DFT absorption spectrum of 92 $Ru(bpy)_2bpyC9$ conformers in acetonitrile (purple line). For comparison, the corresponding experimental spectrum is shown in black.

4.1.3 Spectral overlap and orientation effects on FRET

The final Boltzmann-weighted, representative spectra for C4-PDI-C4 and $Ru(bpy)_2bpyC9$ are shown jointly in figure 26. The 0-0 peak in the C4-PDI-C4 spectrum overlaps with the low-energy end of the $Ru(bpy)_2bpyC9$ absorption profile.

The overlap integral was decomposed into the contributions of each of the four excitations investigated more closely in section 4.1.2 (see table 2). This was achieved by convoluting each of the transitions of interest in $Ru(bpy)_2bpyC9$ with one convolution function and subsequently calculating Boltzmann-weighted, normalized absorption profiles over the ensemble for each transition individually. Finally, the overlap between each of these profiles with the normalized C4-PDI-C4 spectrum was computed. The normalization of each spectrum was performed such that the integral over each individual spectrum was equal to the unit area. With this, the overlap can be expressed in cm according to the FRET rate equation (equation 1)[10].

Since the transitions to S_7 and S_8 are effectively degenerate and merely separable, they are presented as one integral. These integrals can be easily manipulated, as they heavily depend on the convolution functions — choosing more expanded convolution functions will naturally lead to increased overlaps of energetically distant transitions.

Excitation	spectral overlap / cm
$S_0 \rightarrow S_5$	2.12E-4
$S_0 \rightarrow S_6$	1.44E-4
$S_0 \rightarrow S_7$ + $S_0 \rightarrow S_8$	1.60E-4

Table 2: Calculated spectral overlap decomposed for each of the convolution functions of the transitions to S_5, S_6, S_7 and S_8 of $Ru(bpy)_2bpyC9$ with the total spectrum of C4-PDI-C4. Transitions to S_7 and S_8 are collected into only one integral.

Furthermore, especially the C4-PDI-C4 spectrum was shifted to better agree with experimental findings (see section 4.1.1). For the emission spectrum of C4-PDI-C4, the shift amounts to +0.42 eV. This shift was included for the computation of the overlap to best represent the experimental spectra. However, this shift includes a heavy bias. The overlaps for the non-shifted C4-PDI-C4 spectrum are about one order of magnitude smaller, demonstrating the arbitrariness of these computed overlaps. Therefore, it is important that the computed spectra agree well in shape and position with the experimental spectra, as has been demonstrated in the previous analysis. Nevertheless, the absolute overlap valued remain somewhat random and must not be interpreted as factual. Rather, they resemble a general idea of dimension, and especially provide invaluable insights into the relative significance of each of the individual transfers when compared to one another.

This being said, since the C4-PDI-C4 spectrum overlaps with the lower energy range of the $Ru(bpy)_2bpyC9$ absorption (see figure 26), the spectral overlap is largest for the transitions at lower excitation energy. As a result, the $S_0 \rightarrow S_5$ transition is associated with the largest spectral overlap, followed by $S_0 \rightarrow S_6$, while $S_0 \rightarrow S_7$ and $S_0 \rightarrow S_8$ jointly overlap about the same as $S_0 \rightarrow S_6$. This joint overlap, however, arises from two $Ru(bpy)_2bpyC9$ transitions both normalized, such that each of the transitions contribute an overlap of 8.00E-5 nm.

These overlaps have to be combined with the observation, that, after Boltzmann-weighting, the excitation $S_0 \rightarrow S_7$ and $S_0 \rightarrow S_8$ exhibit the most intense dipole strengths (1.62 a.u.), with $S_0 \rightarrow S_6$ (0.968 a.u.) being almost 50% less intense, while $S_0 \rightarrow S_5$ (0.224 a.u.) is less than 1/7th of the most intense dipole strength. In consequence,

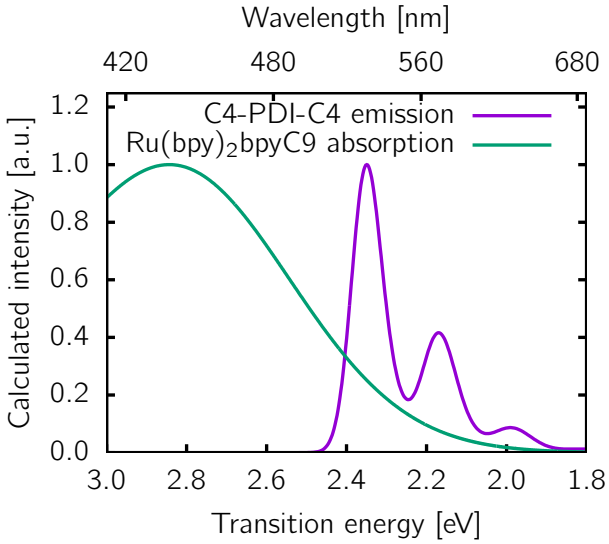

Figure 26: Spectral overlap between the emission spectrum of C4-PDI-C4 and absorption spectrum of $Ru(bpy)_2bpyC9$. Spectra shown are not-shifted the Boltzmann-weighted spectra averaging over the ensemble.

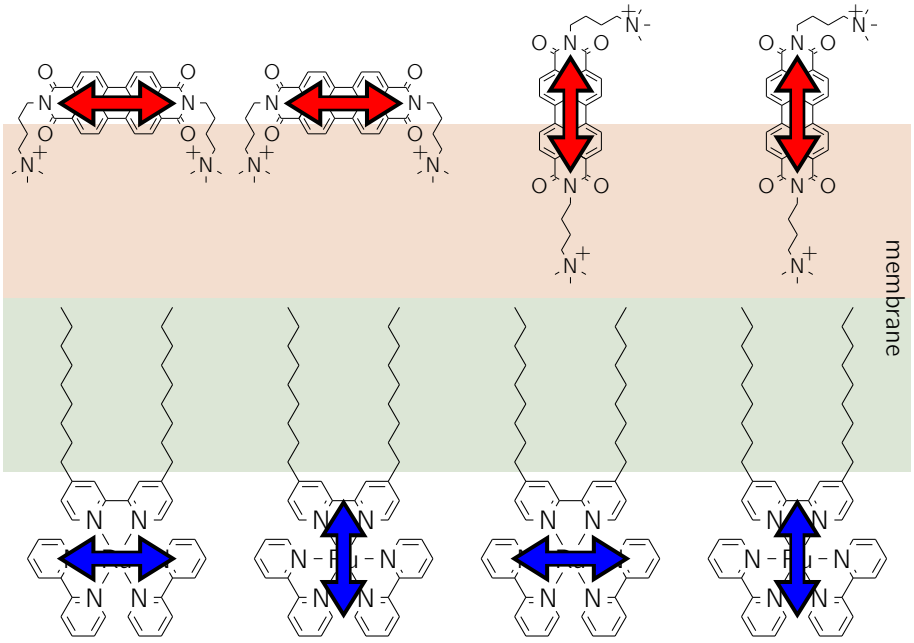

insertion[a]	tangential	tangential	normal	normal
mode[b]	perpendicular	parallel	perpendicular	parallel
θ_{AD}	0 to 90°	0°	0°	0°
θ_D	90°	90°	0°	0°
θ_A	90°	0°	90°	0°
κ^2	0 to 1	0	0	4

a Insertion of C4-PDI-C4 such that the TDM is either tangential or normal to the membrane surface.

b Alignment of the TDM for the corresponding transitions (see table 1) with respect to the principal symmetry axis in $Ru(bpy)_2bpyC9$, which is assumed to coincide with the vector normal to the membrane surface.

Figure 27: Effect of the insertion of C4-PDI-C4 into the membrane on the energy transfer.

the differences in dipole strength (which enters the FRET rate equation squared) and overlaps of the transitions to S_6, S_7 and S_8 almost cancel out, such that in an unconstrained environment, these three would contribute approximately the same amount, while the rate that populates S_5 is significantly reduced. This picture, however, is somewhat altered when the chromophores alignment is restricted by the embedding into a membrane. Assuming that $Ru(bpy)_2bpyC9$ inserts into the membrane in a way that both aliphatic C9 groups align with the aliphatic lipid chains, the principal symmetry axis would coincide with the vector normal to the membrane surface (see figure 27). As a result, the modes of the TDM orientation defined in table 1 correspond to the orientation of the TDM with respect to this normal vector. The TDMs arising from the $S_0 \rightarrow S_5$ and $S_0 \rightarrow S_8$ transitions align with the normal vector, while those corresponding to $S_0 \rightarrow S_6$ and $S_0 \rightarrow S_7$ stand perpendicular to this normal vector. For C4-PDI-C4, there are two different extreme chromophore arrangements into the membrane plausible, with both substitutents inserted into the membrane, or only one of them. In the first case, the TDM for the $S_1 \rightarrow S_0$ transition orientates tangential to the membrane surface, while it aligns with the normal vector in the latter scenario.

These orientations massively affect the FRET. With the TDM of C4-PDI-C4 being

tangential to membrane surface vector, in would be perpendicular to the TDMs of the $S_0 \rightarrow S_5$ and $S_0 \rightarrow S_8$ transitions, prohibiting any energy transfer to these excited states. At the same time, it could be parallel to the TDMs corresponding to $S_0 \rightarrow S_6$ and $S_0 \rightarrow S_7$. In this case, however, rotating C4-PDI-C4 and its TDM within the surface plane, which is not prohibited by embedding, would also originate perpendicular arrangements. Averaging over all arrangements of a donor-acceptor pair, where the TDMs of both are perfectly aligned with the membrane surface, yields a mean κ^2 of around 0.41 (for more details on this averaging see section 4.3), which is already significantly below the mean κ^2 in isotropic media of 2/3[25].

In contrast, if C4-PDI-C4 inserted into the membrane with one substituent only, the $S_1 \rightarrow S_0$ TDM coincides with the normal vector. In this normal arrangement, the C4-PDI-C4 TDM is perpendicular to the perpendicular mode corresponding to the $S_0 \rightarrow S_6$ and $S_0 \rightarrow S_7$ transitions in $Ru(bpy)_2bpyC9$, prohibiting any energy transfer, while the $S_0 \rightarrow S_5$ and $S_0 \rightarrow S_8$ TDMs are aligned with the C4-PDI-C4 TDM, resulting in the idealized case in an κ^2 of 4, which is the maximum possible value. Additionally, with these molecular orientations, rotation around the vector normal to the membrane surface does not impact the κ^2.

The orientation effects described here are limited to the extreme cases, while in reality there will be still some fluctuations around these simplified arrangements. Furthermore, the numbers presented are restricted to the chromophores being directly opposite in the membrane. Displacement along the membrane surface would result in non-extreme values for the angles between the TDMs and the connecting distance vector, giving rise to non-zero terms in the second part of equation 3. However, this would also coincide with a greater distance between the chromophores, again reducing the energy transfer rate.

Aside from these drawbacks, these simplified cases still allow to evaluate the general impact of chromophore restriction within the membrane on the FRET, deactivating some transitions while enhancing others. As described in section 4.1.2, the excitations of the respective excited states in $Ru(bpy)_2bpyC9$ cause different electron density shifts with respect to the ground state electron density distribution. As a result, with C4-PDI-C4 in the normal insertion, and thus energy transfer onto the S_5 and S_8 of $Ru(bpy)_2bpyC9$, gives rise to an increased electron density on the unmodified bipyridine ligands, *i.e.*, an electron transfer outwards from the membrane, while the energy transfer with C4-PDI-C4 in the tangential insertion causes a more balanced electron transfer onto the three ligands. Consequently, due to an impact on the excited electronic states and the electron density, the insertion of C4-PDI-C4 might affect the photosensitizing properties of $Ru(bpy)_2bpyC9$.

4.2 Molecular dynamics simulations

As previously outlined, the orientation of the TDMs has a significant influence on the FRET efficiency. It is to be expected that the membrane reduces the mobility of the inserted chromophores compared to isotropic solutions significantly, both with respect to the acceptor-donor distance as well as the arrangement of those relative to one another. Here, force-field based MD simulations are performed to monitor the evolution of the chromophores' position and orientation in time. Individual systems are generated for both chromophores, to track this progression for each of the inserted species independently. To minimize the bias induced by the selection of a starting geometry, different distances with respect to the center of the membrane are used as initial points. In these simulations, the distance of the inserted molecule with respect to the center of the membrane and the angle of the TDM vectors, as defined through the QM cal-

culations in section 4.1, relative to the membrane surface are monitored. Combining the insights provided by the simulations both for C4-PDI-C4 and $Ru(bpy)_2bpyC9$ embedded into the lipid bilayer and expanding this with the knowledge gained from the QM calculations enables to assess of the FRET efficiency.

4.2.1 PDI

As outlined in section 4.1.3, the orientation of C4-PDI-C4 when embedded into the lipid bilayer membrane is crucial to the efficiency of the FRET. With the two extreme orientations which C4-PDI-C4 adopt, the emission TDM is either aligned with the surface of the membrane in the so-called "tangential" insertion, or it points perpendicular, *i.e.*, "normal" to the surface. To minimize the bias induced into a starting geometry towards one of these two modes, individual simulations were performed for both, each with several distinct distances of the chromophore to the membrane center (see figure 28).

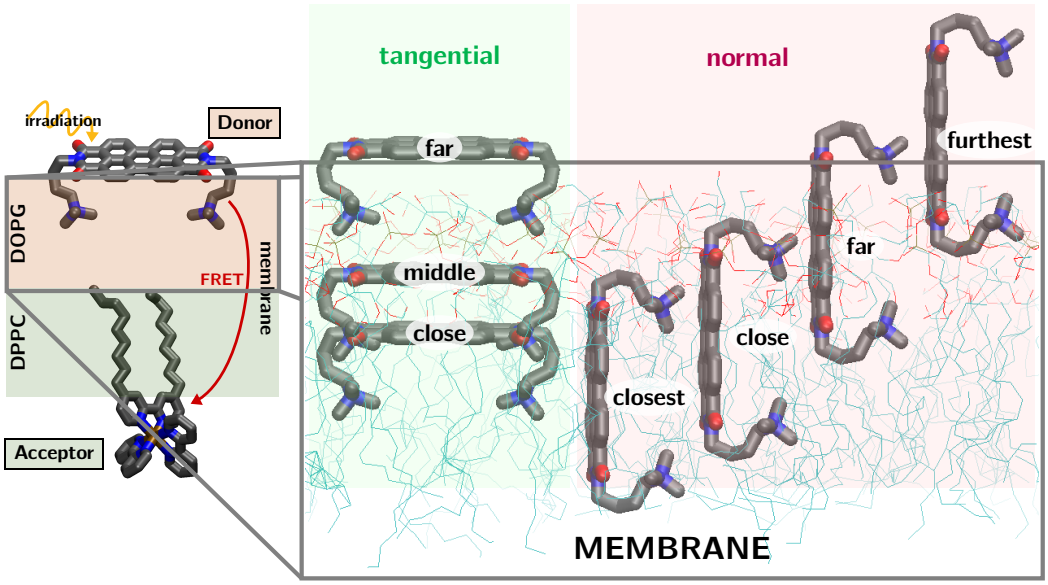

Figure 28: Insertions of C4-PDI-C4 into the membrane. Atoms and bonds are colored by element: cyan and grey for carbon in lipids and ligand, respectively, blue for nitrogen, red for oxygen and ochre for ruthenium. For clarity purposes, only lipid head moieties are displayed, while aliphatic lipid tails are not included. Hydrogen atoms are omitted. Figure 1 is shown as reference.

For the tangential mode, the aromatic plane was oriented along the membrane surface, while the heteroaliphatic moieties were oriented towards the membrane center. Additional details on the starting structures can be inferred from table 3. The orientation of C4-PDI-C4 additionally influences the space uptake along the membrane surface, and thus effects the number of lipid molecules placed inside the box. In general, the tangential insertion mode necessitates 93 DOPG molecules, while one more DOPG molecule is present when the emitter is placed perpendicularly. An exception is the tangential insertion where C4-PDI-C4 is far from the membrane center, as here the membrane penetration is reduced, thus enabling one additional DOPG lipid. Nevertheless, this difference in lipid numbers is diminishing and thus can be neglected. Furthermore, the number of DPPC molecules in the upper lipid layer is not influenced by the insertion of C4-PDI-C4, as the chromophore only penetrates the lower leaflet.

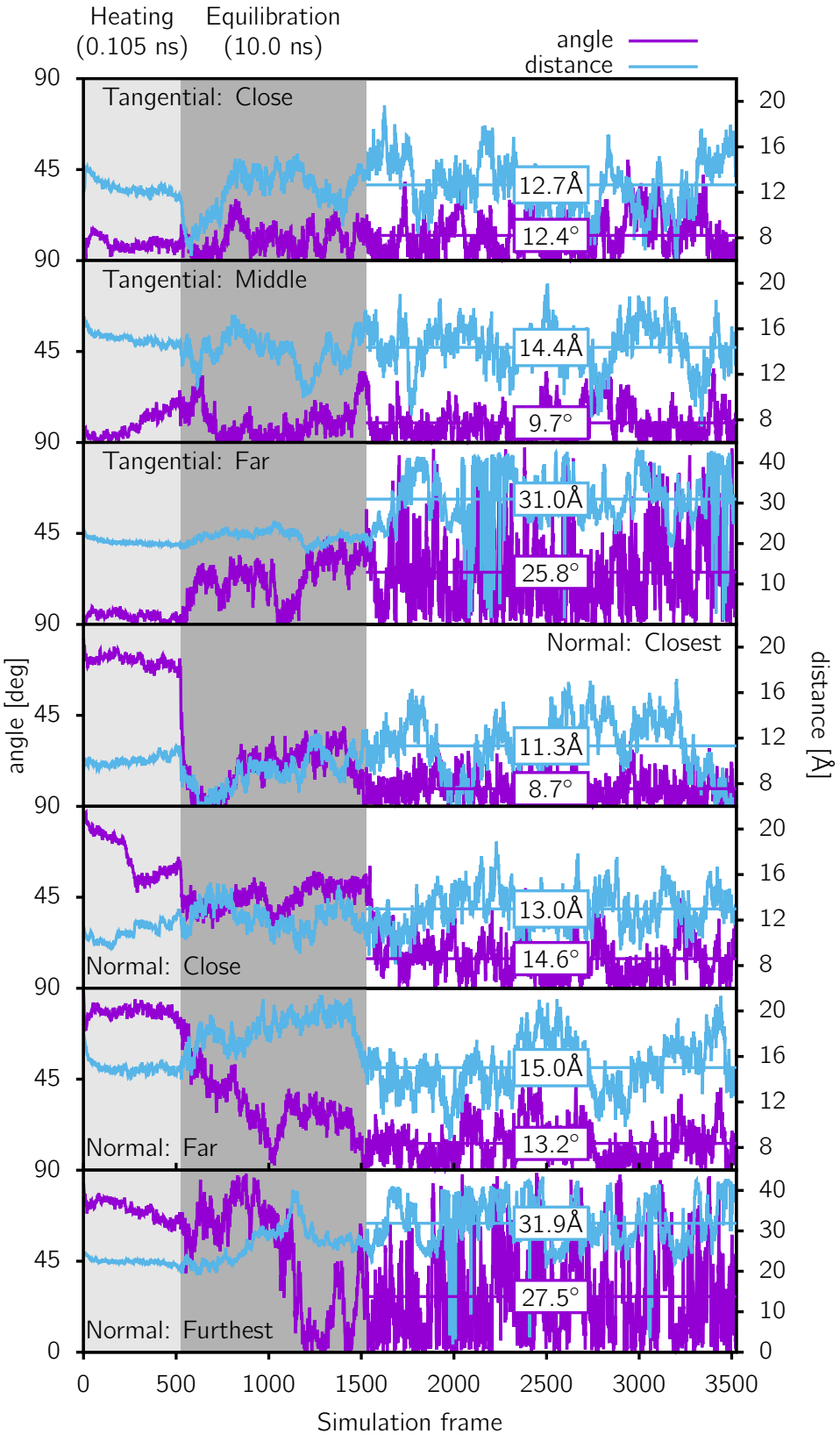

Figure 29: Distance between C4-PDI-C4 and the center of the membrane as well as the angle of the TDM to the surface of the membrane for the seven different insertion modes. During production, each frame corresponds to a time step of 0.1 ns, such that 200 ns production time are presented here. Averages for the distance and angle over these production times are displayed as horizontal lines.

The chromophore-membrane center distance as well as the angles of the TDM of C4-PDI-C4 with respect to the surface of the membrane for these seven trajectories are presented in figure 29. In five of these trajectories, C4-PDI-C4 remains bound into the membrane with stable distances to the membrane center between 8 and 18 Å. For the simulations where the chromophore was inserted furthest distant from the membrane center, both for the tangential and perpendicular insertion modes, C4-PDI-C4 leaves the membrane and remains in solution for the entire simulation time, as indicated by larger distances of around 31-32 Å. This signifies that the chromophore was initially placed at too large a distant to connect constructively to the membrane. However, there are some artifacts in the trajectories, showing up as sudden drops in the distance to almost zero. This is caused by the chromophore approaching the upper membrane leaflet, which can be reached through the solvation phase due to the periodic boundary conditions imposed. As a result, lipid molecules leave the periodic box on the one side and re-entering on the opposite, thus causing a massive shift of the center of mass. Therefore, these averaged distances can only be interpreted as a lower bound to the true mean distance. Similarly, while the proper values are given for the angle, this data is not physically sound, as the chromophore in solution interacting with both membrane leaflets does not represent the situation in situ. Thus, to obtain valid information on C4-PDI-C4 in solution or in close proximity to the membrane surface, additional simulations with increased solvent layer are required, which is not in the scope of this work.

On the other hand, the simulations in which C4-PDI-C4 remained inserted into the membrane, *i.e.*, distances of below 20 Å, unite at similar distances. This convergence is regardless of the number of DOPG (93 or 94) lipid molecules in the box, confirming that this slight initial differences are negligible. This indicates a distinct local minimum for C4-PDI-C4 in the membrane, into which the chromophore evolves indepentently from the starting orientation. One slight exception to this joint convergence is the closest insertion in the perpendicular orientation, which displays the shortest of all distances, at times dropping below 6 Å. This indicates a second local minimum closer to the center of the membrane. To allude the stability of this second local maximum, the trajectory was propagated another 200 ns. This second production period yielded an average distance of 11.2 Å, which is effectively identical to that of the first 200 ns. This insertion mode not converging into the same local minimum as the others stresses the possibility of the existence of a second local minimum.

Nevertheless, the five trajectories in which C4-PDI-C4 remained bonded to the membrane behave very similarly regardless of the insertion mode and initial distance. For all five simulations, the aromatic plane of C4-PDI-C4 aligns parallel to the membrane surface close to the hydrophobic phase of the lipid bilayer, with the positively charged groups at the end of the heteroaliphatic tail pointing outwards to the lipids polar head groups and the solvent layer. One representative snapshot for this conformation is

Name	Displacement / Å	#DPPC	#DOPG
Tangential: Close	9	102	93
Tangential: Middle	13	102	93
Tangential: Far	21	102	94
Perpendicular: Closest	8	102	94
Perpendicular: Close	11	102	94
Perpendicular: Far	18	102	94
Perpendicular: Furthest	25	102	94

Table 3: Attributes for the different simulations performed with C4-PDI-C4.

shown in figure 30. There is some flexibility in the orientation of the aromatic plane, which can flip upright, rotating around the N-N axis. In this way, the nitrogen atoms, which are the reference atoms for the TDM, remain equally distant from the center of the membrane. This is also represented in the angle displayed in figure 29, which is mostly below 15° and very rarely exceeds 30° in any of the five simulations.

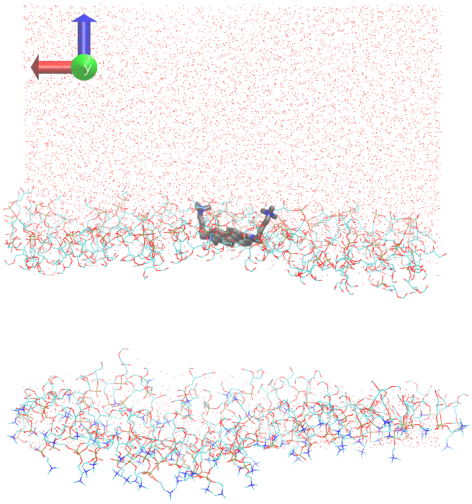

Figure 30: Snapshot of the MD simulation for C4-PDI-C4 (perpendicular, far insertion, frame 3000). Atoms and bonds are colored by element: cyan and grey for carbon in lipids and ligand, respectively, blue for nitrogen and red for oxygen. Axes are displayed for reference: x (red), y (green) and z (blue). For clarity purposes, only water molecules and lipid head moieties are displayed, while aliphatic lipid tails are not included. Hydrogen atoms are omitted.

This indicates that the tangential insertion mode appears to be the favored for C4-PDI-C4. Even the trajectories starting with the perpendicular orientation quickly evolve into the tangential insertion mode, which is especially notable in the trajectory where C4-PDI-C4 was inserted perpendicularly closest to the center of the membrane. Here, the angle for the TDM drops from above 70° all the way below 5° within the first nanosecond of equilibration time. In total, the average distance of C4-PDI-C4 to the membrane center (when inserted into the membrane) is approx. 13.3 Å at a TDM angle relative to the membrane surface of around 11.7°.

4.2.2 Ruthenium complex

Analogously to the simulations performed with C4-PDI-C4, different insertion distances were probed for $Ru(bpy)_2bpyC9$, as well. Since a high attractive interaction between the aliphatic tails of the lipids and the ligand is to be expected, only one insertion direction was chosen as a starting point, in which one of the tails points straight down towards the center of the membrane. The second aliphatic tail was wrapped along the chromohore's core in the starting geometry. Three different distances to the center of the membrane were investigated (see figure 31).

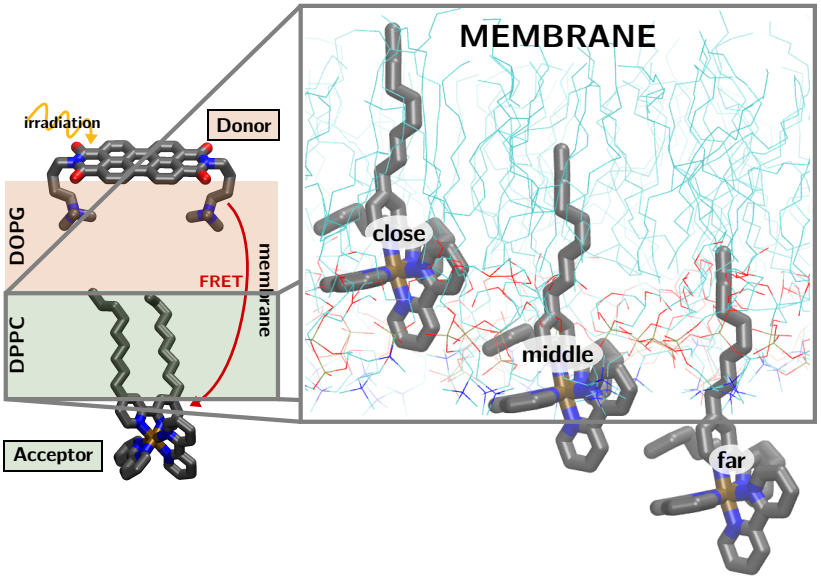

Figure 31: Insertions of $Ru(bpy)_2bpyC9$ into the membrane. Atoms and bonds are colored by element: cyan and grey for carbon in lipids and ligand, respectively, blue for nitrogen, red for oxygen and ochre for ruthenium. For clarity purposes, only lipid head moieties are displayed, while aliphatic lipid tails are not included. Hydrogen atoms are omitted. Figure 1 is shown as reference.

Again, the depth of insertion influences the number of lipid molecules in the respective leaflet, with the close and middle insertions conditioning 99 DPPC molecules each, while the membrane surface penetration of the far insertion mode is diminished, thus allowing two additional DPPC molecules to be put into the simulation box (see table 4).

Name	Displacement / Å	#DPPC	#DOPG
Close	10	99	95
Middle	17	99	95
Far	24	101	95
Far (Modified)	24	99	95

Table 4: Attributes for the different simulations performed with $Ru(bpy)_2bpyC9$.

To overcome this difference, a fourth starting geometry was set up starting from the middle insertion mode, for which the z-coordinates of all $Ru(bpy)_2bpyC9$ atoms were manually increased by 7 Å, to overlap with the far position, while all other molecules in the box remained unchanged with respect to the middle insertion box. As a result, the new starting geometry, now termed "far (modified)", is a mixture of the middle conditions and the chromophore's far position.

The distances and angles to the surface of the membrane for both TDM modes parametrized in section 4.1.2 are presented in figure 32. The close and middle insertion modes converge into very similar conditions, with the distance between chromophore and the center of the membrane stably varying around 18 Å. This local minimum is characterized by both aliphatic tails inserted into the membrane, interacting with the hydrophobic lipids, while the photoactive core is surrounded by the polar head groups of the lipids (see figure 33 left). However, this conformation does not orient the TDM vectors either parallel or perpendicular to the surface of the membrane as hypothesized in section 4.1.3. Rather, the core of $Ru(bpy)_2bpyC9$ tilts such that both vectors are arranged approximately as bisectors. Especially in the middle insertion, the angles are essentially identical when averaged over the 200 ns. Still, there is a lot of flexibility in the orientation of the TDMs, with the values ranging from 0° all the way up to 90°.

In the snapshot presented in figure 33 (left), the membrane is slightly bent. This effect could be caused by a slight overestimation of the membrane penetration of the ruthenium complex, which in turn conditions too few DPPC lipids placed into the upper leaflet initially. As a result, during simulation, the upper leaflet contracts, while the lower does not, as it was assembled without any ligand. The bending could be caused by this difference in expanse similar to the temperature-induced bending of a bimetallic strip. Nevertheless, it is unlikely that this bending significantly affects the position and orientation of $Ru(bpy)_2bpyC9$ within the membrane.

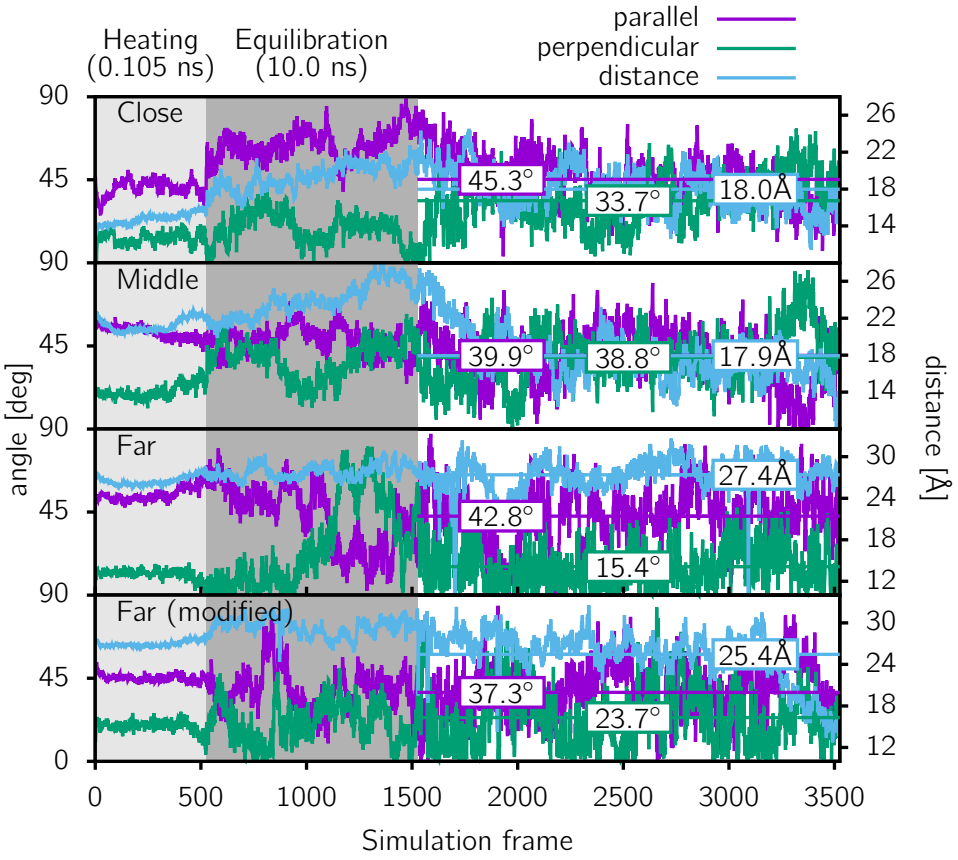

Figure 32: Distance between $Ru(bpy)_2bpyC9$ and the center of the membrane as well as the angles of the two transition dipole moment modes to the surface of the membrane for the four different insertion distances. During production, each frame corresponds to a time step of 0.1 ns, such that 200 ns production time are presented here. Averages for the distance and angle over these production times are displayed as horizontal lines.

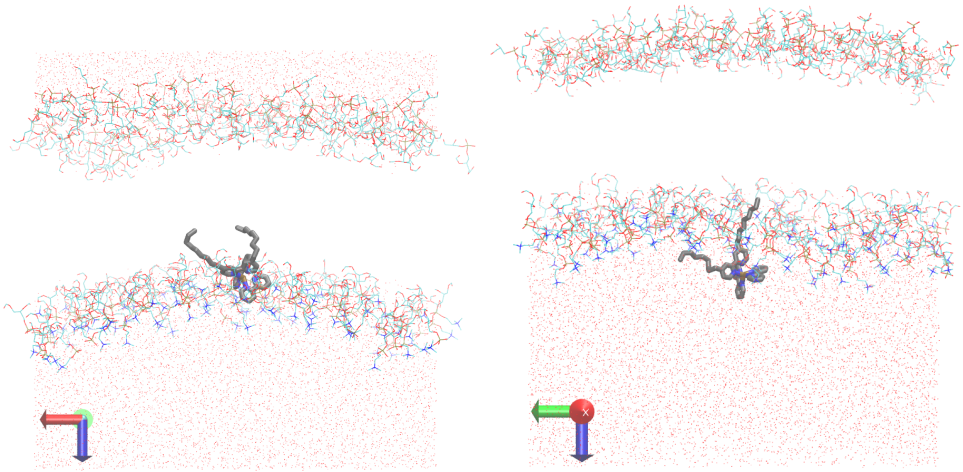

Figure 33: Snapshots of the MD simulation for Ru(bpy)$_2$bpyC9. Left: middle insertion, frame 3000; right: far insertion, frame 2135. Atoms and bonds are colored by element: cyan and grey for carbon in lipids and ligand, respectively, blue for nitrogen, red for oxygen and ochre for ruthenium. Axes are displayed for reference: x (red), y (green) and z (blue). For clarity purposes, only water molecules and lipid head moieties are displayed, while aliphatic lipid tails are not included. Hydrogen atoms are omitted.

The two trajectories, where Ru(bpy)$_2$bpyC9 is initially inserted far from the center of the membrane, suggest a second local minimum at larger distances, in which the complex is still bound to the membrane. Here, only one of the aliphatic tails is inserted into the membrane, with the other one flickering around at the membrane/water interface (see figure 33 right). This leads to the photoactive core of the complex being around 25-27 Å distant from the center of the membrane. This fixation of one aliphatic tail above and one below the lipids head groups also causes a distinction in behavior of the TDM angles, with the TDM parallel to the C2 symmetry axis of the complex somewhat aligning with the membrane surface. Comparing figure 33 left and right, it is noticable how different the box dimensions, especially in z-direction, are. This is most probably caused by the membrane surface penetration of the ruthenium, which increases the area requirement of the membrane upon insertion and thus extends the box in the xy-plane. In turn, this causes a contraction in the z-dimension. Furthermore, in the far insertion trajectories, there are again visible some artefacts in the distance caused by lipid molecules re-entering the periodic box on the opposite face. However, since they only appear very shortly before vanishing again, they can be neglected.

To evaluate the stability of this more distant local minimum and the crossing possibility between the two, the middle and the far trajectories were propagated for additional 200 ns. The two regimes of both minima are very well visible when plotting the distances of all trajectories (see figure 34). And indeed, the modified far trajectory crosses between the two local minima, a process which already begun during the first 200 ns, and remains in the closer minimum for the rest of the propagation time. Thus, there is an apparent crossing possibility from the far minimum to the close minimum. Contrarily, the middle and far trajectories remain in their respective local minima for the entire 400 ns. Whether the hinted stability of the local minimum of the far trajectory is an artefact of the increased density in the upper membrane leaflet due to the higher number of lipid molecules, can not be answered unambiguously. However, the modified far trajectory progressing in this minimum for well over 150 ns production time is a strong indicator for the physical relevance of this local minimum. As a result, it is to be expected that parts of a Ru(bpy)$_2$bpyC9 ensemble will aggregate in the far

minimum, with other parts populating the close minimum. To properly evaluate the relative stability of each of the local minima, more sophisticated binding energy analysis tools have to be employed, which exceeds the scope of this work. Here, this ensemble distribution is approximated by averaging over all computed trajectories. In total, this yields an average distance of the photoactive core to the membrane center of 20.9 Å, and angles of 41.6° and 29.6° for the parallel and perpendicular modes, respectively.

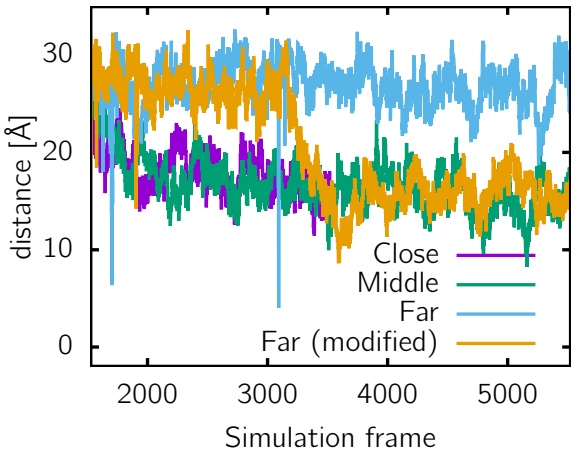

Figure 34: Distance between Ru(bpy)$_2$bpyC9 and the center of the membrane for the four different insertion distances. During production, each frame corresponds to a time step of 0.1 ns, such that 400 ns production time are presented here except for the close insertion mode, which was not propagated beyond 200 ns.

4.3 FRET rate evaluation

The results gathered by means of excited state calculations and molecular dynamic simulations in the preceding chapters allow to compute the rate constant of the energy transfer according to the FRET rate equation (equation 1). In this, the distance between the chromophores is, assuming the chromophores are directly opposite in the respective membrane leaflets, equal to the sums of individual distances to the center of the membrane, and the TDM magnitudes as well as the spectral overlap have been presented in section 4.1. The orientation factor κ^2 is computed from the angles between the TDMs with each other and with the distance vector $\vec{r}_{AD}$ (see figure 2). These angles can be obtained directly, since the averaged angles of the TDMs with respect to the surface of the membrane are known. The angle of the C4-PDI-C4 TDM with respect to the surface of the membrane of 11.7° corresponds to $\theta_D = 78.3°$. For the parallel (41.6°) and perpendicular (29.6°) modes in Ru(bpy)$_2$bpyC9, $\theta_A = 48.4°$ and 60.4°, respectively (see figure 35). Again, this assumes that both chromophores are directly opposite each other, such that the distance vector $\vec{r}_{AD}$ is the normal vector to both surfaces of the lipid bilayer.

However, assessing θ_{AD} is more complex. The results and angles presented for the simulations of C4-PDI-C4 and Ru(bpy)$_2$bpyC9 up until now were referenced against the surface of the membrane, which coincides with the xy-plane. As a result, the z-component of the TDM is strictly defined, while the rotation within the xy-plane is not restricted to one orientation within the membrane. The representation in figure 35 assumes that both TDMs coincide with the paper plane, say the xz-plane. But already within this two-dimensional picture, there exist two different values for θ_{AD}, as

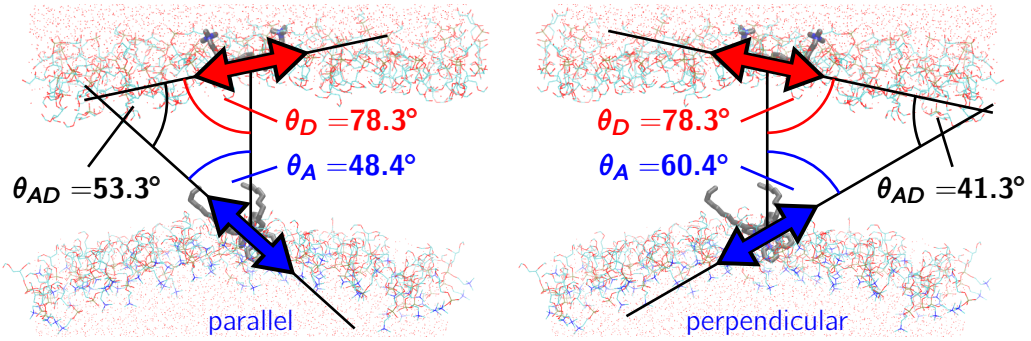

Figure 35: Representation of the light-harvesting system with C4-PDI-C4 and Ru(bpy)$_2$bpyC9 embedded into opposite leaflets of the lipid bilayer membrane. Angles θ_D, θ_A, and θ_{AD} are indicated. For the latter, the less acute angle of the two possible arrangements within the paper plane is chosen.

one of the chromophores can be flipped horizontally. The three-dimensional picture is much more complicated, as rotation within the xy-plane is now permitted, resulting in a continuous spectrum of values for θ_{AD}. This distribution has to be accounted for when computing the FRET efficiency.

For simplicity's sake, the xz-plane is defined such that in contains the donors TDM $\vec{\mu}_D$. In consequence, the normalized donor TDM comprises of x_D and z_D, the ratio of which being defined by the angle with respect to the surface of the membrane, while $y_D = 0$. For the normalized acceptor TDM $\vec{\mu}_D$, x_A and z_A are defined in a similar way, but it has to be accounted for rotation within the surface plane around an angle φ. With this, the dot product between the donor and acceptor TDMs can be represented as

$$|\vec{\mu}_D \cdot \vec{\mu}_A| = \left| \begin{pmatrix} x_D \\ 0 \\ z_D \end{pmatrix} \cdot \begin{pmatrix} x_A * \cos(\varphi) \\ x_A * \sin(\varphi) \\ z_A \end{pmatrix} \right| = |x_D x_A \cos(\varphi) + z_D z_A|. \quad (43)$$

Since the angle between the TDMs is defined to always be positive, the absolute value of the dot product is considered. This dot product flips its sign at $x_D x_A \cos(\varphi) = z_D z_A$ or at the angle $a = \arccos(-\frac{z_D z_A}{x_D x_A})$, respectively. In consequence, when averaging over all unambiguous values for φ, *i.e.*, from 0 to π, the integration has to be split in two parts, accounting for the different signs:

$$\overline{|\vec{\mu}_D \cdot \vec{\mu}_A|} = \frac{1}{\pi}\left[\int_0^a (x_D x_A \cos(\varphi) + z_D z_A)d\varphi - \int_a^\pi (x_D x_A \cos(\varphi) + z_D z_A)d\varphi\right]. \quad (44)$$

Integration and rearranging then yields the following equation to compute the averaged dot product between the TDMs of donor and acceptor:

$$\overline{|\vec{\mu}_D \cdot \vec{\mu}_A|} = \frac{1}{\pi}\left[(2x_D x_A + z_D z_A)\sin(a) + a z_D z_A - \pi z_D z_A\right]. \quad (45)$$

Since the TDMs here as defines as normalized, it holds $\overline{|\vec{\mu}_D \cdot \vec{\mu}_A|} = \overline{\cos\theta_{AD}}$. From here, and with the values for θ_D and θ_A as presented above, the orientation factor κ^2 can be evaluated directly from equation 3: $\kappa^2 = [\cos(\theta_{AD}) - 3\cos(\theta_D)\cos(\theta_A)]^2$. For instance, for two TDMs perfectly aligned with the membrane surface, *i.e*, parrallel to one another and both perpendicular to the distance vector $\vec{r}_{AD}$, corresponds to $\kappa^2 \approx 0.41$.

Acoordingly, averaging the alignments between the C4-PDI-C4 donor and the Ru(bpy)$_2$bpyC9 acceptor chromophores, yields $\kappa^2 = 0.00167$ and 0.0511 for the parallel and perpendicular transition modes of Ru(bpy)$_2$bpyC9, respectively. These values are two or one orders of magnitude below the average value in isotropic media of 2/3, indicating that the membrane confines the orientations of this particular chromophore pair in a FRET rate-diminishing fashion.

On the other hand, with distances to the center of the membrane of 13.3 Å and 20.9 Å for C4-PDI-C4 and Ru(bpy)$_2$bpyC9, respectively, the minimum distance between the chromophores, that is achieved once the chromophores are directly opposite in the membrane, amounts to 34.2 Å. Efficient energy transfer can in general be attained at distances below 60 Å[77], such that, judged by distance, the membrane confinement appears to facilitate the energy transfer.

With this, the parameters κ^2, r, $|\vec{\mu}_D|$, $|\vec{\mu}_A|$ and the spectral overlap are defined for the emission of C4-PDI-C4 and four absorptive transitions in Ru(bpy)$_2$bpyC9. Additionally to these, the FRET rate is computed from fundamental physical constants such as Planck's constant, the speed of light and the vacuum permittivity, as well as the refractive index, which was measured to be 1.478 in DPPC monolayers[78]. This enables the computation of the FRET rate constant k_{FRET} and the lifetime associated with the FRET τ_{FRET}, which is the inverse of the rate constane. The photophysical magnitudes as well as the final rate constants and lifetimes are presented in table 5.

Donor	Acceptor	κ^2	$\|\vec{\mu}_D\|$ [a.u]	$\|\vec{\mu}_A\|$ [a.u]	r [nm]	Overlap [cm]	k_{FRET} [s^{-1}]	τ_{FRET} [ns]
$S_1 \rightarrow S_0$	$S_0 \rightarrow S_5$	0.00167	23.6	0.224	3.42	2.12E-4	1.62E+6	617
$S_1 \rightarrow S_0$	$S_0 \rightarrow S_6$	0.0511	23.6	0.968	3.42	1.44E-4	6.28E+8	1.59
$S_1 \rightarrow S_0$	$S_0 \rightarrow S_7$	0.0511	23.6	1.62	3.42	8.00E-5	9.77E+8	1.02
$S_1 \rightarrow S_0$	$S_0 \rightarrow S_8$	0.0511	23.6	1.62	3.42	8.00E-5	3.19E+7	31.3

Table 5: Photophysical properties of the C4-PDI-C4/Ru(bpy)$_2$bpyC9 pair embedded into the membrane for the four possible energy transfers.

Again, it has to be stressed that these absolute values are only restrictively expressive. As already explained in section 4.1.3, they heavily depend on the way the spectra are convoluted and shifted, and thus how the overlap is computed. Additionally, the values presented in table 5 have to be considered as an upper bound regarding the distance between the chromophores. Any arrangement, in which donor and acceptor are not directly opposite in the membrane, but displaced laterally, would not only decrease the rate as a direct consequence of the increased distance, but also indirectly, as κ^2 will decrease due to variation in the angles between the TDMs and the distance vector.

As such, the absolute rate constants k_{FRET} only resemble a cautious approach to the true rates, and allow a general assessment of the efficiency. However, they enable the relative comparison of the individual modes of the transition. As such it is obvious, that populating Ru(bpy)$_2$bpyC9's S_6 and S_7 contributes most to the total energy transfer, with the population of S_8 and S_5 being one and two orders of magnitude less important, respectively. This demonstrates that the better alignment of the TDM perpendicular to the C2 symmetry axis of the ruthenium complex with the TDM of C4-PDI-C4, paired with the strong dipole strengths, makes up for the diminished spectral overlap. The $S_0 \rightarrow S_8$ transition, on the other hand, is identical to the $S_0 \rightarrow S_7$ transition in dipole strength and overlap, as they have been treated as degenerated states this analysis, but contributes over a magnitude less to the transfer rate due to the unfavorable arrangement. The population of S_5 is diminishingly small compared to the other transitions due to both an unfavored arrangement and a small

transition dipole strength.

Additionally to this descriptive assessment, the analysis of the different factors of the rate equation enables for the proposition of optimization strategies. Excluding trivial parameters such as the TDM dipole strength, where an increase in strength naturally positively influences the energy transfer rate, key parameters of the rate equation are donor-acceptor distance, the spectral overlap and the orientation factor κ^2. The causality for both the distance and the spectral overlap is pretty straight-forward. Smaller distances and larger overlaps result in a more efficient transfer. However, optimization of both these terms is more complicated than this simple description, as other criteria have to be considered. The distance, for instance, is restricted by the conceptual approach of spatially separating donor and acceptor, potentially enabling the tuning of external effects such as the solvent or the pH in a potential application of this light-harvesting system. As such, the membrane thickness resembles a lower boundary to the inter-chromophoric distance within this design approach. Similarly, the accessibility of an increased spectral window is desirable for light harvesting units, which can be achieved by sufficiently different absorption profiles. In turn, some deviation of the donor's emission and the acceptor's absorption profile will have to be tolerated, as the manipulation of the Stoke's shift is not easily feasible. Therefore, there will virtually always be a compromise between maximizing the spectral window and ensuring sufficient overlap.

This leaves the orientation factor κ^2 for the optimization of the FRET rate constant. Surely, with even the more favorable orientation factor being almost two orders of magnitude smaller than the largest possible κ^2 of 4 for aligned TDMs, this leaves much to be desired. As became clear when investigating lipid bilayer systems, any TDMs aligned tangential to the surface of the membrane are suboptimal to the transfer due to the rotation within the plane. This causes even donor and acceptor TDMs, which both are flush within the surface of the membrane, to arrange perpendicularly to one another from time to time. The desired orientation of all TDMs would therefore be normal to the membrane surface. With this, the TDMs of FRET donor and acceptor will be aligned and less sensitive to rotation around the surface's normal vector. Design strategies which alter the chromophore's substituents in a way that these normal orientations are enforced and stabilized therefore promise significant rate increases.

Aside from the optimization of the energy transfer itself, however, the results presented here also enable to manipulate the electronic configuration of the photosensitzer immediately after energy transfer. For instance, the excitations to the S_7 or S_8 in $Ru(bpy)_2bpyC9$ increase the electron density on different ligands. Even if this different population is not significantly expressed in this complex, it is hinted that excitation to S_7 increases electron density on the modified ligand, while excitation to S_8 mediates electron shifts towards the unmodified ligands. Manipulating the orientation of the chromophores can enforce energy transfer between specific states while repressing interaction between others. Especially within the framework of the photosensitizer embedded into the membrane, as the modified ligand is oriented towards the center of the membrane, while the unmodified bipyridine subunits are exposed to the solvent, selective energy transfer could mediate a polarization of the membrane surface. Thus, synthetic strategies influencing the arrangement can also affect the electron distribution in the acceptor, including all the consequences with regard to geometry, stability and reactivity.

5 Conclusions and outlook

In this work, a holistic computational approach to the rate evaluation of the Förster Resonance Energy Transfer (FRET) between chromophores in complex media, where the position and orientation of the structures is restricted, was presented. This workflow is compelling since it directly assesses all quantities influencing the FRET rate with computational methods, while at the same time minimizes conceptual simplifications within the framework of FRET. For instance, the orientation factor κ^2, which is often neglected and averaged assuming isotropic media, was rigorously evaluated.

The coherent computational methodology is based on a multiscale approach, which ensures accommodating accuracy where this is crucially required, but facilitates reducing computational cost otherwise, enabling the treatment of extensive, bio-inspired systems. Accordingly, the photophysical properties of the chromophores were computed using quantum mechanical (QM) methods, such as density functional theory (DFT) as well as semiempirical tight-binding methods. In contrast, the position and orientation of the chromophores within the medium was evaluated in time using classical molecular dynamics (MD) simulations. Referencing photophysical properties such as transition dipole moments (TDMs) to structural parameters allows to intertwine both QM and MD methods to monitor the temporal evolution of relative TDM orientations within the environment. Rigorous conformational sampling additionally ensures a complete structural analysis.

This workflow was applied to the artificial light-harvesting system comprising the C4-PDI-C4 energy donor and the photosensitizer $Ru(bpy)_2bpyC9$ as energy acceptor embedded into opposite leaflets of a lipid bilayer. While for the donor only the transition from the first electronic excited state to the ground state is of importance, four transitions with sufficient spectral overlap and oscillator strength were identified in the acceptor $Ru(bpy)_2bpyC9$. These four transitions correspond to two sets of TDMs, which are oriented either parallel or perpendicular to the principal C_2 symmetry axis of the Ruthenium complex.

However, the chromophores align within the lipid bilayer in a way which limits the FRET efficiency, as especially the C4-PDI-C4 donor orientates such that the TDM vector almost coincides with the surface of the membrane. Since the membrane itself restricts the deviation of this vector relative to its surface, but not any rotations within the surface plane, this coinciding arrangement goes hand in hand with a decrease in energy transfer rate. Additionally, the orientation of $Ru(bpy)_2bpyC9$ within the lipid bilayer is not beneficial to the energy transfer efficiency, as none of the parallel or the perpendicular TDM modes align favorably with the TDM of C4-PDI-C4. As such, the energy transfer lifetimes vary between ca. 1-600 ns for the different excitations in $Ru(bpy)_2bpyC9$.

These transfer rates and lifetimes leave room for improvement in terms of the efficiency of FRET. However, the analysis in this work hints to promising optimization routes. For instance, enforcing TDM arrangements normal to the surface of the membrane through manipulation of the interaction between embedded structure and membrane lipids would not only minimize rate penalties induced by rotation within the membrane plane, but also enforce optimal alignment of the donor and acceptor TDMs with one another. Since the orientation factors calculated in this work range from 0.00167 to 0.0511, which is way off the ideal value of 4, optimizing the chromophore alignments alone holds promise to increase the FRET rate by a factor of about 100. Furthermore, by manipulating the chromophore orientation within the membrane, selectivity could be enforced by increasing transfer efficiency between selected states while repressing others. Due to different excited state electron densities, two distinct elec-

tronic states in the acceptor with sufficiently separate TDM orientations can enable to manipulate the electronic structure of the photosensitizer after the transfer. Tuning the FRET therefore can be employed to influence the electrostatic properties of the membrane.

A limitation of the presented computational approach is the incapability of DFT to accurately predict excitation energies. Since this massively influences the spectral overlap, the meaningfulness of the total rate constants is significantly restricted. To still obtain reliable results, the computed spectra were readjusted based on experimentally recorded data. The combination of experiment and theory improves the quality of the computed attributes, and the theoretical results augment the experimentally accessible spectral overlap by providing additional information on the contribution of each individual transition. By comparing the overlaps and TDM arrangements between the different individual transfers, invaluable insights can be obtained, allowing for a better understanding of the underlying processes and its potential applications.

In prospect, the data acquired here can be further refined. In this work, the QM calculations used to evaluate the photophysical properties were performed in implicit solvation, but not within the membrane, where the chromophores would actually be. To evaluate how changes in the properties caused by the embedding into the lipid bilayer would affect the attributes significant to the FRET rate, further calculations need to be performed. These could for instance include quantum mechanics / molecular mechanics hybrid calculations, where both chromophores and the membrane are included in the same system. The chromophores are then treated using DFT, while the environment is represented as classical point charges. Based on the results presented here and the future calculations proposed, the light-harvesting unit investigated in this work can then be included in a system where the collected energy is utilized, for instance in combination with a water oxidation catalyst.

References

[1] N. Nelson, C. F. Yocum, *Annu. Rev. Plant Biol.* **2006**, *57*, 521–565.

[2] A. Pannwitz, D. M. Klein, S. Rodrıguez-Jiménez, C. Casadevall, H. Song, E. Reisner, L. Hammarström, S. Bonnet, *Chem. Soc. Rev.* **2021**, *50*, 4833–4855.

[3] N. Sinambela, J. Bösking, A. Abbas, A. Pannwitz, *ChemBioChem* **2021**, *22*, 3140–3147.

[4] S. Vasil'ev, D. Bruce, *Plant Cell* **2004**, *16*, 3059–3068.

[5] A. Pannwitz, H. Saaring, N. Beztsinna, X. Li, M. A. Siegler, S. Bonnet, *Chem. Eur. J.* **2020**, *27*, 3013–3018.

[6] N. Ikuta, S.-y. Takizawa, S. Murata, *Photochem. Photobiol. Sci.* **2014**, *13*, 691–702.

[7] M. Hansen, F. Li, L. Sun, B. König, *Chem. Sci.* **2014**, *5*, 2683–2687.

[8] M. Hansen, S. Troppmann, B. König, *Chem. Eur. J.* **2015**, *22*, 58–72.

[9] B. Limburg, J. Wermink, S. S. van Nielen, R. Kortlever, M. T. M. Koper, E. Bouwman, S. Bonnet, *ACS Catal.* **2016**, *6*, 5968–5977.

[10] M. Anzola, C. Sissa, A. Painelli, A. A. Hassanali, L. Grisanti, *J. Chem. Theory Comput.* **2020**, *16*, 7281–7288.

[11] J. de Torres, M. Mivelle, S. B. Moparthi, H. Rigneault, N. F. V. Hulst, M. F. García-Parajó, E. Margeat, J. Wenger, *Nano Lett.* **2016**, *16*, 6222–6230.

[12] A. Iqbal, S. Arslan, B. Okumus, T. J. Wilson, G. Giraud, D. G. Norman, T. Ha, D. M. J. Lilley, *Proc. Natl. Acad. Sci. U.S.A.* **2008**, *105*, 11176–11181.

[13] R. Roy, S. Hohng, T. Ha, *Nat. Methods* **2008**, *5*, 507–516.

[14] I. Reinartz, C. Sinner, D. Nettels, B. Stucki-Buchli, F. Stockmar, P. T. Panek, C. R. Jacob, G. U. Nienhaus, B. Schuler, A. Schug, *J. Chem. Phys.* **2018**, *148*, 123321.

[15] M. J. Shoura, R. U. Ranatunga, S. A. Harris, S. O. Nielsen, S. D. Levene, *Biophys. J.* **2014**, *107*, 700–710.

[16] S. Calero, S. Lago, B. Garzón, *Mol. Simul.* **2003**, *29*, 519–525.

[17] R. A. Urzúa-Leiva, S. Rampino, R. Arratia-Perez, E. Mosconi, M. Pastore, F. D. Angelis, *J. Phys. Chem. C* **2015**, *119*, 16490–16499.

[18] A. Pannwitz, "Unpublished work."

[19] P. Pracht, F. Bohle, S. Grimme, *Phys. Chem. Chem. Phys.* **2020**, *22*, 7169–7192.

[20] T. Förster, *Die Naturwissenschaften* **1946**, *33*, 166–175.

[21] J. Perrin, *Gauthier-Villars Paris* **1925**, 322.

[22] J. Perrin, *CR Acad. Sci. Paris* **1927**, *184*, 1097–1100.

[23] F. Perrin, *Ann. Phys.* **1932**, *10*, 283–314.

[24] T. Förster, *Ann. Phys. (Berlin)* **1948**, *437*, 55–75.

[25] E. Haas, E. Katchalski-Katzir, I. Z. Steinberg, *Biochemistry* **1978**, *17*, 5064–5070.

[26] W. Koch, M. C. Holthausen, *A Chemist's Guide to Density Functional Theory*, Wiley, **2001**.

[27] M. Born, R. Oppenheimer, *Ann. Phys.* **1927**, *389*, 457–484.

[28] P. Hohenberg, W. Kohn, *Phys. Rev.* **1964**, *136*, B864–B871.

[29] W. Kohn, L. J. Sham, *Phys. Rev.* **1965**, *140*, A1133–A1138.

[30] C. C. J. Roothaan, *Rev. Mod. Phys.* **1951**, *23*, 69–89.

[31] D. R. Hartree, *Math. Proc. Camb. Phil. Soc.* **1928**, *24*, 111–132.

[32] V. Fock, *Z. Physik* **1930**, *61*, 126–148.

[33] M. Marques, A. Rubio, E. K. Gross, K. Burke, F. Nogueira, C. A. Ullrich, *Time-dependent density functional theory*, *Vol. 706*, Springer Science & Business Media, **2006**.

[34] F. Jensen, *Introduction to Computational Chemistry*, John Wiley & Sons, Inc., Hoboken, NJ, USA, **2006**.

[35] A. D. Becke, *Phys. Rev. A* **1988**, *38*, 3098–3100.

[36] J. P. Perdew, *Phys. Rev. B* **1986**, *33*, 8822–8824.

[37] C. Lee, W. Yang, R. G. Parr, *Phys. Rev. B* **1988**, *37*, 785–789.

[38] A. D. Becke, *J. Chem. Phys.* **1993**, *98*, 5648–5652.

[39] B. Miehlich, A. Savin, H. Stoll, H. Preuss, *Chem. Phys. Lett.* **1989**, *157*, 200–206.

[40] L. González, R. Lindh, *Quantum Chemistry and Dynamics of Excited States: Methods and Applications*, John Wiley & Sons, **2020**.

[41] E. Runge, E. K. U. Gross, *Phys. Rev. Lett.* **1984**, *52*, 997–1000.

[42] R. van Leeuwen, *Phys. Rev. Lett.* **1998**, *80*, 1280–1283.

[43] G. Vignale, *Phys. Rev. A* **2008**, *77*, 062511-1–062511-9.

[44] J. Theilhaber, *Phys. Rev. B* **1992**, *46*, 12990–13003.

[45] K. Yabana, G. F. Bertsch, *Phys. Rev. B* **1996**, *54*, 4484–4487.

[46] V. Barone, J. Bloino, M. Biczysko, F. Santoro, *J. Chem. Theory Comput.* **2009**, *5*, 540–554.

[47] J. Grunenberg, *Computational Spectroscopy*, Wiley-VCH Verlag GmbH & Co. KGaA, **2010**.

[48] M. J. Frisch, G. W. Trucks, H. B. Schlegel, G. E. Scuseria, M. A. Robb, J. R. Cheeseman, G. Scalmani, V. Barone, G. A. Petersson, H. Nakatsuji, X. Li, M. Caricato, A. V. Marenich, J. Bloino, B. G. Janesko, R. Gomperts, B. Mennucci, H. P. Hratchian, J. V. Ortiz, A. F. Izmaylov, J. L. Sonnenberg, D. Williams-Young, F. Ding, F. Lipparini, F. Egidi, J. Goings, B. Peng, A. Petrone, T. Henderson, D. Ranasinghe, V. G. Zakrzewski, J. Gao, N. Rega, G. Zheng, W. Liang, M. Hada, M. Ehara, K. Toyota, R. Fukuda, J. Hasegawa, M. Ishida, T. Nakajima, Y. Honda, O. Kitao, H. Nakai, T. Vreven, K. Throssell, J. A. Montgomery Jr., J. E. Peralta, F. Ogliaro, M. J. Bearpark, J. J. Heyd, E. N. Brothers, K. N. Kudin, V. N. Staroverov, T. A. Keith, R. Kobayashi, J. Normand, K. Raghavachari, A. P. Rendell, J. C. Burant, S. S. Iyengar, J. Tomasi, M. Cossi, J. M. Millam, M. Klene, C. Adamo, R. Cammi, J. W. Ochterski, R. L. Martin, K. Morokuma, O. Farkas, J. B. Foresman, D. J. Fox, Gaussian16 Revision C.01, **2016**.

[49] A. R. Leach, *Molecular modelling: principles and applications*, 1. publ., Longman, Harlow, **1996**.

[50] F. Weigend, R. Ahlrichs, *Phys. Chem. Chem. Phys.* **2005**, *7*, 3297.

[51] F. Weigend, *Phys. Chem. Chem. Phys.* **2006**, *8*, 1057.

[52] V. Barone, M. Cossi, *J. Phys. Chem. A* **1998**, *102*, 1995–2001.

[53] M. Cossi, N. Rega, G. Scalmani, V. Barone, *J. Comput. Chem.* **2003**, *24*, 669–681.

[54] S. Grimme, J. Antony, S. Ehrlich, H. Krieg, *J. Chem. Phys.* **2010**, *132*, 154104.

[55] S. Grimme, S. Ehrlich, L. Goerigk, *J. Comput. Chem.* **2011**, *32*, 1456–1465.

[56] T. Lu, F. Chen, *J. Comput. Chem.* **2012**, *33*, 580–592.

[57] F. Santoro, A. Lami, R. Improta, J. Bloino, V. Barone, *J. Chem. Phys.* **2008**, *128*, 224311.

[58] J.-P. Ebejer, G. M. Morris, C. M. Deane, *J. Chem. Inf. Model.* **2012**, *52*, 1146–1158.

[59] P. C. D. Hawkins, *J. Chem. Inf. Model.* **2017**, *57*, 1747–1756.

[60] S. Grimme, *J. Chem. Theory Comput.* **2019**, *15*, 2847–2862.

[61] C. Bannwarth, S. Ehlert, S. Grimme, *J. Chem. Theory Comput.* **2019**, *15*, 1652–1671.

[62] S. Grimme, C. Bannwarth, S. Dohm, A. Hansen, J. Pisarek, P. Pracht, J. Seibert, F. Neese, *Angew. Chem. Int. Ed.* **2017**, *56*, 14763–14769.

[63] A. Malik, *Applied Unsupervised Learning with R : : Uncover Hidden Relationships and Patterns with K-Means Clustering, Hierarchical Clustering, and PCA.* Packt Publishing Ltd., Birmingham, **2019**.

[64] F. Neese, F. Wennmohs, U. Becker, C. Riplinger, *J. Chem. Phys.* **2020**, *152*, 224108.

[65] D. Case, H. Aktulga, K. Belfon, I. Ben-Shalom, S. Brozell, D. Cerutti, T. Cheatham, III, V. Cruzeiro, T. Darden, R. Duke, G. Giambasu, M. Gilson, H. Gohlke, A. Goetz, R. Harris, S. Izadi, S. Izmailov, C. Jin, K. Kasavajhala, M. Kaymak, E. King, A. Kovalenko, T. Kurtzman, T. Lee, S. LeGrand, P. Li, C. Lin, J. Liu, T. Luchko, R. Luo, M. Machado, V. Man, M. Manathunga, K. Merz, Y. Miao, O. Mikhailovskii, G. Monard, H. Nguyen, K. O'Hearn, A. Onufriev, F. Pan, S. Pantano, R. Qi, A. Rahnamoun, D. Roe, A. Roitberg, C. Sagui, S. Schott-Verdugo, J. Shen, C. Simmerling, N. Skrynnikov, J. Smith, J. Swails, R. Walker, J. Wang, H. Wei, R. Wolf, X. Wu, Y. Xue, D. York, S. Zhao, P. Kollman, Amber 2021, San Fransisco, **2021**.

[66] P. Brandt, T. Norrby, B. Åkermark, P.-O. Norrby, *Inorg. Chem.* **1998**, *37*, 4120–4127.

[67] S. Jo, T. Kim, V. G. Iyer, W. Im, *J. Comput. Chem.* **2008**, *29*, 1859–1865.

[68] N. Kučerka, M.-P. Nieh, J. Katsaras, *Bba-biomembranes* **2011**, *1808*, 2761–2771.

[69] S. Izadi, R. Anandakrishnan, A. V. Onufriev, *J. Phys. Chem. Lett.* **2014**, *5*, 3863–3871.

[70] R. Salomon-Ferrer, A. W. Götz, D. Poole, S. L. Grand, R. C. Walker, *J. Chem. Theory Comput.* **2013**, *9*, 3878–3888.

[71] A. W. Götz, M. J. Williamson, D. Xu, D. Poole, S. L. Grand, R. C. Walker, *J. Chem. Theory Comput.* **2012**, *8*, 1542–1555.

[72] S. L. Grand, A. W. Götz, R. C. Walker, *Comput. Phys. Commun.* **2013**, *184*, 374–380.

[73] D. R. Roe, T. E. Cheatham, *J. Chem. Theory Comput.* **2013**, *9*, 3084–3095.

[74] W. Humphrey, A. Dalke, K. Schulten, *J. Mol. Graphics* **1996**, *14*, 33–38.

[75] D. Jacquemin, V. Wathelet, E. A. Perpète, C. Adamo, *J. Chem. Theory Comput.* **2009**, *5*, 2420–2435.

[76] Z. Zara, J. Iqbal, K. Ayub, M. Irfan, A. Mahmood, R. A. Khera, B. Eliasson, *J. Mol. Struct.* **2017**, *1149*, 282–298.

[77] R. B. Sekar, A. Periasamy, *J. Cell Biol.* **2003**, *160*, 629–633.

[78] D. F. Kienle, J. V. de Souza, E. B. Watkins, T. L. Kuhl, *Anal. Bioanal. Chem.* **2014**, *406*, 4725–4733.

[79] R. González-Alemán, D. Hernández-Castillo, J. Caballero, L. A. Montero-Cabrera, *J. Chem. Inf. Model.* **2020**, *60*, 467–472.

[80] R. González-Alemán, D. Hernández-Castillo, A. Rodríguez-Serradet, J. Caballero, E. W. Hernández-Rodríguez, L. Montero-Cabrera, *J. Chem. Inf. Model.* **2020**, *60*, DOI 10.1021/acs.jcim.9b00828.

[81] J. G. Brandenburg, C. Bannwarth, A. Hansen, S. Grimme, *J. Chem. Phys.* **2018**, *148*, 064104.

[82] J. P. Perdew, K. Burke, M. Ernzerhof, *Phys. Rev. Lett.* **1996**, *77*, 3865–3868.

[83] J. P. Perdew, K. Burke, M. Ernzerhof, *Phys. Rev. Lett.* **1997**, *78*, 1396–1396.

[84] C. Adamo, V. Barone, *J. Chem. Phys.* **1999**, *110*, 6158–6170.

[85] T. Yanai, D. P. Tew, N. C. Handy, *Chem. Phys. Lett.* **2004**, *393*, 51–57.

A Appendix: Ru(bpy)$_2$bpyC9 Force Field parametrization

As noted in section 3.2, in the force field of Ru(bpy)$_2$bpyC9 used in this work, the three nitrogen-ruthenium-nitrogen trans-angles were incorrectly parametrized by the author as cis-angles, imposing physically wrong forces on the octahedral center. To demonstrate that this does not notably affect the magnitudes used in this work to compute the FRET rate, an additional simulation with the corrected force field was performed. This simulation was performed on the same starting structure as the run denoted as the middle insertion mode in the main part of this work (see section 4.2).

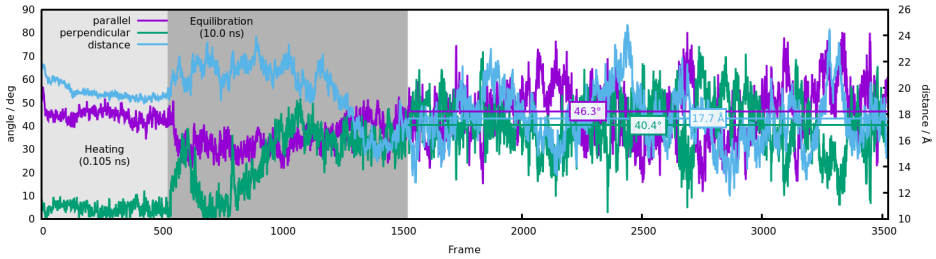

Figure 36: Distance between Ru(bpy)$_2$bpyC9 and the center of the membrane as well as the angles of the two transition dipole moment modes to the surface of the membrane for the simulation with the corrected force field. During production, each frame corresponds to a time step of 0.1 ns, such that 200 ns production time are presented here. Averages for the distance and angle over these production times are displayed as horizontal lines.

Naturally, as MD simulations are not deterministic regarding individual trajectories, this reference simulation exhibits different dynamics compared to the middle insertion simulation in the main part of this work. Nevertheless, the overall properties of the curves appear not different from one another, with the averages in distances being virtually identical (17.7° vs. 17.9°). The angle averages are slightly increased in this reference calculation (46.3° and 40.4° vs. 39.9° and 38.8°), but this deviation is to be expected when considering the large fluctuations the trajectories. These differences can rather be attributed to the short time scales then to differences in the force field. As a result, there is no reason to doubt the validity of the data presented in the main part of this work within the accuracy of the method itself.

B Appendix: Additional molecular orbitals

The molecular orbitals for C1-PDI-C1 in gas phase, Ru(bpy)$_2$bpyC1 in gas phase and Ru(bpy)$_2$bpyC9 in acetonitrile were omitted from the main part of this work and are presented in the following.

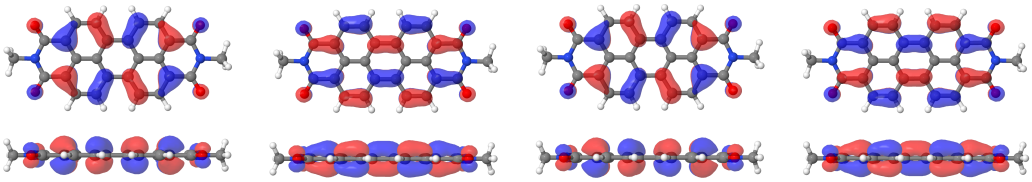

HOMO ground state geometry | **LUMO** ground state geometry | **HOMO** excited state geometry | **LUMO** excited state geometry

Figure 37: Computed HOMOs and LUMOs of C1-PDI-C1 in gas phase. Molecular orbitals are shown at an isosurface cutoff of 0.03 a.u.

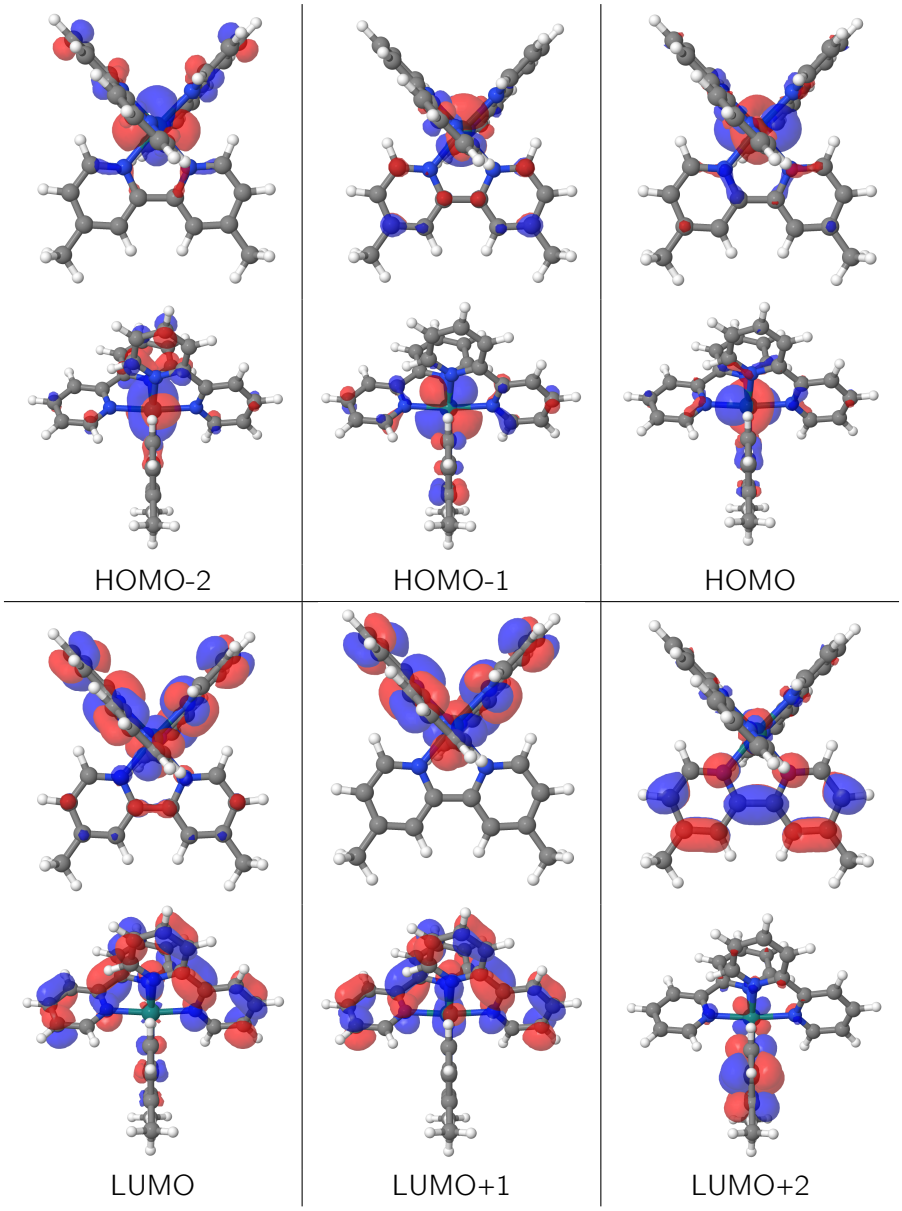

Figure 38: Computed orbitals of $Ru(bpy)_2bpyC1$ in gas phase from HOMO-2 to LUMO+2. Molecular orbitals are shown at an isosurface cutoff of 0.03 a.u.

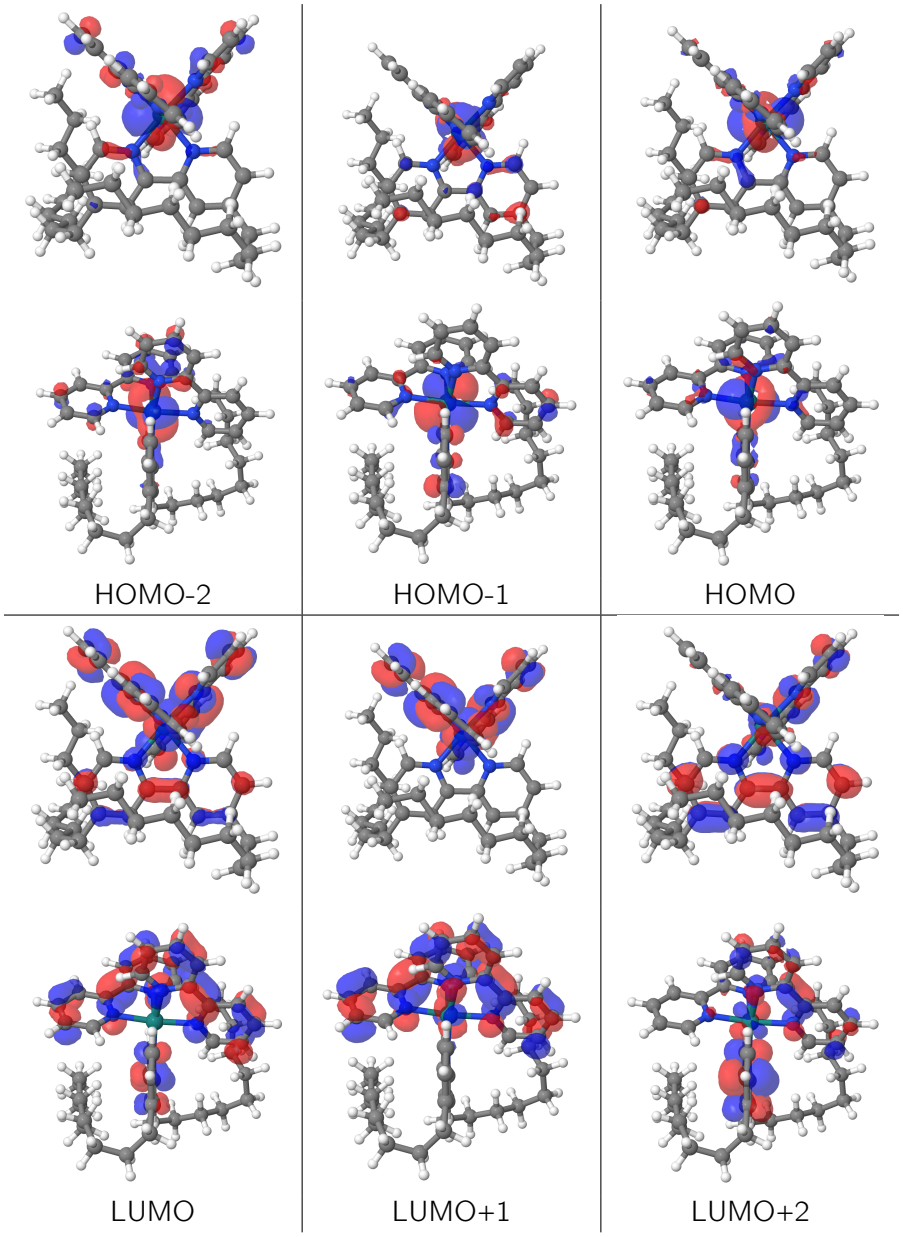

Figure 39: Computed orbitals of $Ru(bpy)_2bpyC9$ in acetonitrile from HOMO-2 to LUMO+2. Molecular orbitals are shown at an isosurface cutoff of 0.03 a.u.

C Appendix: Additional computations

During development of a suitable setup for the generation of the conformational ensemble, additional data was acquired.

For C4-PDI-C4, a CREST run was performed with the same parameters as presented in the main part of this work, but without simulating acetonitrile as implicit solvent, *i.e.*, in gas phase. A first approach to reduce the size of the total ensemble (709 conformers) was to select all conformers within an energy window of 3 kcal/mol with respect to the most stable structure, which yielded 135 conformers. For these structures, B3LYP/def2-SVP energies were computed both on optimized structures as well as the structures obtained directly from the CREST run.

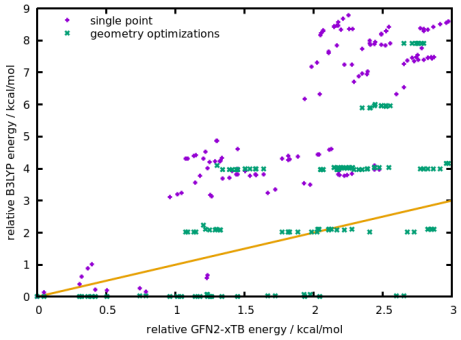

Figure 40: GFN2-xTB vs. B3LYP energies on the 135 conformers of C4-PDI-C4. GFN2-xTB and B3LYP single points were computed on the GFN2-xTB geometries, while for B3LYP additional geometry optimizations were conducted. The yellow line denotes identical GFN2-xTB and B3LYP energies.

For the conformers generated using CREST including acetonitrile as implicit solvent, BP86 single point energies were computed for all 2273 conformers. However, in the main part of this work only the energies of the 1000 conformers remaining after the principal component analysis and k-means clustering were presented to be in line with the conformer generation of $Ru(bpy)_2bpyC9$, where the drastically increased number of conformers prohibited this. As visibile from figure 41, the difference is negligible, *i.e.*, the additional conformers are similar to identical in energies to the 1000 remaining.

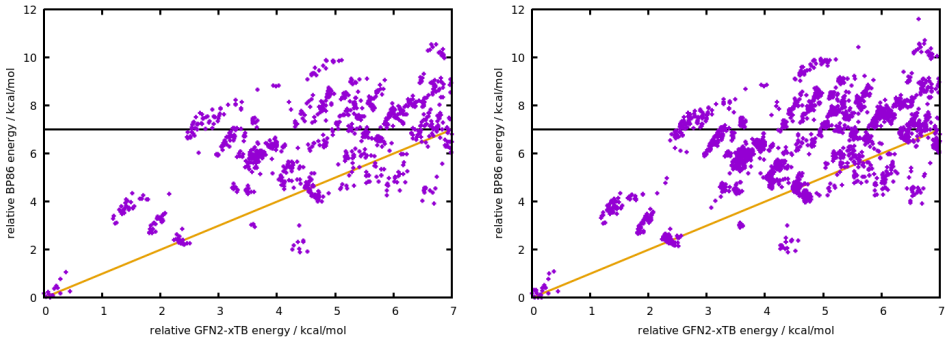

Figure 41: GFN2-xTB vs. BP86 energies on 1000 (left) and all 2273 (right) GFN2-xTB geometries of C4-PDI-C4. The black line denotes 7 kcal/mol in relative BP86 energies, the yellow line identical GFN2-xTB and BP86 energies.

For $Ru(bpy)_2bpyC9$, a CREST run in gas phase yielded 3380 conformers. A first approach to this ensemble was the selection of the conformer within 3 kcal/mol with

respect to the most stable conformer, which yielded a reduced ensemble of 126 conformers. On these, single point and geometry optimization energy calculations were performed on the B3LYP/def2-SVP level of theory.

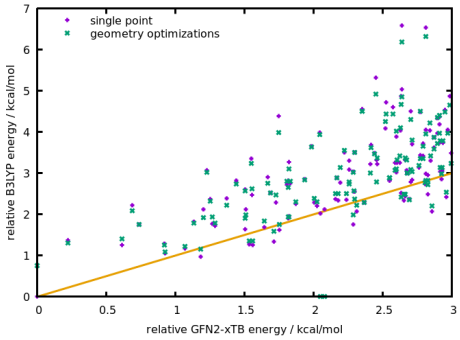

Figure 42: GFN2-xTB vs. B3LYP energies on the 126 lowest conformers of C4-PDI-C4. GFN2-xTB and B3LYP single points were computed on the GFN2-xTB geometries, while for B3LYP additional geometry optimizations were conducted. The yellow line denotes identical GFN2-xTB and B3LYP energies.

A second approach to reducing this gas-phase ensemble without losing higher-lying conformers, computations were performed on every sixth conformer when energetically ordered starting from the most stable conformer (564 conformers). Those conformers were then geometry optimized on the B3LYP/def2-SVP level of theory, while not all conformers were able to converge to a stable stucture. This convergence issue was not further investigated, after these calculations were disregarded in favor of the ensemble generation presented in the main part of this work, leaving 539 conformers for further analysis. This number was again reduced based on the structure using the clustering tool BitClust[79, 80]. On these remaining 126 conformers, TD-DFT absorption spectra were computed.

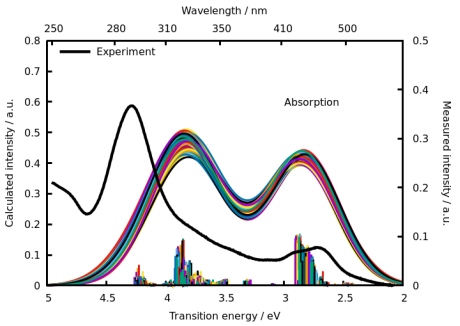

Figure 43: Computed TD-DFT absorption spectra of 126 $Ru(bpy)_2bpyC9$ conformers in acetonitrile (multiple colored lines). Oscillator strengths are drawn as vertical lines. For comparison, the corresponding experimental spectrum is shown in black.

Extensive benchmarking of different level of theory was performed on the CREST run including acetonitrile as implicit solvent, *i.e.*, the one used in the main part of this work. Therefore, the total number of 38399 conformers was reduced to 384 by selecting every tenth conformer when energetically ordered starting from the most stable conformer. Single point calculations in ORCA were performed using the following functionals: B97-3c[81] with and without the resolution of identiy (RI), BP86 with RI, and B3LYP with RIJCOSX.

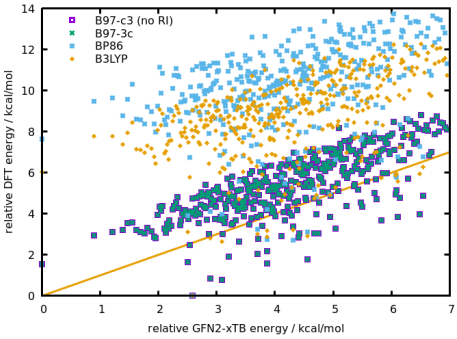

Figure 44: GFN2-xTB vs. DFT energies on 384 GFN2-xTB geometries of C4-PDI-C4. The yellow line denotes identical GFN2-xTB and DFT energies.

Additionally to the results presented for C4-PDI-C4 in the main body of this work, computations were performed on a similar molecule, where the -N^+Me_3 groups were substituted with -N^+H_3 (from now on referred to as HC4-PDI-C4H). A gas-phase CREST run yielded 54 conformers. After optimization on the B3LYP/def2-SVP level of theory and a reduction of the ensemble to 36 conformers using BitClust, standard TD-DFT and vibrationally-resolved absorption and emission spectra were computed.

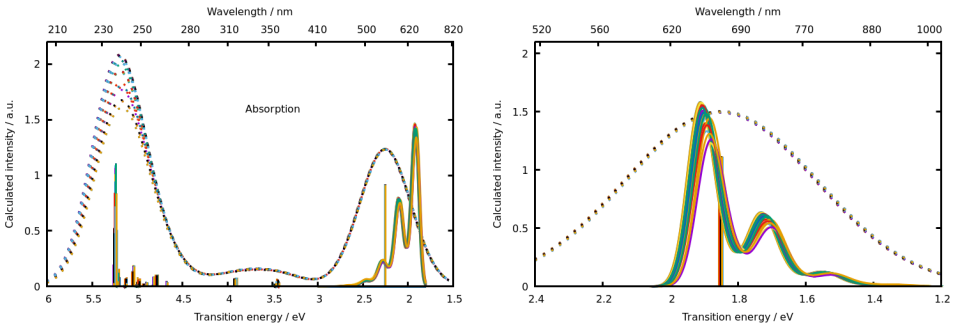

Figure 45: Computed TD-DFT (dotted line) and vibrationally resolved (full line) absorption (left) and emission (right) spectra of HC4-PDI-C4H. Oscillator strengths are drawn as vertical lines.

To select a suitable level of theory, different functionals were employed to computed standard TD-DFT as well as vibrationally resolved absorption and emission spectra of C1-PDI-C1. These functionals include PBE0[82–84], BP86, B3LYP, and CAM-B3LYP[85].

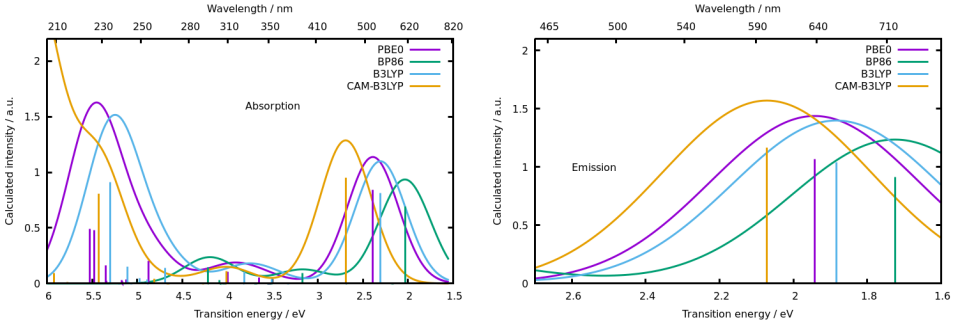

Figure 46: Computed TD-DFT absorption (left) and emission (right) spectra of C1-PDI-C1 for different functionals. Oscillator strengths are drawn as vertical lines.

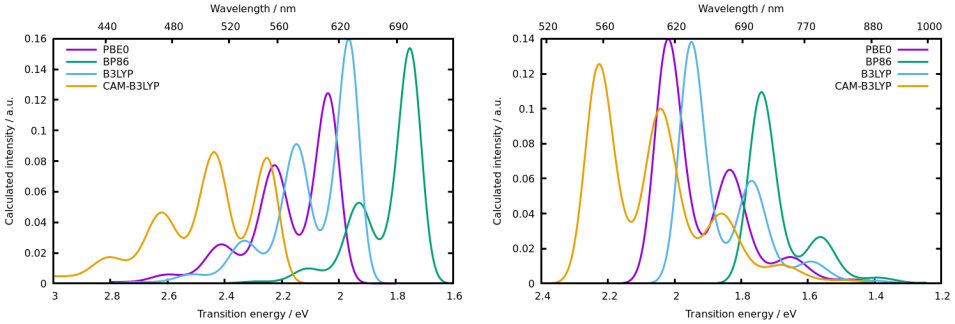

Figure 47: Computed TD-DFT/FCHT absorption (left) and emission (right) spectra of C1-PDI-C1 for different functionals. The relative intensity was adjusted in this representation.